Author:
Sun, Xiaoyang

Title:
Failure of Notched Stiffened Structures Under Tension

Failure of Notched Stiffened Structures Under Tension

By

XIAOYANG SUN

Department of Aerospace Engineering
UNIVERSITY OF BRISTOL

A dissertation submitted to the University of Bristol in accordance with the requirements of the degree of DOCTOR OF PHILOSOPHY in the Faculty of Engineering.

MARCH 2023

Word count: fifty thousand

Abstract

Fibre reinforced composites have seen a huge increase in usage during the past decades owing to their superior strength-to-weight ratio and the ability to tailor material properties based on requirements by adjusting the stacking sequence. These high-performance composites are often found in critical load-carrying components where stringers are necessary. This thesis investigates both experimentally and numerically the interaction between translaminar fracture and stringer debonding with the ultimate goal being to develop a cost-effective modelling method for predicting the fracture behaviour of large stiffened composite panels. The effect of fracture resistance curves (R-curves) on fracture behaviour has been investigated as it is crucial for the accuracy of the modelling method. Stiffened over-height compact tension (OCT) specimens made from Hexcel IM7/8552 pre-preg were designed and manufactured to experimentally determine the fracture behaviour and damage mechanism. Compact tension and extended single-edge notched tension (ESET) specimens made from non-crimp fabric (NCF) were used to experimentally evaluate the damage mechanism and to obtain more information on the R-curve. The effect of ply-thickness on the R-curve has also been considered by testing large compact tension specimens manufactured from unidirectional plies of thickness 0.03 mm. A numerical model based on the Virtual Crack Closure Technique (VCCT) was developed to predict the fracture behaviour of stiffened OCT specimens. The methodology used from the stiffened OCT VCCT model was then used to predict the behaviour of a large notched composite panel with three co-cured hat-shaped stringers.

During the stiffened OCT tests, it was found that stringer thickness has a significant effect on the fracture behaviour - a thinner stringer foot promotes stringer breakage, whereas thicker stringers tend to induce skin-stringer debonding without stringer breakage. R-curves obtained from the compact tension and ESET specimens made of NCF materials showed no obvious plateau within the validity range of the tests. Specimens with thin plies of thickness 0.03 mm yielded a significant smaller fracture process zone and overall a very neat fracture surface with no obvious signs of delamination, and with a flat R-curve. The VCCT model of the stiffened OCT specimen showed a high resemblance with experimental data. A similar philosophy was applied to the large panel with hat-shaped stringers and the results show a high correlation with existing test data.

In essence, this thesis presents the investigation process, both numerical and experimental, that has led to the creation of a novel cost-effective modelling method for accurately predicting the fracture behaviour of notched stiffened structures under tension. With it being cost-effective while still returning good results, this modelling method would be particularly appealing for industrial applications.

Dedication and acknowledgements

I want to start by sincerely thanking my supervisors, Prof. Michael Wisnom and Dr. Xiaodong Xu, for their unwavering support and commitment throughout my PhD and BEng program. Since I was an undergraduate, their depth of subject knowledge, persistence, inspiration, and direction have been tremendously motivating, and they have been wonderful mentors for me to look up to. Additionally, I want to thank them for enabling me to attend key conferences and engage in fascinating conversations with a number of industry leaders.

I owe a great deal of gratitude to Mitsubishi Heavy Industries (MHI) for this project, which they have provided me with a wonderful opportunity to develop and use my skills. Their advice and suggestions have been quite helpful to us as we work on this project. I am also grateful for the financial support provided by the Engineering and Physical Sciences Research Council (EPSRC) as this PhD project would not have been feasible without their help.

For their advice and assistance, I also like to thank the technicians and my colleagues. Particular thanks to Ian Chorley for his assistance and guidance throughout the lab sessions and for his patience with my tight deadlines. Finally, I want to express my gratitude to my family and friends for their unwavering support and joyous distractions at this difficult time. My wife Jiatong, my parents Mr. Sun and Mrs. Zhao, and I appreciate all of their support and encouragement throughout the PhD.

AUTHOR'S DECLARATION

I declare that the work in this dissertation was carried out in accordance with the requirements of the University's Regulations and Code of Practice for Research Degree Programmes and that it has not been submitted for any other academic award. Except where indicated by specific reference in the text, the work is the candidate's own work. Work done in collaboration with, or with the assistance of, others, is indicated as such. Any views expressed in the dissertation are those of the author.

SIGNED: .....XIAOYANG SUN..... DATE: .....20TH MAR 2023.....

LIST OF PUBLICATIONS

[1] Sun, X., Shin-ichi, T., Wisnom, M. R., & Xu, X. (2019, September). Predicting trans-laminar fracture using VCCT and in-situ CT scans. *In 7th ECCOMAS Thematic Conference on Mechanical Response of Composites*.

[2] Sun, X., Takeda, S. I., Wisnom, M. R., & Xu, X. (2020). In situ characterization of trans-laminar fracture toughness using X-ray Computed Tomography. *Composites Communications*, 21, 100408.

[3] Xu, X., Paul, A., Sun, X., & Wisnom, M. R. (2020). An experimental study of scaling effects in notched quasi-isotropic carbon/epoxy laminates under compressive loads. *Composites Part A: Applied Science and Manufacturing*, 137, 106029.

[4] Xu, X., Sun, X., & Wisnom, M. R. (2021). Initial R-curves for trans-laminar fracture of quasi-isotropic carbon/epoxy laminates from specimens with increasing size. *Composites Science and Technology*, 216, 109077.

[5] Xiaoyang, S., Xiaodong, X., Shimizu, T., & Michael, R. W. (2022, June). AN EXPERIMENTAL STUDY OF CRACK PROPAGATION IN STIFFENED OVER-HEIGHT COMPACT TENSION (SOCT) SPECIMENS. *In 20th European Conference on Composite Materials*.

TABLE OF CONTENTS

List of Tables

List of Figures

CHAPTER 1

INTRODUCTION

1.1 Introduction to composites failure

Composites, by definition, involves the integration of two or more constituent materials which often have distinctively different chemical and physical properties. The newly produced composite material will usually inherit the advantageous properties from its constituent materials while the individual elements remain separate and distinct. Owing to the nature of composite materials, failure can take various forms - damage may be specific to one or both of the constituents or involve interaction of the two [1]. In addition, depending on the scale over which the damage is described, the form and severity of the damage varies drastically - from minor voids to large-scale delaminations, holes and laminate failures. Figure 1.1 shows the typical damage at various scales of a composite structure. For the current thesis, the focus would be failures that occur at the ply and laminate level - between 0.1 mm to 5 mm. The load-bearing composite structures used in aerospace applications often are fitted with stringers that run in the direction of the load to provide support against out-of-plane bending/compression or even crack propagation. The focus of this thesis is to investigate the fracture process of notched stiffened structures.

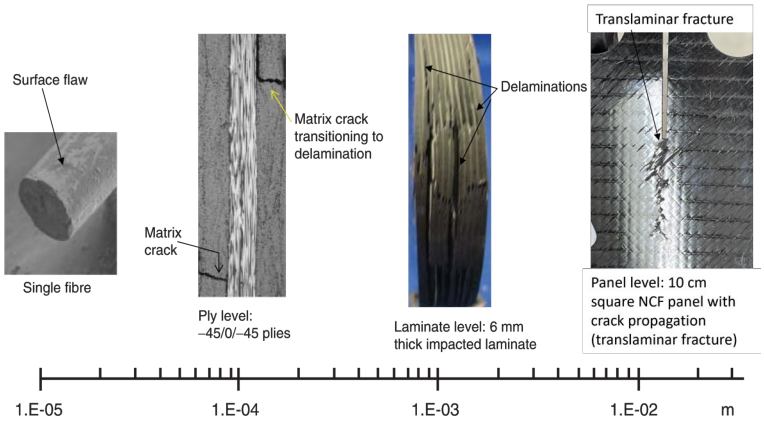

Figure 1.1: Typical damage at various scales of a composite structure, [1].

The failure of notched stiffened structures under tension is a complex and multifaceted problem that has garnered significant attention from researchers and practitioners in the field of structural engineering. These structures, which are commonly found in a variety of civil and military applications, are known for their high strength-to-weight ratio and ability to withstand large loads. However, their structural integrity can be compromised when subjected to tensile forces, particularly when a notch or other imperfection is present. The resulting failure can have catastrophic consequences, leading to significant damage to the structure and potential injury or loss of life.

In recent years, there have been numerous instances of notched stiffened structures failing under tension, highlighting the need for a better understanding of the underlying mechanisms and factors that contribute to their failure.

1.2 Background and objectives

This thesis builds upon the experimental work carried out by S. Takeda [11], where a large-stiffened composites panel was tested. The stiffened panel had a dimension of approximately 900 mm by 750 mm with three hat-shaped stringers co-cured to one side of the specimen. The specimen had a machined notch of length 200 mm running perpendicular to the loading direction. The goal of this thesis is to investigate the failure of notched stiffened structures under tension, with a focus on identifying the key factors that influence their behaviour and developing a cost-effective method to predict the failure of the notched stiffened panel tested by S Takeda et al.

The aim of this PhD thesis is to understand and develop a cost-effective method for predicting the fracture behaviour of large stiffened composite panels. To achieve this, the basics of fracture mechanics in composites were firstly reviewed, followed by a series of experimental investigations with small coupons. The purpose of testing various small coupons is to understand the fracture mechanism of crack-stringer interaction and to gather data for the models. With the knowledge from the small coupons, numerical models were firstly constructed for some small coupons to

validate and refine the model, followed by the construction of the large stiffened panel model. The final model utilises the nodal-energy Virtual Crack Closure Technique (VCCT) and is capable of predicting the failure of large stiffened composite panels to a reasonable degree of accuracy. The cost and time on R&D for MHI, one of the sponsors of this PhD project, would be greatly reduced with the help of a computationally efficient FEA model capable of predicting the fracture behaviour of real structure sized panels with realistic features such as stringers and cracks.

This thesis is a result of the project funded by Mitsubishi Heavy Industries (MHI) and the Engineering and Physical Sciences Research Council (EPSRC) with the aim of developing cost-effective prediction models for large stiffened composite panels. The project started in Nov 2018 running until Nov 2022, when all of the research in the thesis was completed. Some results were presented at the 7th ECCOMAS Thematic Conference on Mechanical Response of Composites in 2019 and The 20th European Conference on Composite Materials (ECCM20) in 2022, as highlighted in the list of publications section.

1.3 Thesis outline

This thesis contains eight chapters in total, with the first and the last chapter being the introduction and the conclusion respectively. Previous literature was extensively analysed in the literature review in **Chapter 2**. The literature review firstly looks into the different composite failure modes, followed by a review of the different specimens used to assess the translaminar fracture of multi-directional composites. The tensile and compressive failure modes of translaminar ply failure are investigated. The modelling section of the literature review looks into the different methods that are available for modelling composite fracture.

Chapter 3 details the characterisation of the fracture behaviour in stiffened Over-height Compact Tension (OCT) specimens. The effect of the stringer thickness is also investigated by testing two batches of OCT specimens with thick and thin stringers.

Chapter 4 details the experimental characterisation of the R-curve of the Non-Crimp Fabric (NCF) using two types of specimen geometries. Eccentrically loaded single-edge-notch tension (ESET) specimens and Compact Tension specimens were both used for the resistance curve (R-curve) characterisation. It was found that the R-curves provided by these sets of data were of limited length and longer R-curves are necessary for the model construction. To achieve a longer R-curve, **Chapter 5** records the design, test and analysis process of a larger compact tension specimen made from thin-ply materials - approximately 0.03 mm ply thickness. Towards the end of **Chapter 5**, all experimental data were gathered and an in-depth analysis was carried out to draw a conclusion for the upcoming modelling chapters.

Both **Chapter 6** and **Chapter 7** detail the modelling work carried out in this thesis. To begin with, **Chapter 6** provides a background to the VCCT modelling technique followed by an initial VCCT model construction of small test coupons. The results of the initial VCCT model

were subsequently analysed with improvements made including the introduction of nodal-energy VCCT and cohesive elements for delamination/debonding simulation. The chapter finishes with a comparison between the nodal-energy VCCT results and the corresponding experimental work. A conclusion was drawn towards the end of **Chapter 6** in regards to the findings of the small coupon models.

With the small coupon models established and compared against test data, **Chapter 7** proceeds to achieve the ultimate goal of this thesis - building a cost-effective modelling method for predicting fracture in notched stiffened composite panels. The model construction was split into two parts - a coupon model with the same material as the large panel was firstly tried and tested against tests data, followed by the actual large stiffened panel. A discussion can be also found towards the end of **Chapter 7**.

Chapter 8 reports the conclusions of the thesis followed by possible future work.

The main novel contribution of the current thesis is by applying the R-curve obtained from small coupons to a newly developed nodal-energy VCCT based FEA model, the fracture process of a large stiffened composite panel can be predicted to a high degree of accuracy while being relatively computationally efficient.

CHAPTER 2

LITERATURE REVIEW

With the substantially enhanced understanding of composite failure, along with the desire for more efficient design, accurate predictions for the onset and subsequent propagation of the damage in composite structures are in high demand.

Much research effort has been made for damage propagation modelling, which includes cohesive elements [15], smeared crack models [16], X-FEM [17] and Hi-FEM [14]. These methods all require the fracture toughness values for the failure modes concerned, hence the development of an accurate experimental technique for fracture toughness characterisation is of considerable importance.

Composites failure modes can be generally divided into three categories: interlaminar failure, intralaminar failure and translaminar failure. Interlaminar failure (i.e. delamination) has been under extensive research for many years. The current leading-edge research in interlaminar fracture toughness testing methods has been comprehensively reviewed by many authors in the past years [18–21].

There are, however, relatively fewer published studies dedicated to the translaminar fracture toughness of composites and these works were often isolated. Such a lack of research effort for translaminar fracture is partly resulting the lack of confidence for using composite materials in primary structures, where these properties possess the greatest effect. However, with the ever increasing adoption of composites in load bearing structures, it is envisaged that the fracture toughness associated with the translaminar failure modes will play an increasingly important role over the coming years. This review draws together the conclusions of these studies to help the readers to have a context of the current PhD project.

2.1 Overview of composite failure modes

Due to the inhomogeneous and anisotropic nature of composite materials, the formation and the subsequent propagation of damage within a laminate is layup dependent. As a result, the fracture toughness of composites may not be a material property. Ultimately, failure will be governed by any one, or a combination of the ply-level failure mechanisms detailed below.

2.1.1 Interlaminar failure

Interlaminar failure, or delamination, describes the failure process when two adjacent laminae debond from each other, which is a prevalent failure mode that distinguishes composites from conventional isotropic materials such as metals. Delamination has received much research interest lately such that standardised test methods for measuring interlaminar fracture toughness have been developed [22–24]. The laminated nature of composite materials, stacking layers of reinforcement, can result in a tendency for delamination during service [25] at weak interlaminar regions. Delamination is a crack separating adjacent plies [26]. When the plane of the crack is parallel and at the same level as the plane of the interface between adjacent plies, delamination takes place. Fracture mechanics principles can often be employed to explain the growth of delamination. The debonding process of the two adjacent laminae can take three forms: opening, in-plane shearing, and out-of-plane shearing, which are often referred to as Mode I, Mode II, and Mode III failures respectively [27], figure 2.1 shows a schematic of the three failure modes. The occurrence of interlaminar failure can be attributed to many factors, including non-optimal curing [19] or imperfections within the material, but it is primarily due to weak matrix. It can also be induced by impact damage, or from the three dimensional interlaminar stresses that develop at discontinuities such as free edges and ply drops [28, 29], shown in figure 2.2.

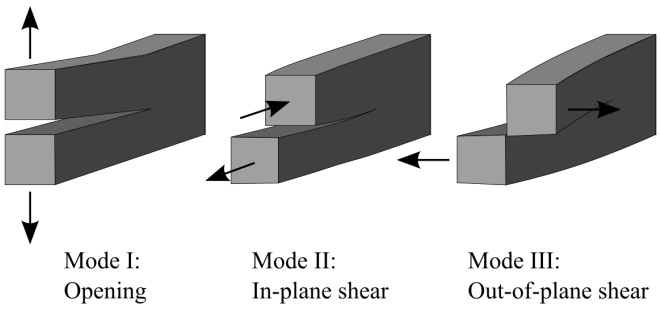

Figure 2.1: Schematics of the three fracture modes.

The general expression for the critical strain energy release rate, G_c, takes the form of [30] -

$$G_c = \frac{P_c^2}{2B}\left(\frac{\delta C}{\delta a}\right) \tag{2.1}$$

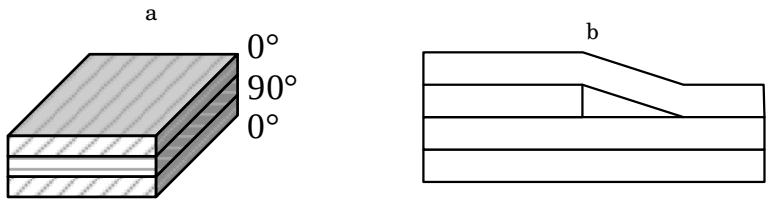

Figure 2.2: Features inducing three dimensional interlaminar stresses. (a) Free edge. (b) Ply drop.

where
P_c = the critical load,
B = the specimen width,
a = the crack length, and
C = the compliance of the ENF specimen. This general expression is valid for any mode mixity and coupon geometry.

For Mode I delamination, the delamination surfaces separate perpendicularly to the plane of delamination [26]. Mode I delamination can be best recreated with a Double Cantilever Beam (DCB) specimen geometry. Consider a DCB specimen of width b, height h, with a longitudinal modulus (along beam length) of E_1, the strain energy release rate G_I can be calculated as [26]

$$G_I = \frac{12P^2a^2}{E_1b^2h^3} \tag{2.2}$$

where
P = Applied load, and,
a = Crack length.

The critical energy release rate G_{Ic} can be calculated at maximum applied load at crack extension a. Stable crack growth is necessary for the experimental determination for the critical strain energy release rate G_{Ic} [31]. The DCB specimen would be under displacement control. An artificial delamination is introduced by inserting a Teflon film at the midplane of the specimen. To permit the rotation of cantilever beams under load, the load is applied through metallic piano hinges that are bonded to the delaminated end of the specimen [26, 32, 33]. Loading rate shall be kept at a low level to enable stable carack propagation. Displacement readings can be obtained from the test machine crosshead or by means of a linear variable differential transformer (LVDT) extensometer.

As for Mode II delamination, the same DCB specimen from Mode I tests can be used but tested in three-point bending and is called end-notched flexure (ENF) specimen, shown in figure 2.3. Shear stresses are present at the tip of the crack due to the load transfer between the upper and lower parts of the beam [25]. The strain energy release rate of Mode II delamination, G_{IIc}, can

be obtained via compliance calibration method [2]:

$$G_{IIc} = \frac{9P_c^2 a_e^2}{16B^2 E_1 h^3} \tag{2.3}$$

where

P_c = the critical applied load,

B = the specimen width,

a_e = the equivalent crack length,

E = the flexural modulus, and

h = the specimen half thickness.

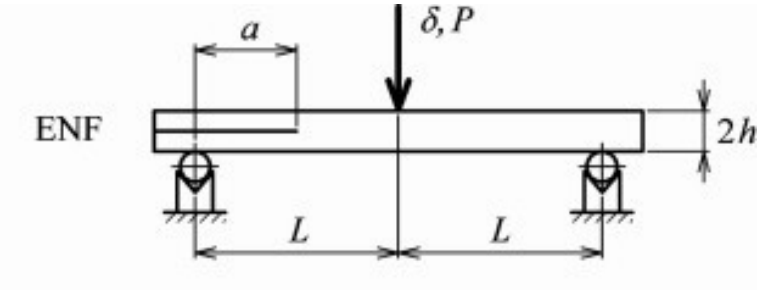

Figure 2.3: Typical End Notch Flexure (ENF) test specimen [2].

Mode III delamination fracture toughness measurement can be carried out with edge crack torsion specimen [3], shown in figure 2.4.

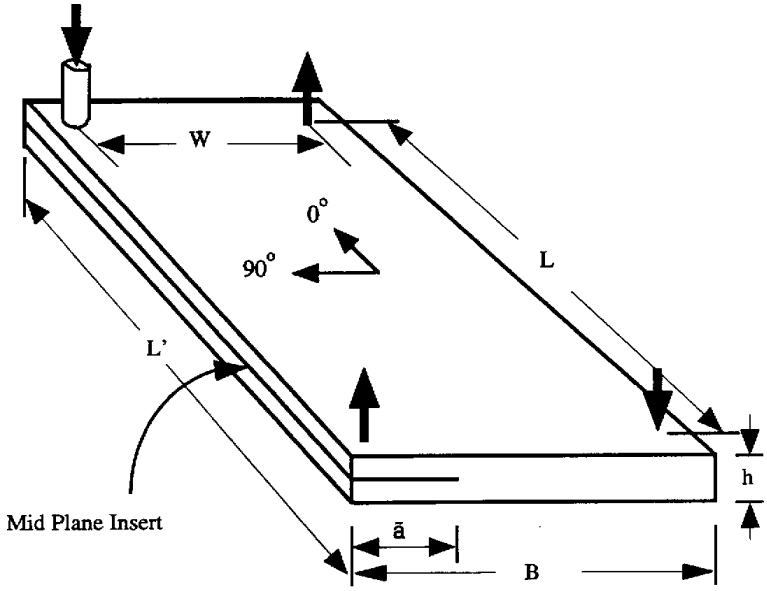

Figure 2.4: Edge crack torsion specimen for Mode III delamination fracture toughness measurement [3].

2.1.2 Intralaminar matrix dominated failure

Intralaminar matrix failure is characterised by matrix cracking either longitudinally or transversely with respect to the fibre direction, shown in figure 2.5. The anisotropic nature of composite materials means that the properties orthogonal to the fibre direction are inherently lower than its longitudinal properties. Owing to this fact, cracks have the tendency to develop parallel to the fibres, which are often the first form of observed damage in fibre-reinforced composites [34]. Many terms can be used to refer to intralaminar matrix failure, namely matrix microcracks, transverse cracks, intralaminar cracks, and ply cracks or splits [35]. Intralaminar cracks can be induced by various loading conditions, including tensile loading, fatigue loading, and even thermal fluctuations. They can often originate from discontinuities and voids during manufacturing [35]. The toughness values obtained from intralaminar matrix failure modes are comparable to those found in interlaminar failure modes [36, 37]. It has been found that interlaminar delamination and intralaminar fracture can often happen simultaneously in one structure, as reported by [38–40]. Previous research suggests that intralaminar cracks can often function as delamination migration pathways between adjacent interfaces [41] or as boundaries that constrain delamination growth [38].

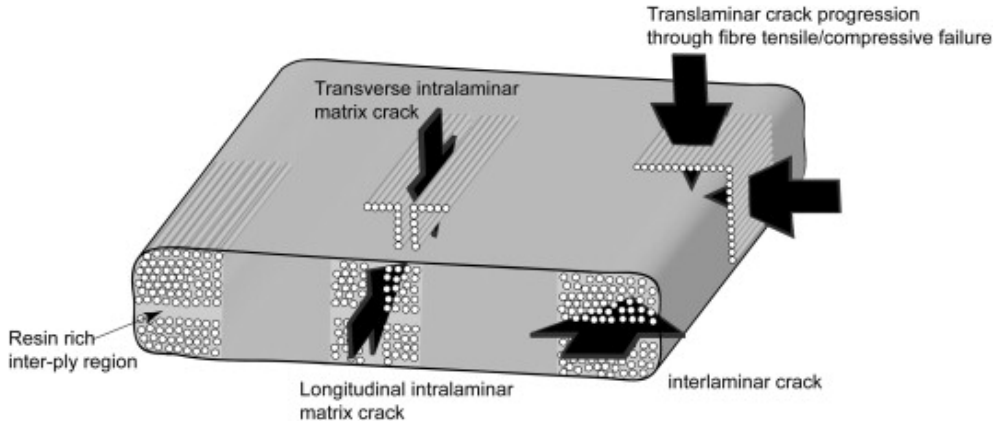

Figure 2.5: Overview of ply level failure modes [42].

Much of the intralaminar fracture research carried out has been focused on the measurement of Mode I (opening) intralaminar fracture toughness of polymer matrix composites [36, 37, 43–54], with a number of test specimen geometries, namely DCB [45, 48, 50, 54–56], the Compact Tension (CT) [36, 43, 46, 47, 49, 52, 57], three and four point bending (3PB and 4PB) [37, 43, 53, 54, 57], and the double torsion test [44].

2.1.3 Translaminar fibre tensile failure

With fibres being the predominant load-carrying constituents of fibre-reinforced composites, the breakage of the fibres in the load-carrying direction often implies the failure of the structure. Consider a unidirectional composite structure loaded in tension, fibre failure takes place

at weak points on the fibres. Stress is then redistributed to the fibres in the vicinity of the broken fibres via matrix shear, possibly breaking some more fibres [35]. Fibre tensile failure is statistically controlled owing to the non-uniformity of fibre strength along the fibre length and stress redistribution [58]. Due to this statistical nature of fibre failure, the failure tensile strength of a ply within a general laminate is difficult to predict from the tensile strength of the fibres [59, 60]. While the properties of the constituents play a significant role in determining the overall material fracture properties, it is also heavily impacted by the efficiency of bonding across the interface [61].

The foundation of brittle fracture originating from a crack was established by Griffith back in 1921 [62, 63], where the unstable crack extension was associated with strain energy release rate. Three decades later Irwin [64] introduced the crack-tip local stress-strain field and the characterisation of fracture in terms of stress intensity factor. At the molecular level, fracture is the debonding of atoms across a fracture plane, giving rise to new surfaces. This process of bond breakage perpendicular to the fracture plane is called cleavage, and therefore the theoretical tensile strength of a material will be associated to it [65, 66]. However, it was later found that the failure strength of most engineering materials was much lower than the theoretical predictions made by the atomic model. Griffith [62] suggested that such a discrepancy between theoretical strength and measured strength is due to stress concentrations. The stress concentrations arise due to inherent defects in the material causing very high local stresses at the tip of these cracks, thereby fracture. Using Inglis's [67] solution, Griffith was able to provide some justification for the reduction in the theoretical strength [68]. To combat this issue, Griffith proposed to use an energy balance approach, where "fracture will occur if sufficient energy was released from the strain field to support the energy requirements of the crack", relating the change in energy during crack growth with the energy required to create new fracture surfaces. The critical amount of energy required is denoted by G_c. Irwin later proposed a second related fracture criterion [64] in terms of stress intensity factor, K, where K describes the manner in which the local stress is proportional to the inverse square distance from the crack-tip. He suggested that fracture occurs when the stress intensity factor, K, attained a critical value K_c.

The use of the stress intensity factor K approach has some apparent limitations when applied to composite materials -

- K characterises the stress distribution immediately ahead of a crack. K may be readily defined for a homogeneous, isotropic materials but composites are usually neither of these. Hence the meaning of K is questionable for composites.

- At fibre-matrix interfaces there will be a conversion of loading mode, i.e. pure mode loading will become mixed-mode, and hence a mixed-mode value of K will be required.

- For the K approach to be valid, the K controlled singular field should be dominant and control the fracture process. In composites, the singular field is often very small and

localised compared to the damage zone ahead of the crack tip.

Due to the above-listed reasons, the energy release rate or G approach is often adopted instead. It utilises a global energy balance and eliminates the need to make any assumptions about the stress around the crack tip or process zone. Data suggests the critical strain energy release rate of PAN-based carbon fibre itself can be as low as 7.4 J/m^2 [69], however, with the numerous strengthening mechanisms available, such as crack blunting and fibre pull-out, the resulting homogenised ply-level fracture toughness could be orders of magnitude higher than that of the fibre alone.

2.1.4 Translaminar fibre compressive failure

Owing to the slender nature of high-modulus fibres, their compressive strength is relatively low despite their excellent strength and stiffness in tension. Such phenomenon can be easily explained by the Euler buckling equation where for a column of length L with a cross-sectional moment of inertia I, when subject to a compressive force P, becomes unstable when

$$P \geq \frac{\pi^2 EI}{L^2} \tag{2.4}$$

From equation 2.4, one can conclude that a long, slender fibre ought to have little load-carrying capacity in compression. However, equation 2.4 is considering the situation where fibres are standing alone, which is not the case in a typical CFRP material where many fibres are parallel to each other in close vicinity and are bonded together by the matrix material. An early effort to take the matrix into account when calculating composite compressive strength was by Rosen et al. [70], where he proposed the compressive failure criterion for UD composites is:

$$\sigma_c = \mu_{LT} + \pi^2 E_f V_f \left(\frac{r}{L}\right)^2 \tag{2.5}$$

where μ_{LT} is the longitudinal transverse shear modulus of the composite and E_f is Young's modulus of the fibres. It was found Rosen's model over-predicts the actual compressive strength of composites by a factor of approximately four [71]. There are three reasons for such discrepancy - one being the misalignment of the fibres; one being this model assumes the material behaviour remains elastic, whereas matrix yielding may be likely; the last being it considers global fibre instability, whereas fibre buckling is a local event [72, 73]. Figure 2.6 shows kink band computer tomography pictures from two materials - AS4/PEEK composite [74] and Cu/Nb nanolaminate composite [75]. Under compressive load, failure of the fibres aligned with the loading axis can initiate as either shear-driven fibre failure, or fibre kinking. Any imperfections within the material such as fibre misalignment would induce an shear force which causes fibre rotation, thereby potentially causing fibre kinking. All fibre kinking can be regarded as an instability-driven phenomenon.

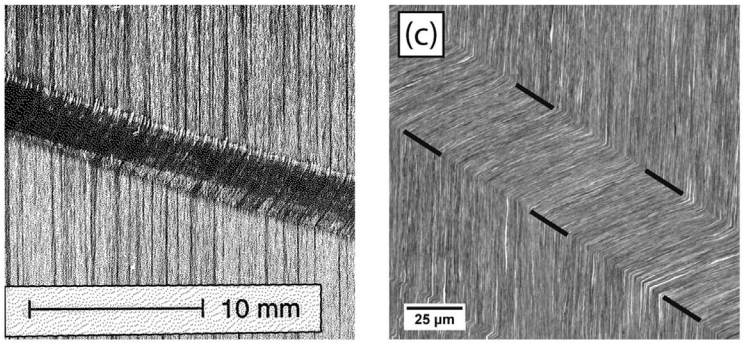

Figure 2.6: Kink-band computer tomography in two materials, (a) AS4/PEEK composite, (b) Cu/Nb nanolaminate composite.

2.2 Translaminar fracture of multidirectional laminates

Unlike the instantaneous nature of fibre failure in a tensile test, failure in translaminar fracture propagation tests, while also involving the breakage of axial fibres, can occur in a relatively stable and homogeneous manner.

The R-curve, short for resistance-curve, measures the material resistance to crack propagation as a function of crack length [27]. Crack propagation occurs when the strain energy release rate is equal to the fracture energy, but this propagation can be stable or unstable depending on how the above two factors vary with crack size. To determine if a crack propagation will be stable or not, the fracture energy term can be replaced with R - the material resistance to crack extension [71]. The R-curve is obtained by plotting the material resistance, R, as a function of crack extension. Figure 2.7 shows a typical R-curve.

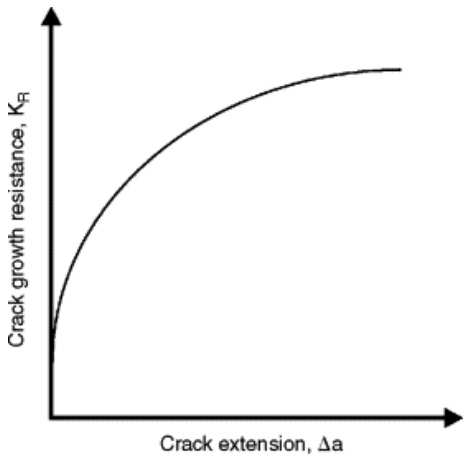

Figure 2.7: A typical R-curve, [4].

Crack growth stability is dependent on numerous factors including material systems, lay-up and specimen geometry. A stable crack growth requires the rate of change of the energy release

rate with crack length to be smaller than zero (assuming no R-curve) [27], that is:

$$\frac{dG}{da} \leq 0 \tag{2.6}$$

where, G is the energy release rate, and a is crack length. A value of $\frac{dG}{da}$ greater than zero will render the crack growth to be unstable. On the other hand, assuming that there is a R-curve, then for a crack propagation to be stable, the following requirement needs to be fulfilled [27]:

$$\frac{dG}{da} \leq \frac{dR}{da} \tag{2.7}$$

where, R is the fracture resistance, G and a denotes the same parameters as in equation 2.6.

Previous work related to translaminar fracture has mainly been focused on measuring the toughness of multidirectional laminates manufactured from unidirectional or 2D woven material systems [13, 76–81]. Translaminar fracture toughness is a lay-up-dependent property which is not intrinsic to the material system and will be the result of the constituent plies failing in a combination of any of the aforementioned failure modes in section 2.1. Of the various specimen configurations, shown in figure 2.8, only the compact tension, three/four point bend and extended compact tension specimens exhibit stable crack growth. A stable crack growth is a must for capturing the change in critical strain energy release rate with the evolution of damage in the form of a resistance curve (R-curve).

2.2.1 Compact tension

The Compact Tension specimen, shown in figure 2.8a, is a widely adopted configuration for the testing of fracture toughness. Its wide adoption covers many material systems including: metals, carbon/epoxy [82–88], Vectran/epoxy [89], carbon/carbon [90, 91], carbon/PEEK [92] and boron/aluminium [93, 94].

The data reduction scheme recommended by the ASTM E399 [12] standard is the most widely used method for CT configurations [49, 93–97], which indicates the critical stress intensity factor K_{Ic} can be calculated as:

$$K_{Ic} = \frac{P}{t\sqrt{w}} f(a/w) \tag{2.8}$$

where, P is the critical-load causing crack propagation, t and w are specimen dimensions as per figure 2.8, a is the crack length and $f(a/w)$ is a finite width correction factor. It should be noted that many previous studies [49, 93–97] have been using values of $f(a/w)$ obtained from conventional metallic structures for composite calculations, and the interchangeability of these values is still open to question as the equation is largely empirically derived [79, 98].

The critical strain energy release rate, G_{Ic}, can be determined via three options: critical stress intensity factor [99], area method [92], and change of compliance [94, 100]. Using the critical stress intensity factor, the critical strain energy release rate can be established as [101]:

$$G_{Ic} = \sqrt{\left(\frac{1}{2E_{xx}E_{yy}}\right)} \sqrt{\sqrt{\frac{E_{xx}}{E_{yy}}} - \upsilon_{xy} + \frac{E_{xx}}{2G_{xy}}} K_{Ic}^2 \tag{2.9}$$

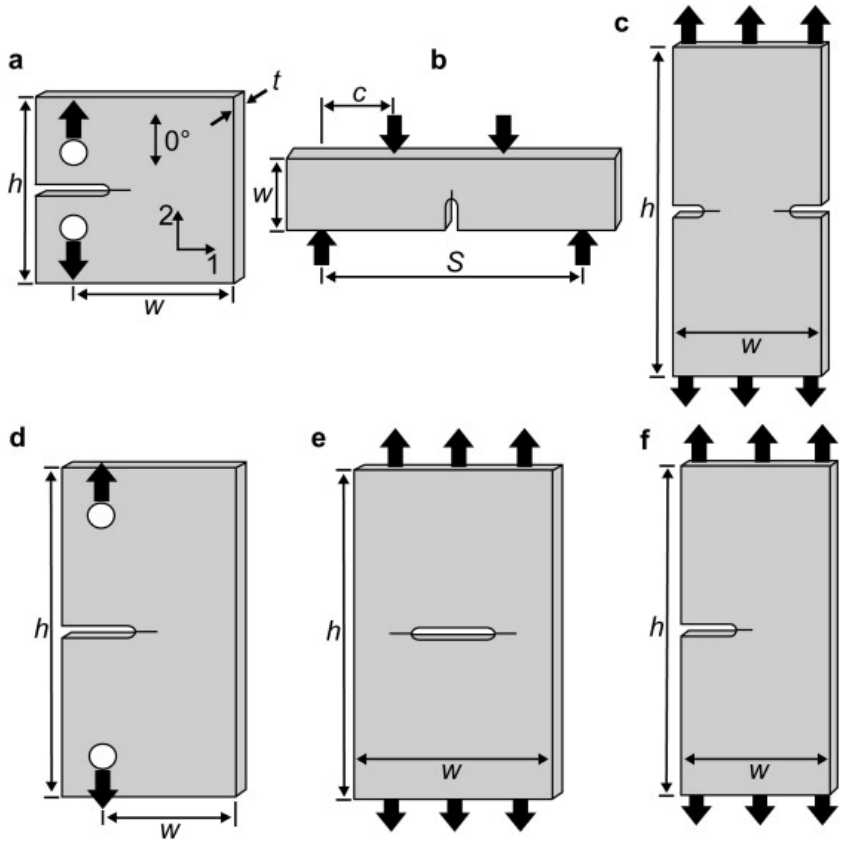

Figure 2.8: Translaminar fracture toughness measurement specimen configurations: (a) compact tension/compression, (b) four-point bend, (c) double edge notch tension, (d) extended compact tension, (e) centre notched tension, (f) single edge notched tension [42].

where E and G are the laminate in-plane extensional and shear moduli, respectively, and v is Poisson's ratio. For a laminate with a quasi-isotropic layup, assuming plane stress, equation 2.9 simplifies to the following:

$$G_{Ic} = \frac{K_{Ic}^2}{E} \tag{2.10}$$

Alternatively, the critical strain energy release rate can be determined directly from the rate of change of compliance with crack length, C:

$$G_{Ic} = \frac{P_c^2}{2t}\frac{dC}{da} \tag{2.11}$$

where P_c is the critical load causing crack extension, t is the specimen thickness, C is the compliance and a is the crack length. There is also the area method [92] which may be used for the determination of critical strain energy release rate, where the area underneath the load-displacement curve is divided by the fractured area associated with crack growth:

$$G_{Ic} = \frac{1}{2t(a_2 - a_1)}(P_1\Delta_2 - P_2\Delta_1) \tag{2.12}$$

where at a_1, the critical load is P_1 and the displacement is Δ_1; at a_2, the load is P_2 and the displacement is Δ_2.

In addition to the above-mentioned methods for determining the fracture energy, there also exists the J integral method. The aforementioned methods such as the stress intensity factor assume the stress field ahead of the crack tip is linear elastic with no crack tip plasticity for metals, or damage for composites. If there is a significant crack tip damage zone then G shall not be determined from the elastic stress field. The J integral method offers the means to determine the strain energy release rate where crack tip plasticity is non-negligible.

Path-independent contour integrals were established by Rice [102] based on energy conservation, shown in equation 2.13.

$$J = \int_{\Gamma} \left(W dy - T \frac{\partial u}{\partial x} ds \right) \tag{2.13}$$

where $W = W(x,y) = W(\epsilon) = \int_0^{\epsilon} \sigma_{ij} d\epsilon_{ij}$

Figure 2.9 shows the schematic of the closed contour Γ which should be followed counter-clockwise in a stressed solid. Orthogonal to Γ is the tension vector T, u is the displacement in the x-direction and ds is an element of Γ. W is the strain energy per unit volume. In a closed loop $J = 0$.

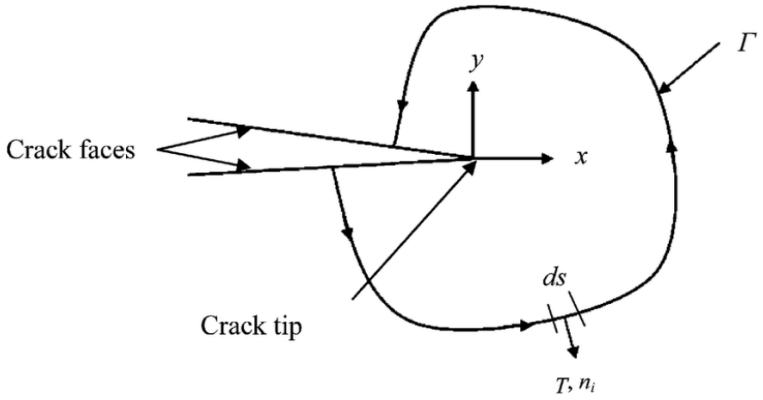

Figure 2.9: Definition of J integral. [5]

Since the path-independent contour proposed by Eshelby is based on energy conservation, it is safe to postulate that the J integral is an energy-related property. Both W and $T\frac{\partial u}{\partial x}$ in equation 2.13 have strain energy incorporated in these terms [27]. It has been reported by Rice [102] that the J integral around the crack tip is the change in potential energy for a virtual crack extension da:

$$J = -\frac{\partial V}{\partial a} \tag{2.14}$$

where V is the potential energy. And for a linear elastic material $-\frac{\partial V}{\partial a} = G$, hence it could be shown that $J = G$ for a linear elastic case [27]. For cases where significant plastic deformation is present, J could be argued to be a more universal fracture criterion than G. But for cases where

plastic deformation is negligible, then $J = G$ and thereby $J = G = \frac{K^2}{E}$. For such elastic materials, one could deduce that fracture would occur if J exceeds J_{Ic} which is equal to G_{Ic}. And for plastic materials, the ease of measuring J_{Ic} could ultimately determine if it would be a widely adopted fracture criterion [27].

2.2.2 Extended compact tension

With a resembling shape to the compact tension specimen, the extended compact tension (shown in figure 2.8d) specimen was used by a few researchers [103, 104] to alleviate some undesirable failure modes which occurred in the conventional compact tension tests. ASTM E1922 [105] standardises the use of extended compact tension specimens to determine the translaminar fracture toughness of laminated and pultruded polymer matrix composite materials. However, the standard only covers the measurement of translaminar fracture toughness at initiation, hence an R-curve effect cannot be fully captured.

Similar to compact tension specimens, the stress intensity factor, K_{Ic}, can be calculated with equation (2.8), but the way $f(a/w)$ is calculated is strictly only valid for isotropic materials. For K_{Ic} measured from the maximum load during testing to be valid, the following criteria ought to be fulfilled [105]:

$$\Delta V_n / V_{n-0} \leq 0.3 \tag{2.15}$$

where, $V_{n-0} = V_n$ at $P = P_{max}$ on the extension of the initial linear portion of the plot, see figure 2.10, and ΔV_n is the additional notch-mouth displacement up to the P_{max} point. The ASTM standard [105] states that if the validation in equation 2.15 is not met, then this indicates the damage process zone ahead of the crack tip is proportionally too large for the specimen for an accurate K_{Ic}.

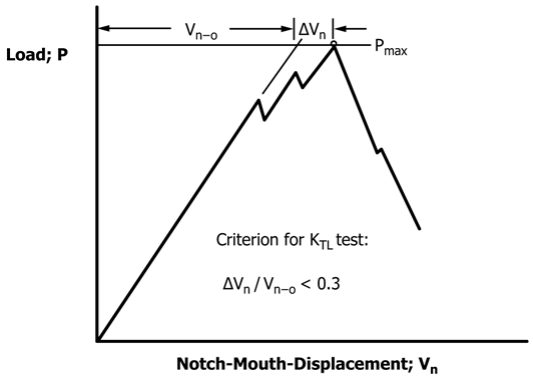

Figure 2.10: Typical load-displacement plot for ECT [105].

2.2.3 Centre notched tension

The centre notched tension specimen, shown in figure 2.8e, has been used for the testing of carbon/epoxy [95, 96, 106–109], carbon/bismaleimide [107] and boron aluminium system [93]. With the loading directions reversed, it can also be used to determine the compressive fracture toughness. It is also common to replace the centre notch with an open-hole, rendering a different fracture toughness result.

For centre-notched specimens, the critical stress intensity factor K_{Ic} can be determined from:

$$K_{Ic} = \sigma_c \sqrt{\pi a} f(a/w) \tag{2.16}$$

where σ_c is the applied stress at fracture initiation, and that $f(a/w)$ is a finite width correction factor.

2.3 Characterisation of translaminar ply failure modes

So far the work addressed in the previous sections has been focusing on the measurement of fracture toughness of laminates. The resulting critical strain energy release rates G_c, represnets the damage processes displayed in each individual ply. These properties are lay-up dependent and are not intrinsic to the material system [42].

On the other hand, research carried out by Vaidya et al. [110] suggests that G^0_{Ic} and K^0_{Ic} are intrinsic material properties, where G^0_{Ic} is the mode I critical strain energy release rate of 0° plies and K^0_{Ic} is the critical stress intensity factor of 0° plies. Such a conclusion was drawn as they related the stress carried by the 0° plies in a laminate to the stress carried by the laminate, via a parameter η:

$$\sigma^0_c = \eta \sigma_c \tag{2.17}$$

with η being dependent only on the lay-up and elastic properties of the constituent plies in the laminate in question. It was also found that an identical relationship exists between the ply critical stress intensity factor and its 0° ply counterpart:

$$K^0_{Ic} = \eta K_{Ic} \tag{2.18}$$

Using this relationship, they were able to predict the fracture toughness of multidirectional laminates to a high degree of accuracy.

2.3.1 Tensile failure

The impact of the notch root radius, ρ, on the critical strain energy release rate (G^0_{Ic}) has been explored for cross-ply IM7/8552 CT samples. The translaminar toughness, assessed at the onset, appeared to be unrelated to the notch root radius for values less than 250 microns. Beyond this threshold, a noticeable initiation toughness was observed. A fractographic examination of

the samples led to the conclusion that there was no substantial interplay between the 0° and 90° ply failure patterns, and that the critical notch root radius for the tested laminate was a characteristic of the 0° plies [79].

Previous work carried out by Li et al. [111] investigated the effect of specimen thickness and lay-up on translaminar fracture toughness. The Over-height Compact Tension (OCT) specimens were manufactured from IM7/8552 pre-preg, consisting of cross-ply and quasi-isotropic laminates of varying thicknesses. Results show that stacking sequence and ply-block thickness have significant influence on the failure mechanism and damage zone. Dispersed plies are damage inhibitive, the damage blunting effects are therefore less effective, rendering higher local stress at the notch tip. In contrast, larger damage zones were observed on laminates with higher ply-block thickness, induced by more subcritical damage such as splitting and delamination. As a result, the load-displacement curves of these laminates are non-linear, different to those found in specimens with dispersed plies. Such sub-critical damage prior to ultimate failure reduces the stress concentration at the crack tip, hence a tougher laminate compared to its counterpart with dispersed plies.

Xu et al. [112] investigated the effect of thickness and crack length on Mode I trans-laminar fracture toughness of QI specimens. Centre-notched quasi-isotropic IM7/8552 laminates with a stacking sequence of $[45/90/\text{-}45/0]_{ns}$ with a notch length of 12.7 mm and 25.4 mm were used. Test results suggest a decrease in tensile failure stress for the 25.4 mm crack length specimens as the specimen thickness increases from 1 mm to 8 mm, while no apparent trend is visible for the 12.7 mm crack length specimens. Translaminar fracture toughness and tensile strength are direclty proportional since tensile strength is the only non-geometrical parameter when calculating trans-laminar fracture toughness. It was concluded that the double 0° central ply promotes sub-critical damage such as splitting and delamination, hence the observed higher toughness values compared to outboard single 0° plies. As the specimen thickness increases, the central double 0° plies account for a smaller proportion of the 0° plies, hence the reduced effect. The longer 25.4 mm notch results in a lower normalised split length, which leads to a stable crack propagation as the equivalent stress concentration factor reduces when the crack propagates. Whereas for the shorter 12.7 mm notch, the equivalent stress concentration factor is approximately the same before and after the crack propagates, leading to an unstable crack propagation. Such a phenomenon justifies the lower fracture toughness found in specimens with a shorter 12.7 mm notch. Which explains why if the specimen is too small, premature failure occurs before the damage process zone is fully developed and the apparent translaminar fracture toughness is lower. The effect of thickness and notch length on cross ply laminates could be the target for future research.

Most of the literature focused on the translaminar fracture toughness of composites has adopted a ply-by-ply failure analysis method, however, Torabi and Pirhadi [113] very recently introduced a novel concept: The Virtual Isotropic Material Concept (VIMC). In it Torabi claims

that orthotropic laminated composites can be approximated by linear elastic brittle material, with the aid of the maximum tangential stress criterion and the mean stress criterion. Specimens of various lay-ups including unidirectional, cross-ply and quasi isotropic were manufactured from Epon 828 E-glass cloth fibre. Different notch tip radii were considered, including 1 mm, 2 mm and 4 mm. Considering all the notch tip radii, the lay-up configurations, and the numbers of ply, the average discrepancies of VIMC-MTS and VIMC-MS criteria are obtained equal to approximately 8.7% and 9.8%, respectively, indicating that both criteria are generally successful in predicting the load carrying capacities of the centre notched glass/epoxy composite laminates tested. Results indicate an increase in the last-ply failure load as the notch radii increases from 1 mm to 4 mm, which is in disagreement with the previous literature. Xu et al. suggested a higher fracture toughness could be the result of sharper notches as the sharper notch induces a higher local stress concentration, which in turn causes more local notch blunting effect, rendering a higher fracture toughness. It could be argued that the discrepancy in the notch radii effect is due to the difference in absolute value of the notch sizes. In hindsight, the novel VIMC has the potential to predict the last ply failure load of centre notched laminates under pure mode I loading using only translaminar fracture toughness and the ultimate tensile strength.

2.3.2 Compressive failure

In virtually all load-carrying structures, there are tensile and compressively loaded parts. Therefore it is no surprise that the compressive performance of composites is equally important as tensile performance. However, unlike tension which is mostly a stable loading pattern (depending on the G and R values), compression may often carry some stability issues to the structure that negatively affects performance.

There is a limited amount of research on notched composite compressive failure. Pinho et al. [98] investigated the fracture behaviour of cross-ply T300/913 laminates using compact compression samples (figure 2.11), a modified version of compact tension samples with a tapered notch to allow for the displacement during compression. It was suggested that when compressive load is applied to the sample, a horizontal kink band that is orthogonal to the loading direction develops from the notch tip, for approximately 20 mm. The kink band can be viewed as crack development, however, it was proven to be difficult to observe optically. With the aid of C-scans, it is clear that the kink band was accompanied by a large area of delamination underneath the surface plies, further complicating the damage mechanism.

Further to Pinho, work carried out by Rawlings et al. [6] focused on the matrix cracking performance. In it some pre-preg material (CFRP) was used to manufacture four types of compression samples, however, the exact type of the material was undisclosed. The types of compression samples include: Compact Compression (CC), Centre Notched Compression (CNC), Edge Notched Compression (ENC), and Tapered Edge Notch Compression (TENC), shown in figure 2.12. Out of these, it was reported only the TENC specimens were able to produce a stable crack propagation,

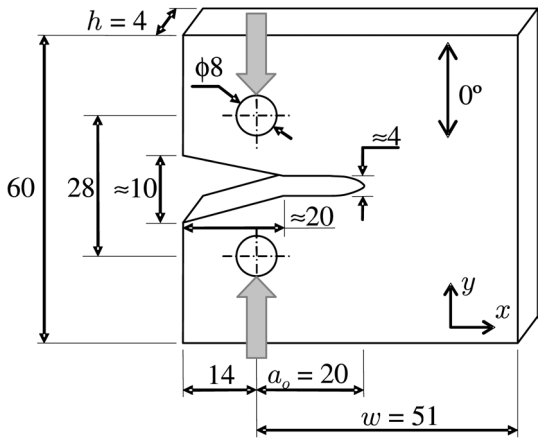

Figure 2.11: Schematic of the compact compression sample used by Pinho et al. [98].

indicating that a linear variation in specimen thickness can suppress the crack propagation through the material.

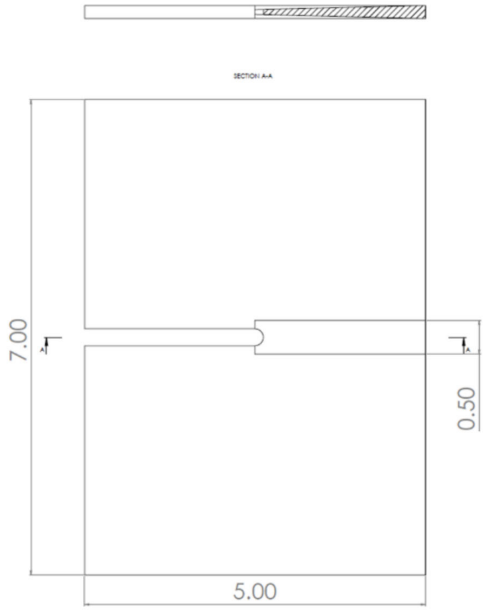

Figure 2.12: Schematic of a Tapered Edge Notch Compression (TENC) specimen, figure from ref. [6]. Dimensions in inches.

Research carried out by Kuhn et al [114]. focused on the fracture resistance curves for fibre compressive failure mode in polymer composites under dynamic loads. It utilised the concept of energy release rate, size effect law and R-curve. Double edge notched specimens of four different sizes were manufactured from IM7/8552 material with a stacking sequence of $[0/90]_{8s}$. Test results suggest a 63% higher fracture energy R for the dynamic loading as compared to quasi-static, with the R-curve shown in figure 2.13. It was also reported by the author that the fracture process zone increased from 2.05 mm to 2.24 mm when dynamic load is applied. Pinho et al. [98]

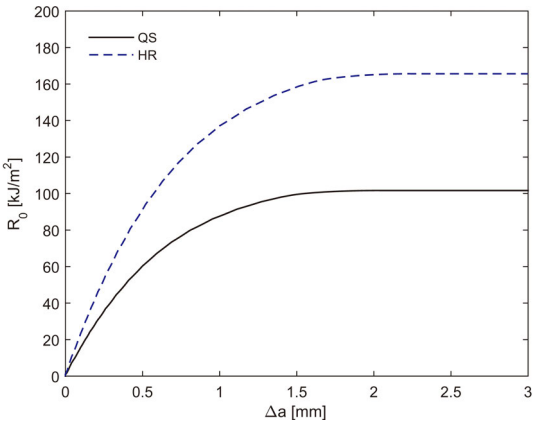

Figure 2.13: Compressive R-curve of IM7/8552 double edge notched specimens for quasi-static and high rating loading, [114].

suggested that despite the fact that meaningful initiation values could be obtained from compact compression tests, due to the presence of contact forces across the kink-band during propagation, the R-curve could not be derived from the data observed during testing.

2.4 Modelling methods for composites fracture

There exists a substantial size gap between testing coupons, which are typically in centimetres, and real engineering structures made of CFRP, typically in meters. In addition, full-scale structures with notches are often found to be tougher than expected [13] due to the existence of resistance curves, hence a numerical method is required to accurately predict the size effect of composites (i.e. size induced failure stress variation). The R-curve effect can be accounted for via many methods such as the cohesive zone model [115, 116], Virtual Crack Closure Technique, High-fidelity Finite Element Method [14], and continuum damage mechanics [117–119].

2.4.1 Cohesive zone models

Linear elastic fracture mechanics (LEFM) is a valuable tool for solving fracture problems as long as the crack-like notch or flaw in the body has a negligible nonlinear zone ahead of the crack tip. However, this condition does not hold for materials like ductile metals or cementitious materials, where the size of the nonlinear zone due to plasticity or microcracking is comparable to the dimensions of the cracked geometry. Even for brittle materials, LEFM requires the presence of an initial crack, meaning that blunt notches without cracks cannot be analyzed using LEFM. Concrete exhibits both of these shortcomings, as stress concentrators acting as notches are often found in structural elements, and the nonlinear zone coincides with the fracture process zone and can be measured in tenths of a meter for ordinary concrete [120]. To resolve this issue, Hillerborg [121] proposed the *fictitious crack model*, initially for concrete, also known as the

Cohesive Zone Model (CZM). Despite being developed for concrete, the cohesive zone model is a general model which can be deployed to other material systems. Tijssens et al. [122] used a cohesive surface method to simulate crazing in polymers. Lin et al. [123] demonstrated strength mismatch effects in welded joints using a cohesive zone model.

Li et al. [124] presented a two-parameter model capable of predicting the fracture behaviour of notched or cracked composites specimens. The two-parameter model involves taking a characteristic toughness and a characteristic strength of the material. The compact tension and single edge notch tension specimen geometries were used for the study. Results showed that with this two-parameter cohesive zone model, the strength, deformation and energy dissipation of the specimen could be well predicted. However, the author also reported that when the initial crack length or ligament length were small, a three-parameter cohesive zone model may be required where an extra parameter - matrix-cracking strength would be needed. In addition, the model was also capable of capturing the onset of catastrophic failure in static tests - where no further input of energy into the system was required for crack propagation.

2.4.2 VCCT

The Virtual Crack Closure Technique (VCCT) was firstly proposed by Irwin[64] in 1957, it was stated that when a crack is extended, the energy required to open the crack is the same required to close it. VCCT has gained much popularity lately for its capability to computationally predicate structural responses, especially involving delamination. VCCT analysis involves the computation of displacements and nodal forces in local elements around the crack tip.

Consider a crack opening situation in a four-noded element as shown in figure 2.14. The mode I and mode II components of the strain energy release rate, G_I and G_{II} can be calculated as [7] -

$$G_I = -\frac{1}{2\Delta a} \cdot Z_i \cdot (W_l - W_{l^*}) \tag{2.19}$$

$$G_{II} = -\frac{1}{2\Delta a} \cdot X_i \cdot (u_l - u_{l^*}) \tag{2.20}$$

where Δa is the length of the element at the crack front and X_i and Z_i are the forces at the crack tip (nodal point i). The nodal displacements at the upper and lower crack faces (u_l and W_l) and (u_{l^*} and W_{l^*}) are used to calculate the relative displacements behind the crack tip. It is assumed the two-dimensional model is of unit thickness '1' and therefore the crack surface ΔA created is calculated as $\Delta A = \Delta a \cdot 1$. Raju [125]. also showed that the equations are applicable if triangular elements, obtained by collapsing the rectangular elements, are used at the crack tip [7].

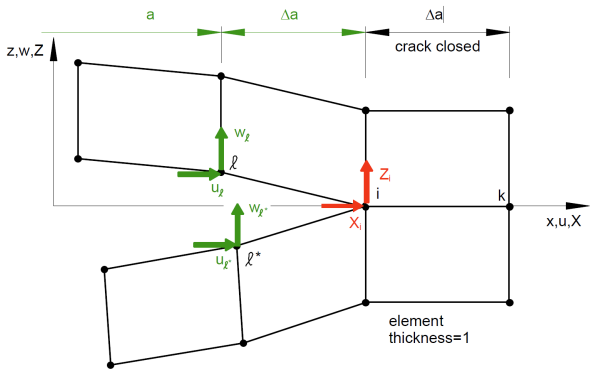

Figure 2.14: Virtual Crack Closure Technique for four-noded element [7].

A recent publication by Xu et al. [11] investigated the initial fracture propagation in a full-scale stiffened panel and stiffened coupons using experimental methods and VCCT. Specimens were manufactured from non-crimp fabric through vacuum assisted resin transfer moulding. It was concluded that the critical strain energy release rate determined from VCCT analysis of failure of small coupons can be used to derive the failure load for the full-scale stiffened panel using VCCT analysis provided the damage process zone is included in the crack length.

Mode I translaminar fracture toughness of pultruded glass fibre reinforced plastics (GFRP) has been investigated by Xiong et al. [126] using VCCT. Tests were carried out using the ESET specimen detailed in the ASTM E1922 standard [105] and results were calibrated using VCCT based finite element methods. A correction function based on VCCT was proposed and a good correlation between the corrected results and test data have been found.

A recent publication by Heidari-Rarani et al. [127] investigated the suitability of three methods for modelling delamination propagation in composite Double Cantilever Beam (DCB) specimens. The three methods considered are VCCT, CZM, and the extended finite element method (XFEM). Two-dimensional plain strain and three-dimensional DCB models were both considered. Results show that the VCCT method lacks the ability to produce accurate results for crack propagation in composite laminates, potentially due to its single critical strain energy release rate input, but benefits from being a simple and effective way to predict delamination initiation.

Additionally, a VCCT based finite element analysis model was developed by Orifici et al. [128] to predict the propagation of delamination in composites. This method involved simulating the structure using two layers of shell elements that are separated by a nominal distance and connected through multiple-point constraints (MPCs). After each increment, the VCCT is employed to compute the strain energy release rates at the MPCs located on the crack front. When basic single-mode criteria are met, any MPCs that fail are released, causing a propagation of the disbonded area in the subsequent increment. The degradation model with four propagation methods was employed to generate numerical predictions, which were compared to experimental results for double-cantilever beam specimens. The results showed a close correlation between the

numerical and experimental data for all aspects of structural behaviour, including load-carrying capacity, structural deformation, and crack propagation. Among the propagation methods tested, the approach that adjusted the values of strain energy release rate based on the crack front in the next increment yielded the closest agreement with the experimental data. This approach proved more accurate than a simple fail-release method, as it resulted in a better match between the predicted and actual energy released during crack growth. Notably, the use of VCCT with relatively large elements was found to produce results that were almost identical to those obtained with a finely meshed model with element sizes similar to the ply-thickness. Furthermore, using smaller elements was found to have a double disadvantage, as it increased both the computation time and the need for smaller increments.

2.4.3 Hi-FEM

Work carried out by Xu [14] et al. numerically investigated the R-curve effect of quasi-isotropic IM7/8552 over-height compact tension specimens, with a layup of $[90/45/0/\text{-}45]_{4s}$, using a High-fidelity Finite Element Method (Hi-FEM) model. Cohesive interface elements were used to simulate potential delamination and fibre splitting, with the Weibull fibre failure criterion employed to model fibre failure. Fairly consistent results were observed between the Hi-FEM model and scaled-down OCT tests, with the Hi-FEM results showing many small incremental load-drops and crack propagation; whereas the load drops found in experimental tests are less frequent with larger magnitude. To accurately determine the R-curve, the definition of crack increment Δa needs to be established. In the past, crack lengths have often been defined by the distance from the tip of the 0° fibre breakage to the initial crack tip, shown in figure 2.15, however, Xu et al. argued that the crack length should only be considered when all the plies through the whole thickness are broken, i.e. there are no ±45° plies intact, known as the real crack length. As such, real crack length is always shorter than that of the effective crack length. It was suggested that effective crack length α_{eff} is equal to the sum of real crack length α and fracture process zone length l_{FPZ}. By using the real crack length to calculate the fracture energy, the R-curve starts from a non-zero value and is in good agreement with previous independent tests. The obtained R-curve shows a tendency to plateau as the crack length increases, however, more tests at larger sizes are needed to verify such a claim. With the new Hi-FEM model and true crack length established, the R-curves for other stacking sequences can also be investigated in future work.

A numerical study was carried out by Xu et al. [116] using the explicit code LS-Dyna to study the progressive damage development at the notch tips. Sub critical damage such as fibre splits and delamination were modelled by cohesive interface elements, while fibre failure was governed by a failure criterion based on Weibull statistics. Centre notch specimens were used for both the numerical simulation and experimental validation. Results suggest a high degree of correlation between modelling and experiments, provided that the gaps between virtual splits are less or

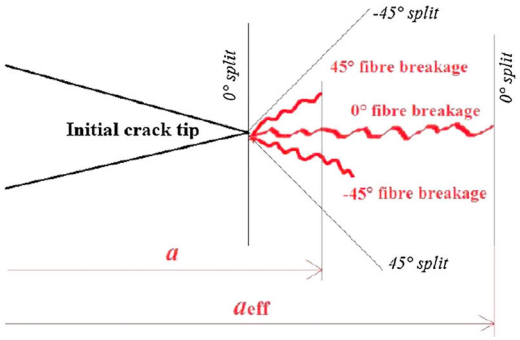

Figure 2.15: Schematic of true crack length α and effective crack length α_{eff}, [14].

equal to 1 mm and that the mesh size is no larger than 0.2 mm. It was also concluded that delamination and splitting are both energy driven rather than stress driven. As the notch length increases, the tensile strength approaches the value determined from linear elastic fracture mechanics due to the predicted damage zones approaching an approximately constant size as the simulated specimens get larger.

2.5 Conclusion

A diverse range of approaches for the characterisation of translaminar fracture has been reviewed in this chapter. Numerous specimen configurations, sizes and data reduction schemes have been used. These innovative methods were the achievements of many researchers, all of whom are motivated by the difficulty in triggering the desired failure mode and obtaining accurate results.

For tensile testing, although a general consensus towards data reduction has not been settled, but a specimen suitable for all material systems and lay-ups can be derived from the current CT and over-height CT configurations.

Characterisation of toughness for compressive failure exhibits more issues with some researchers work published in this domain. Kuhn et al. [114] presented a feasible methodology, however, more robust testing and verification are needed.

In relation to the current thesis, previous work by Xu et al. [11] investigated the initial fracture response of large stiffened composite panels using OCT coupons which has left a gap for the current project to fill - trying to predict the full fracture response of the same large stiffened composite panel. The two key differences between the approach adopted in the current thesis and ref [11] are taking account of the full fracture response rather than the initial response, and carrying out extensive new experimental work to better understand the R-curve and the effect of skin-stringer interaction. To capture and predict the full fracture response, the following issues, which were not present in the previous study, need to be addressed

- Skin crack and stringer interaction. To assess the full fracture response, it is necessary to establish the behaviour of a skin-crack/stringer interaction. Does the stringer crack along

with the skin or does the stringer debond from the skin but stay intact? This question would need to be investigated to establish the full fracture response. It is proposed to investigate this issue experimentally via some stiffened OCT tests.

- Scaling effects. The panel that is being predicted is 750 mm by 900 mm, which is significantly larger than the conventional coupons tested. With such a large panel comes the potential issue of scaling effects. Would the trends observed from the small coupons still be valid on a large panel, where the crack itself could be multiples of the size of the coupons. Therefore it is necessary for this thesis to address any potential scaling effects from small coupons to large panels.

- The R-curve shape and its effect on the fracture response. The previous study in ref. [11] addressed the crack initiation point on a R-curve, but lacked the remaining R-curve. While this was sufficient for the previous study, to predict the full fracture response the full R-curve would need to be established. The shape and plateau value are two items which need particular attention.

- Modelling method. The modelling method plays a vital role in determining not only the capabilities of the model but the computational cost also. A previous work by Xu et al. [14] employed a High-fidelity Finite Element Method (Hi-FEM) model to deduce the R-curve for translaminar fracture. While the Hi-FEM model provided satisfactory results it was relatively computationally expensive. To suit the needs for industrial applications, a more cost effective approach is required. It is proposed to employ VCCT in conjunction with cohesive elements, which ought to provide accurate results while being relatively computationally efficient.

CHAPTER 3

CHARACTERISATION OF FRACTURE BEHAVIOUR IN STIFFENED OCT SPECIMENS

3.1 Background

Much research has been carried out using finite element analysis to investigate the effect of crack propagation in stiffened panels. Vitali et al. [129] proposed a combination of a high-fidelity analysis model with a low-fidelity model to determine the crack propagation constraint in the design optimisation process. While numerical results exist, there is still a great need for some experimental input to serve not only as a comparison but to investigate the actual damage process and mechanism, especially the interaction between translaminar fracture and stringers. There has been some previous experimental research with stiffened OCT panels by Takeda et al. [11], where a very limited number of specimens with thin and thick stringer foot have been tested but not much information has been published. Figure 3.1 shows all of the data that can be accessed from Takeda's research. To better understand the interaction of crack propagation within stiffened panels, it is necessary to carry out a full set of experiments with 0.5 mm and 2 mm thick stringers. The values of 0.5 mm and 2 mm have been chosen based on two factors - firstly they provide a good variation in thickness, and secondly these two stringer foot thickness values have been used in previous stiffened OCT tests ([11]) which provides an additional source of comparison. A new set of complete test results with many specimens would enable a more in-depth data analysis and be more statistically convincing. The damage process when a translaminar fracture in the skin encounters a stringer and the damage mechanism is of particular interest to this PhD project as it would provide some useful information that can be applied to the ultimate goal of predicting the response of a large stiffened composite panel. The plan was to carry out two sets of tests, with 4 mm thick skin, and 2 mm or 0.5 mm stringers. The stacking sequence was $[45/90/\text{-}45/0]_{4s}$ for

the skin, [45/90/-45/0] for the 0.5 mm stringer, and $[45/90/-45/0]_4$ for the 2 mm stringer. These configurations have been chosen based on previous studies [11] to provide a source of comparison.

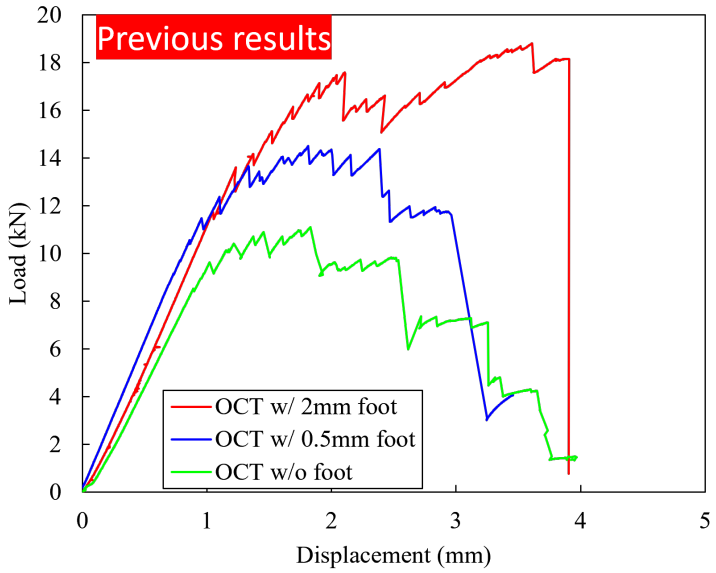

Figure 3.1: Previous stiffened OCT experimental results by Takeda et al..

3.2 Specimen details and test set-up

Two panels were layed up, both of which have a skin thickness of 4 mm, and a stringer thickness of 0.5 mm and 2 mm respectively on both sides of the panel. Each panel can be cut into eight individual stiffened OCT specimens, dimensions of the specimen is shown in figure 3.2.

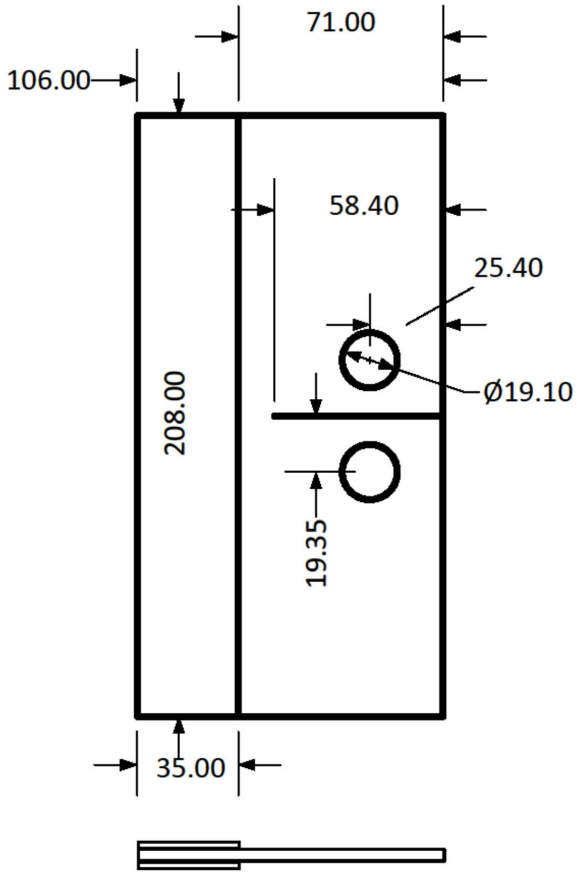

Figure 3.2: Dimensions of the stiffened OCT specimens, all dimensions in mm.

The in-plane stiffened OCT specimens were tested in a hydraulic-driven Instron 100 kN test machine under displacement control at a rate of 1 mm/min. No anti-buckling rods were attached to the rear end of the specimen as no buckling failure was observed. Interrupted tests in which each specimen was unloaded after certain load drops (2–3 load levels) on the respective load-Pin Opening Displacement (POD) curves were carried out to study the failure mechanisms via CT scanning. The specimens from the interrupted tests were soaked in a bath of zinc iodide penetrant for at least 3 days. A Nikon XT H 225 ST CT scanner was used for damage evaluation. It has a 225 kV, 225 W microfocus X-ray source and a 3-μm focal spot size. Figure 3.4 gives an overview of the test set-up. The specimen was loaded via two loading pins inserted into the two loading holes, while the loading jigs were clamped by the test machine crosshead. The loading pins are cylindrical and have a smooth contact surface with the specimen loading holes, with threads on either ends of the pins for tightening nuts. Care was taken during the tests to make sure the top and bottom crosshead were aligned properly and parallel to each other. Load and crosshead displacement readings were provided by the test machine, while a video gauge was employed to measure the POD throughout the test to serve as an independent source for the displacement

reading. The material used was Hexcel's HexPly® IM7/8552 carbon/epoxy unidirectional pre-preg with a 0.125 mm nominal cured ply thickness. The stringers were layed-up on to the skin before any curing took place, with spacers of the same thickness as the stringers inserted at areas without the stringers to make sure the whole panel had a flat surface front and back. The spacers were made from the same Hexcel IM7/8552 pre-preg with the same thickness as the stringers. A thin layer of release film was placed in between the skin and the stringers to enable the spacers to be easily removed after curing. Figure 3.3 shows the arrangements of the eight specimens on one panel, the area shaded in red represents the location of the spacers. Once the whole panel was layed up, stringers and spacers included, it was sent to the autoclave and cured all in one go according to the manufactures recommendations.

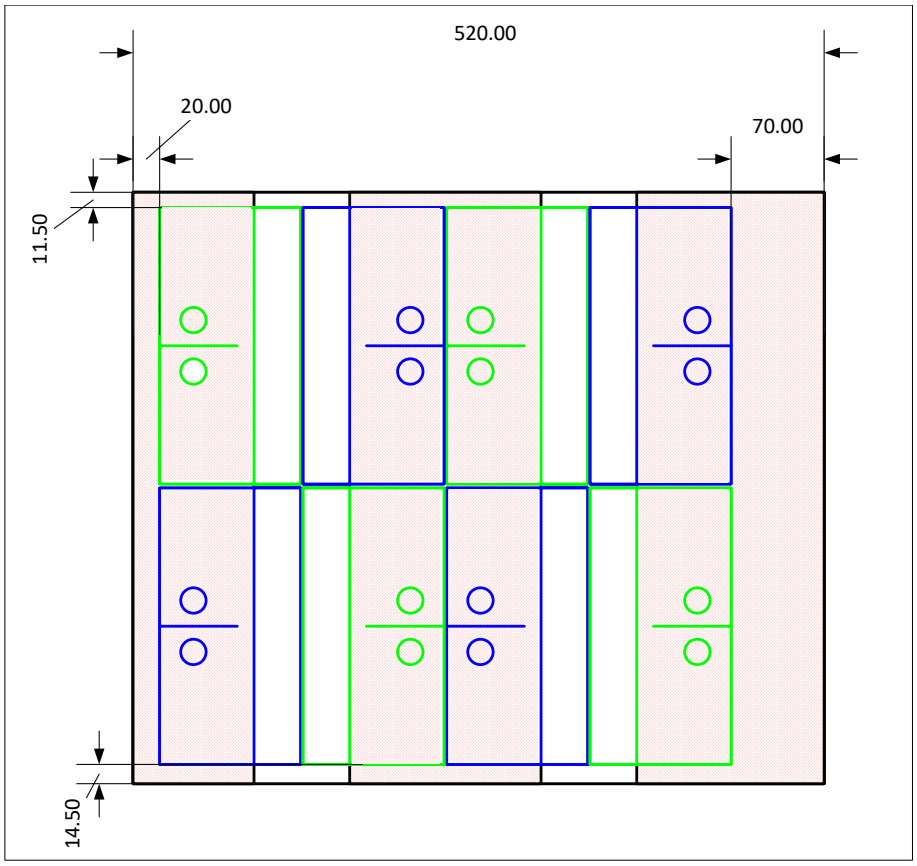

Figure 3.3: Schematic showing the lay-out of the eight specimens on one panel, the red shaded areas indicate the location of the spacers. Dimensions in mm.

For each set of tests, three tests-to-failure (uninterrupted) and four interrupted tests were carried out. The purpose of the uninterrupted cases is to have a baseline of the behaviour of the specimens and assess the repeatability, while the purpose of the interrupted tests was to assess the damage sequence during the test and investigate the damage morphology at different stages by CT scanning.

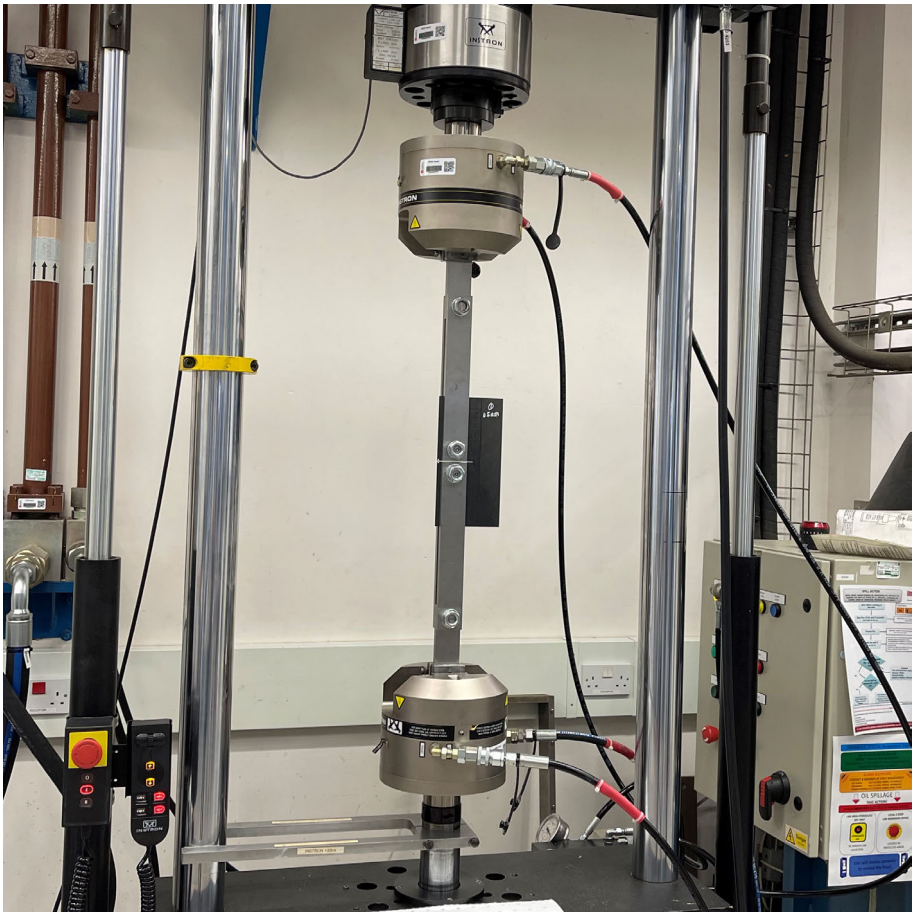

Figure 3.4: Stiffened OCT test machine set up.

3.3 Test results

Three test-to-failure cases were carried out for each set of specimens, the load-POD curves of the uninterrupted results can be found in figure 3.5 and figure 3.6 for the 0.5 mm stringer set and the 2 mm stringer set respectively. In both stringer thickness cases, the loads increased linearly at the beginning until load-drops started occurring. The 2 mm stringer set yielded a higher initial stiffness than the 0.5 mm stringer set. One of (SP3) the three 0.5 mm stringer test specimens displayed a higher initial stiffness compared to the remainder two (SP1 and SP2), which is likely to have been caused by the installation of that particular specimen causing it to have less slack in the loading jig compared to others. Peak load occurred approximately at 12 kN for the 0.5 mm stringer cases and at 18 kN for the 2 mm stringer cases. Fracture in front of the notch occurred when significant load drops appear on the load-POD curves. For the 0.5 mm stringer sets, fracture started occurring at approximately 1.6 mm displacement, whereas for the thicker 2 mm stringer sets, fracture occurred earlier at around 1.4 mm displacement. Both the 0.5 mm stringer specimens and 2 mm stringer specimens exhibited compressive failure at the

back, away from the notch, though they are of different forms - the 0.5 mm stringer specimens exhibited a crack at the back of the specimen without skin-stringer delamination, while the 2 mm stringer specimens did not crack, but rather delaminated and buckled, shown in figure 3.7. As a result, the unloading pattern displayed on the load-POD curves are drastically different between the 0.5 mm specimens and the 2 mm specimens. The 0.5 mm stringer specimens exhibited a gradual unloading pattern where multiple load-drops occurred, each reducing the load by a margin. Whereas the 2 mm specimens' unloading pattern was much more sudden as all three test-to-failure specimens yielded a very sudden failure causing the load to drop instantly. The 2 mm stringer specimens failed at a slightly lower displacement value than the 0.5 mm stringer specimens, approximately 4 mm and 4.5 mm displacement respectively. No significant differences were found between displacement values produced by the video gauge and the test machine cross-head displacement, suggesting the test machine set-up remained relatively stiff under the load levels of this test. Figure 3.8 shows a comparison of the load-displacement curves produced by the test machine cross-head and the video gauge of the 0.5mm SP2 specimen. It can be seen that they yield very similar results. Generally, the load-POD curves from both sets demonstrated a good consistent trend among themselves, both before cracks reached the stringer and after.

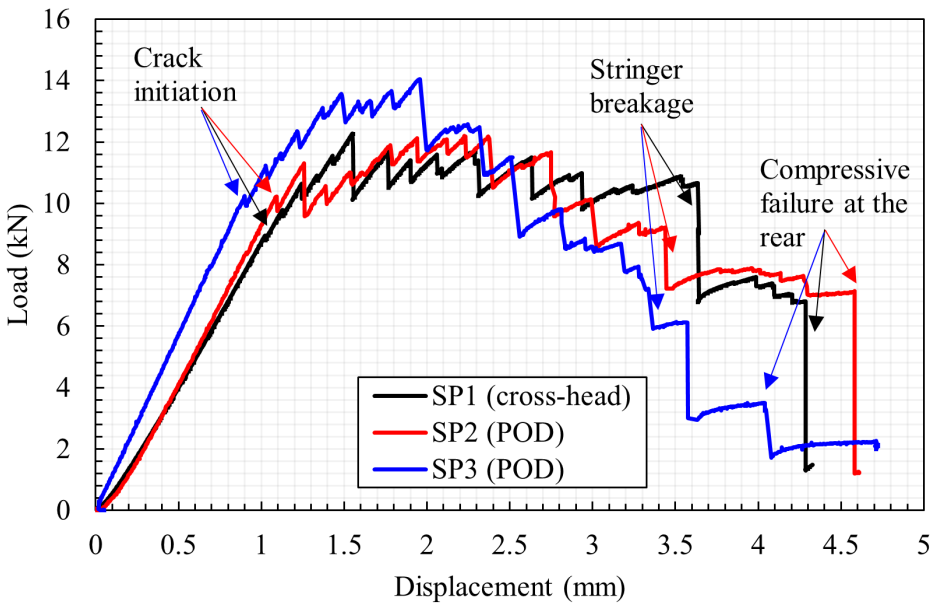

Figure 3.5: Load-POD curves for 0.5 mm stringer specimens, test to failure.

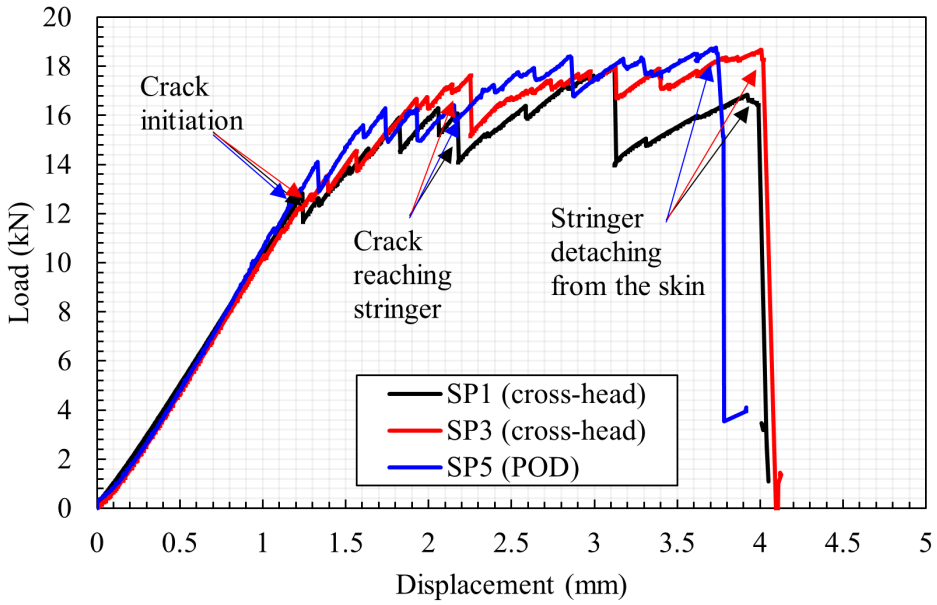

Figure 3.6: Load-POD curves for 2 mm stringer specimens, test to failure.

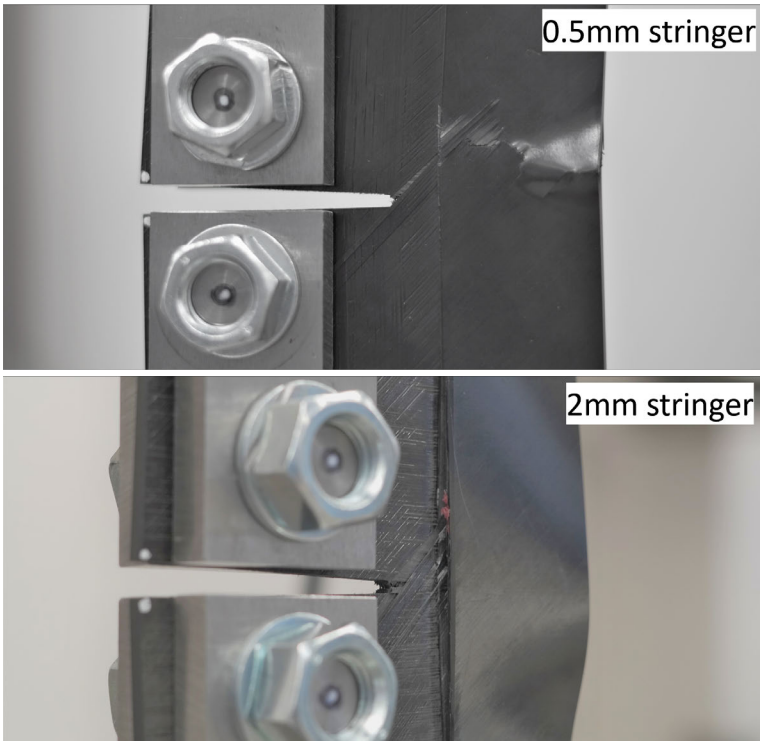

Figure 3.7: State of the specimens after compressive failure.

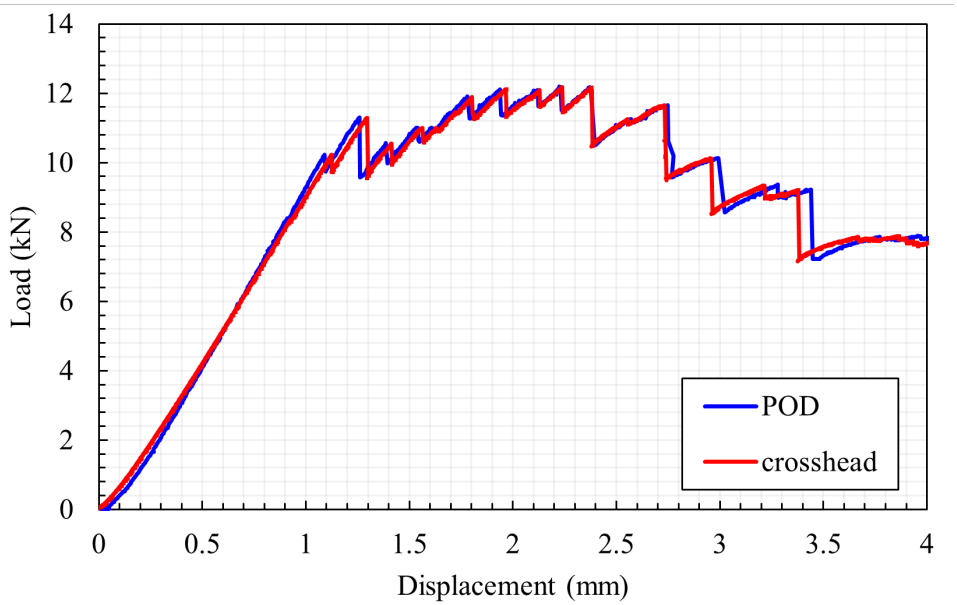

Figure 3.8: A comparison of the load-displacement curves produced by the test machine cross-head and the video gauge Pin Opening Displacement (POD). Results show minimal difference between the two methods.

With the uninterrupted tests established, four interrupted tests were carried out for each specimen set. The aim of the interrupted tests is to capture the damage state of the specimen during the crack propagation process, and to be able to observe further via CT scanning. To achieve this, tests were interrupted throughout the test duration with the goal being to have an interrupted sample for every significant load-drop. Figure 3.9 and 3.10 show the interrupted Load-POD curves for each set. The locations of interruptions were determined based on major load drops and displacements. Firstly, the interrupted points need to be spread across the full displacement range, and secondly, if possible, the interruption should take place just after a major load drop.

The four interrupted tests for the 0.5 mm stringer specimens were at displacement values of 1.6 mm, 1.9 mm, 2.8 mm, and 3.5 mm with the typical failure displacement being 4.3 mm. The first interruption point with a displacement value of 1.6 mm took place just before the typical first major load drop. The second interruption point at 1.9 mm took place just after the first major load-drop. The third interruption points were chosen approximately half way through the displacement range. And the fourth interruption points were chosen just after the second major load-drop, where load levels have dropped to about half of the typical peak value but still some distance away from the final failure.

Turning to the 2 mm stringer specimen sets, the four interrupted locations were at 1.8 mm, 2.5 mm, 3.0 mm, and 3.6 mm. The first interrupted location at 1.8 mm POD was chosen as it was just after the first major/peak load-drop. The second interrupted location at 2.5 mm POD was chosen as it is approximately half way through the POD range. The third interrupted location at

3.0 mm POD was chosen due to it being just prior to the second major load-drop in specimen 1 (SP1). And the last interrupted location at 3.6 mm POD was chosen just prior to the final failure took place in SP1.

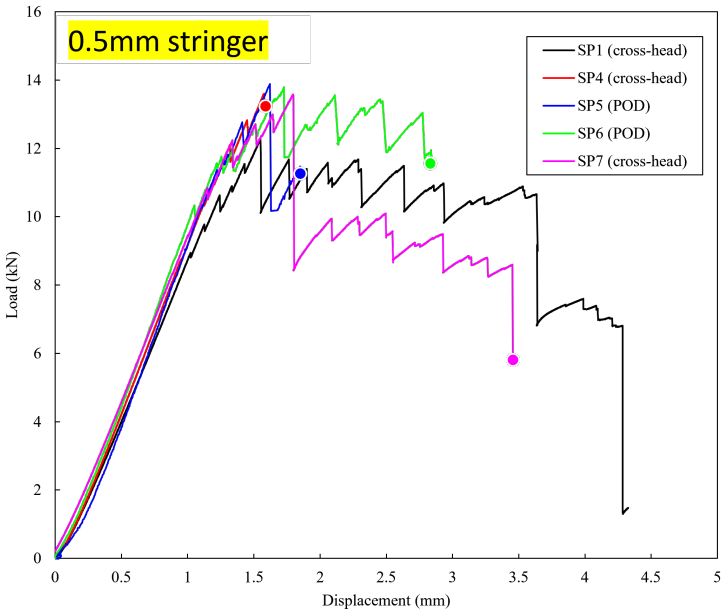

Figure 3.9: Load-POD curves for 0.5 mm stringer specimens. SP1 - test-to-failure; SP4,5,6,7 - interrupted.

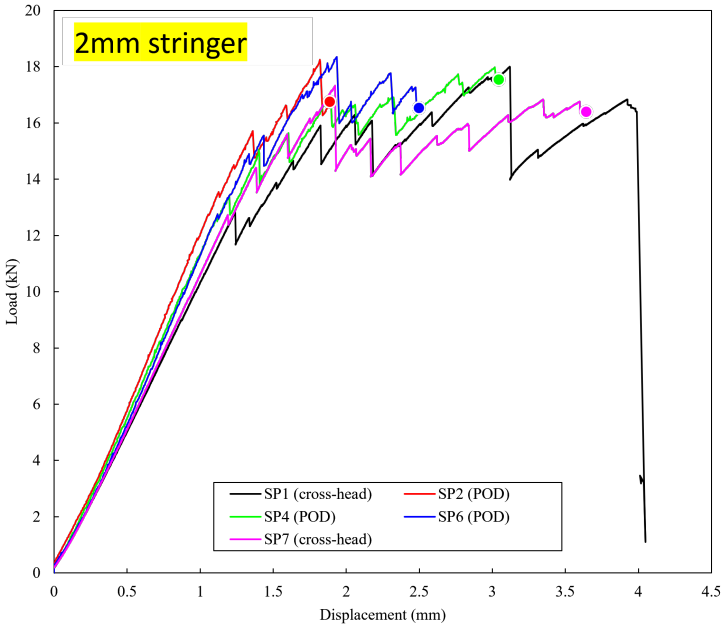

Figure 3.10: Load-POD curves for 2 mm stringer specimens. SP1 - test-to-failure; SP2,4,6,7 - interrupted.

3.4 Analysis

By checking the CT scan images of the interrupted tests, shown in figure 3.11 and 3.12, the damage state of the skin-stringer interface can be compared across the full displacement range. The CT scan images shown were taken at the skin surface - where the skin-stringer interface was located.

3.4.1 0.5 mm stringer samples

Despite some clear splitting in the surface 45 plies in SP4 & SP5, it is clear that delamination has not yet propagated into the stringer just after the peak load. Peak load was achieved when no damage occurred in the stringers, and load drops occurred due to damage propagation. The test to failure cases show that ultimate failure of the 0.5 mm stringer samples includes compressive failure in the stringer towards the back of the specimen. However, such damage can not be found up until SP6 (11 kN at 2.8 mm). The CT image of SP6 clearly indicates a large area of delamination between the skin and stringer, however, upon inspection of the stringer, there was no damage found in the stringer itself.

Turning to SP7, while delamination in the skin-stringer interface gets even larger, it differs to SP6 in that there is a clear cracking taking place in the stringer. SP7 is a unique case as far as damage morphology is concerned as it is the only specimen which contains stringer cracking without compressive failure at the back. Stringer cracking occurred in all of the three test-to-failure cases (SP1, SP2, & SP3), but the stringer cracking in the test-to-failure cases were all accompanied by compressive failure at the back. Figure 3.13 shows a comparison of the stringer damage state for SP6, SP7, and SP1, the sequence of damage can therefore be confirmed -

1. Crack propagating in the skin and keeps on propagating underneath the stringer.

2. Skin and stringer debonding due to the crack in the skin, the stringer is still not damaged. Area of debonding increases as the loading process continues.

3. Due to the large area of skin-stringer debonding and fracture in the skin, much of the load which was taken by the skin is now transferred to the stringers.

4. Compressive failure at the back of the specimen is the ultimate failure observed in the test-to-failure cases.

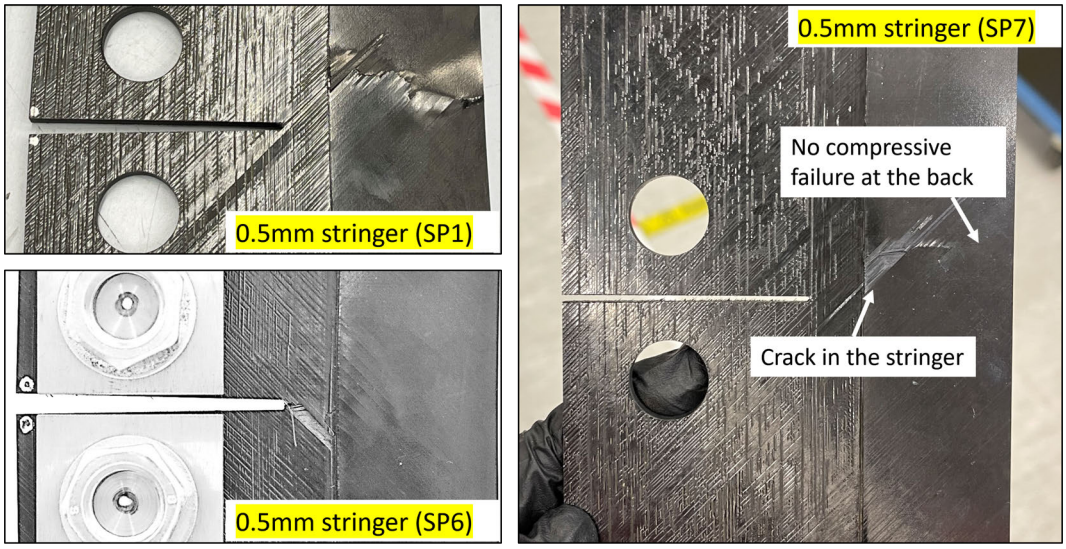

Figure 3.13: Damage state of the specimen surface for SP1, SP6, & SP7 (0.5 mm stringer case).

3.4.2 2 mm stringer samples

The uninterrupted tests for the 2 mm stringer specimens showed some severe skin cracking and skin-stringer debonding with no sign of stringer cracking. This finding is confirmed through CT scan images of the interrupted tests - none of the four interrupted specimens exhibited stringer cracking. The stringers in this case were acting as a crack stopper where the crack is unable to propagate into the stringers. Similar to the 0.5 mm stringer cases, delamination is the main damage mechanism, but it occurs at a much earlier stage. The CT image in figure 3.12 indicates that delamination occurred underneath the stringer as early as SP2 (1.8 mm displacement), which is much earlier than what is seen in the 0.5 mm stringer cases (2.8 mm displacement). As the load and displacement increase through testing, the delamination area also increases.

Furthermore, test-to-failure cases such as SP1 demonstrated some very significant skin-stringer debonding, to the extent that they are almost detaching from each other. However, such behaviour was not observed in any of the interrupted tests, even SP7. Such a difference in damage morphology can be supported by the CT image in figure 3.12 where there is no sign of delamination at the back of the specimen in SP7. In addition, figure 3.14 shows the damage state of SP1 (test-to-failure) and SP7 (interrupted just before failure), it is clear that the severe skin-stringer detaching/bulging seen in SP1 is not present in SP7. This observation confirms that the delamination of the stringer is what caused the final failure, and that when the stringer is 2 mm thick, stringer cracking does not occur.

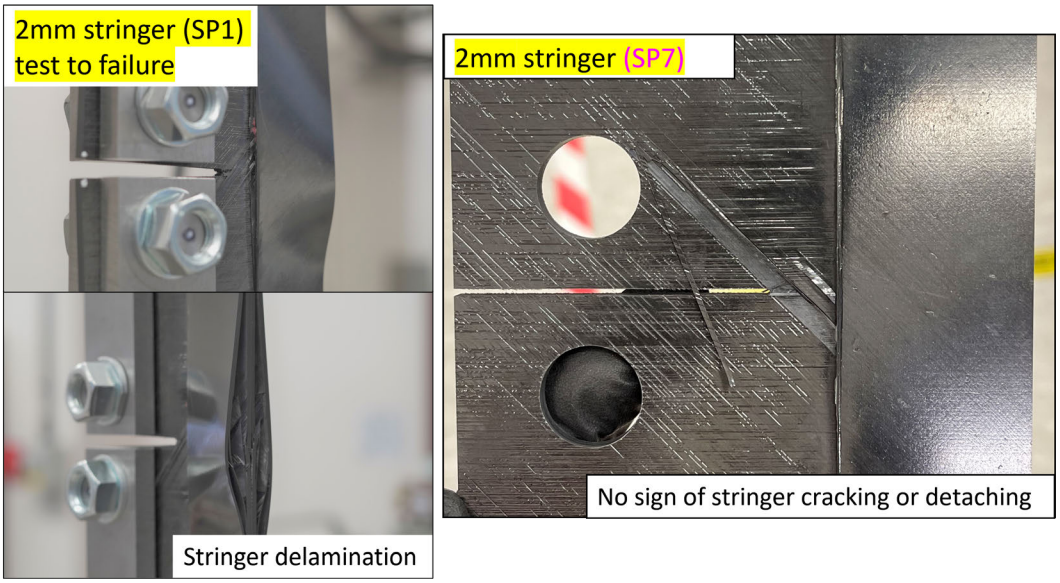

Figure 3.14: Damage state of the specimen surface for SP1, & SP7 (2 mm stringer case).

3.4.3 Discussion

Xu et al. [8] published tensile test results of unstiffened OCT specimens of three different sizes – scaled down, baseline, and scaled up. The baseline set from [8] is of value to the current study as the specimen geometry is identical to the stiffened OCT specimen tested here, except without the stringers. Figure 3.15 shows a comparison between the typical stiffened OCT and baseline OCT load-POD curves. Both stiffened OCT results exhibit higher peak load values, and for the 2 mm stringer cases only, a lack of the gradual load-decreasing trend that is present in the baseline OCT specimens. The higher peak load shows that the stiffened OCT specimen is much tougher than the unstiffened OCT specimen. The lack of the load-decreasing trend in the 2 mm stringer cases can be attributed to two factors - a strong R-curve effect and the load being transferred to the stringers as the crack propagates in the skin, a mechanism that does not exist in the unstiffened OCT specimens and to a lesser extent in the 0.5 mm stringer cases. Without the stringers, there is a clear gradual load-decreasing trend, with the 0.5 mm stringers, peak load can be maintained for a substantial proportion of the test and then starts to decrease quickly. Whereas the 2 mm stringer specimens exhibit a 28% increase in load (from 14kN to 18kN) as the test progresses and reaches its peak load towards the end of the displacement range. Such differences in the load-decreasing trend proves the hypothesis that as the crack propagates in the skin, load is being transferred to the stringers. A thicker stringer that is capable of withstanding higher tensile loads enables the specimen to reach even higher loads than the crack initiation load, while specimens without stringers have nowhere to redirect the load lost by the skin fracture hence the gradual unloading trend. And the specimen with 0.5 mm stringer is in the middle ground where the stringers can take some redirected load but eventually fail in tension.

3.5 Conclusion

To conclude, a comprehensive set of results for the Over Height Compact-tension (OCT) specimens with IM7/8552 materials has been presented. The results consist of a set of specimens with 0.5mm stringer foot thickness and a set with 2mm thick stringer foot. Both stringer foot thickness specimens exhibit delamination to some extent, while only the 0.5 mm stringers exhibit stringer breakage. The extent of delamination is greater on the 2 mm stringer cases than the 0.5 mm cases. The observed damage mechanism of the stringer is tensile failure, and not crack propagation.

Key findings for the 0.5 mm stringer specimens are -

1. Compressive failure at the back of the specimen causes the ultimate failure
2. Fracture occurs across the full width of the stringer at ultimate failure.
3. Breakage in the stringer occurs nearer the notch first, followed by compressive failure at the back.
4. Stringer breakage is caused by excessively high tensile stress due to load being transferred from the skin to the stringers as a result of skin-stringer debonding and skin fracture.

Key findings for the 2 mm stringer specimens are -

1. Stringer breakage never occurs in the 2mm stringer specimens, even ones tested to failure.
2. Instead, large areas of delamination can be seen at the skin-stringer interface.
3. Ultimate failure is caused by the total delamination of the stringer, and the stringer bulges out.
4. The damage morphology is distinctively different from the 0.5mm cases.

When a crack propagates in the skin underneath the stringer, one of two things happens – delamination propagation only or delamination along with stringer breakage. Which happens depends on the thickness and strength of the stringers - with thicker stringers acting as a crack stopper where the crack is unable to propagate into the thick stringers. The load-carrying capability of the skin decreases as fracture propagates through it, therefore an increasing amount of load is transferred to the stringers. When the stringer is relatively strong or of sufficient thickness, it can withstand more of the load that is transferred - reducing the crack propagation in the skin. On the other hand, when the stringer is not of sufficient strength or thickness, it fails in tension as the load gets transferred to it, reducing the overall load-carrying capability of the specimen compared to specimens with thicker stringers. Such tensile failure is what has been observed in the uninterrupted tests of the 0.5 mm stringer specimens.

Overall the new stiffened OCT results from the current study combined with the previous unstiffened OCT results by Xu et al. have formed a coherent and convincing argument regarding

the damage mechanism for translaminar fracture in stiffened structures. And these new findings will contribute to the validation of a cost-effective modelling method for translaminar fracture prediction in large stiffened panels.

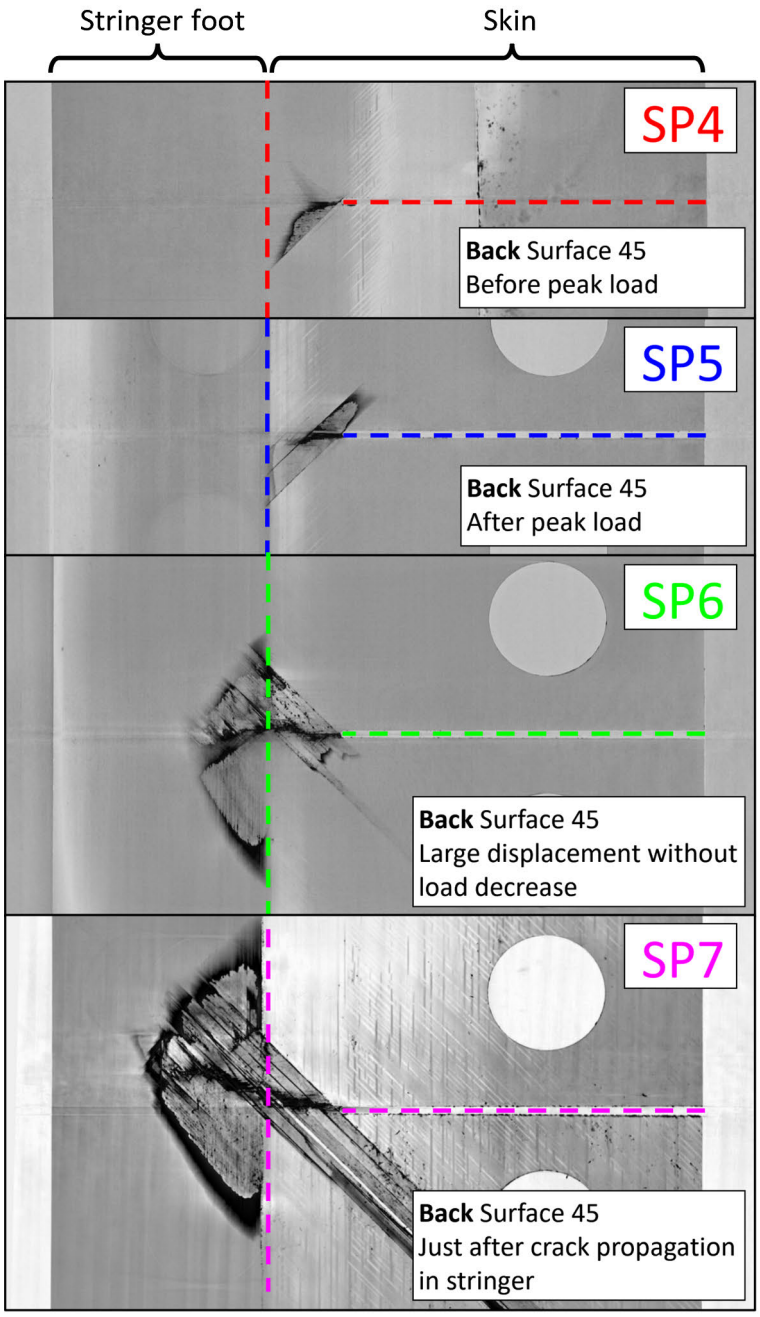

Figure 3.11: CT images of the skin-stringer interface from interrupted tests, 0.5 mm stringer samples. Dashed vertical lines represent the edge of the stringer foot, dashed horizontal lines represent the location of the machined notch. Crack propagates from right to left as shown in the CT images.

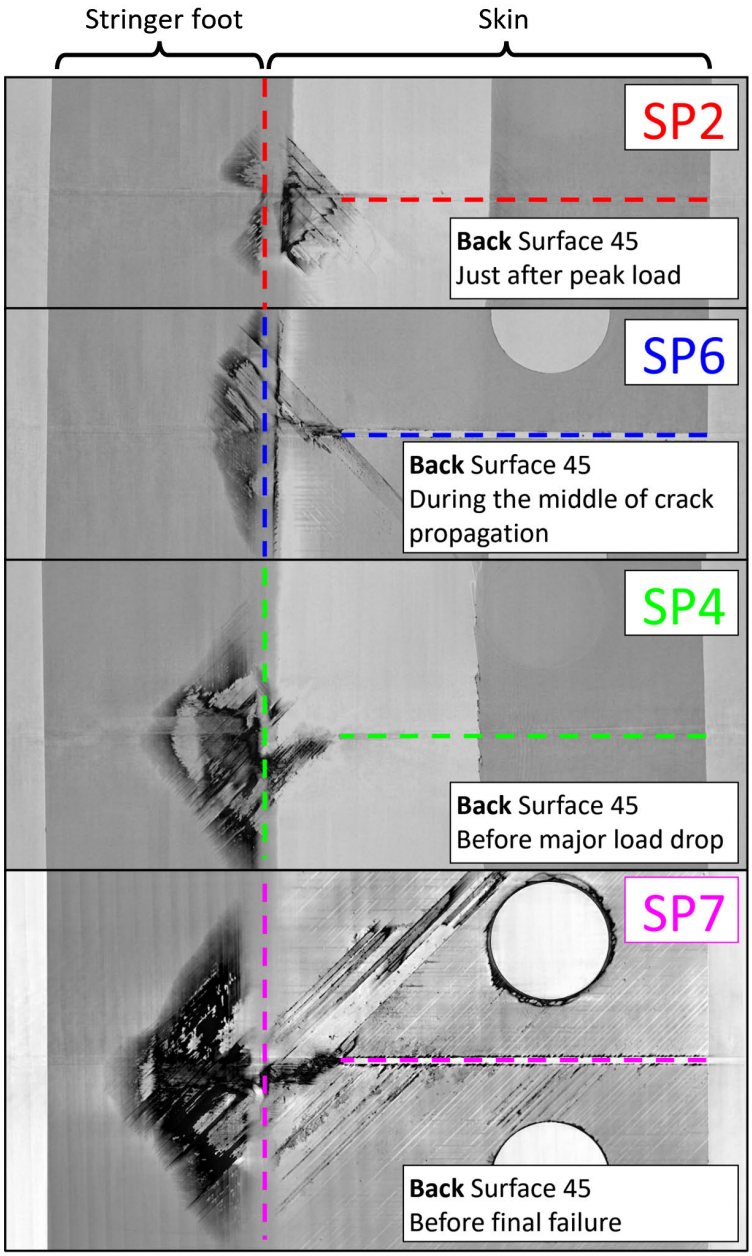

Figure 3.12: CT images of the skin-stringer interface from interrupted tests, 2 mm stringer samples. Dashed vertical lines represent the edge of the stringer foot, dashed horizontal lines represent the location of the machined notch. Crack propagates from right to left as shown in the CT images.

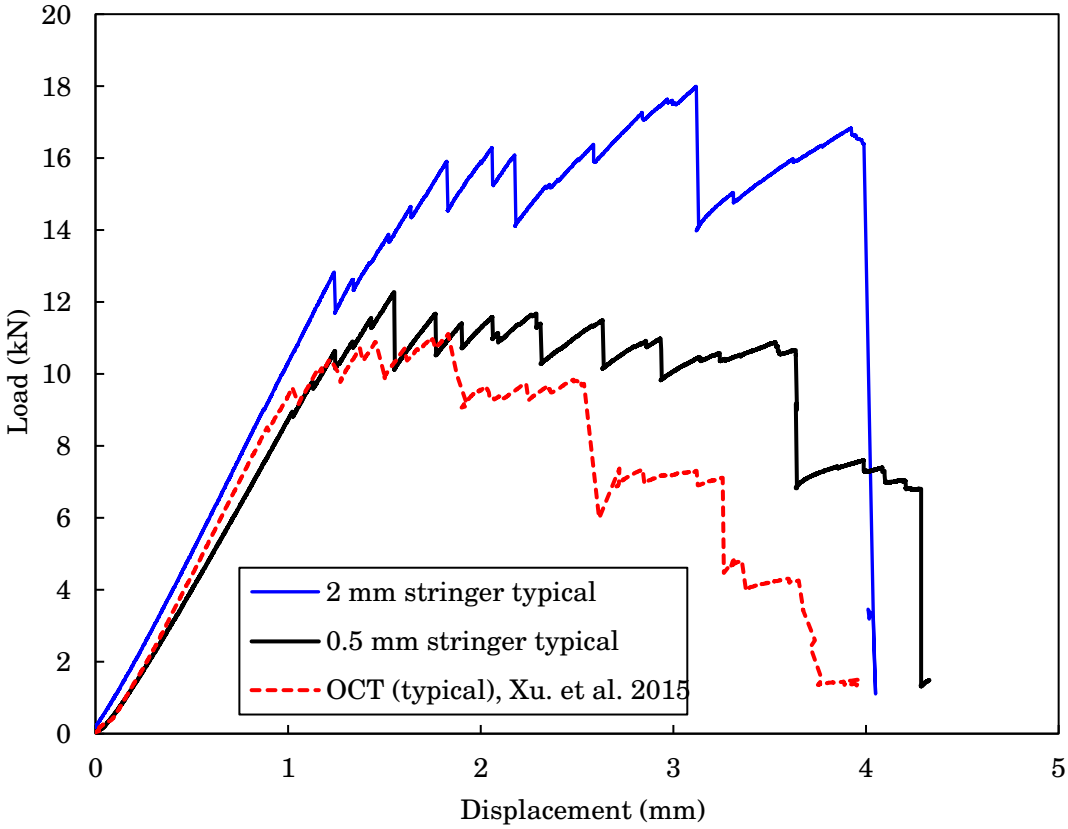

Figure 3.15: Load-POD curves of stiffened OCT specimens compared to unstiffened OCT specimens, data from Xu et al. [8].

CHAPTER 4

R-CURVE CHARACTERISATION OF NON-CRIMP FABRIC (NCF) MATERIAL.[1]

4.1 Background

The ultimate goal of the PhD project is to develop a cost-effective modelling method for translaminar-fracture propagation in stiffened composite structures under tension. The previous chapter made a step towards the ultimate goal by investigating experimentally the interaction of skin crack and stringer by means of stiffened over-height compact tension tests. Much valuable test data were collected and the damage mechanism between translaminar fracture and stringers was established. It was reported that the stringer breakage is dependent on the relative tensile strength of the stringers, and the magnitude of the load that is being transferred from the skin. While the damage mechanism and interaction have been investigated, there is still a piece of the puzzle missing - that being the establishment of the resistance-curve (R-curve), how the critical strain energy release rate changes as a function of crack propagation. There has been a lot of previously published research on translaminar fracture R-curve in composite materials [13, 79, 82, 98, 130]. While these results all have their merits in their own rights, unfortunately, they are of limited use to the current project as they are either cross-ply specimens or of a different material system to the current study.

To achieve a more accurate modelling result, the full R-curve of the material concerned needs to be established. The material for the large stiffened panel that is to be modelled is a custom non-crimp-fabric material developed and used by the Japan Aerospace Exploration Agency (JAXA). Being custom means there is only a limited number of literature or test data publicly available for this particular material. But fortunately, there were two spare panels from

[1] Parts of this chapter were previously published by *Elsevier* in the journal of *Composites Communications* [10].

JAXA of the same NCF material that was available to be used for this PhD project. These two panels would permit experimental tests to be carried out to determine the R-curve of this NCF material, which would be of paramount value to the construction of a cost-effective modelling method.

Two sets of tests were carried out with the NCF material, one set employed the Eccentrically loaded Single-Edge-notch Tension (ESET) specimen while the other set employed the compact tension specimen. This chapter records the test methods and reports the test data, followed by some data analysis.

4.2 Eccentrically loaded single-edge-notch tension (ESET) specimen test

To establish a R-curve, the knowledge of crack length throughout the test is vital. One method for R-curve characterisation is to carry out multiple interrupted tests across the full displacement range, such that an R-curve with a reasonable crack length range can be obtained. The issue with this approach is that it requires the data from multiple specimens to draw one curve - time-consuming and costly. To resolve this issue, in-situ computer tomography (CT) scan could be employed. In-situ CT scan uses an X-ray scanning machine that is built around the test machine that enables the specimen to be CT scanned while still on the test machine, even under load. This real-time CT scan capability would enable the monitoring of the internal crack status throughout the test duration, without having to unload or remove the specimen. Traditionally, assessing the internal damage status via CT scanning would require multiple specimens to carry out many interrupted tests, where tests are stopped at pre-defined intervals throughout the displacement range to assess the damage progression through time. With in-situ CT scanning, it would be possible to achieve the same result with one specimen. Not only would this reduce testing cost, it would also promote a more continuous test result since the data were collected from one specimen - alleviating any potential deviations caused by minor test specimen imperfections. However, the in-situ CT scan machine that was available to use for this study had some limitations to the specimen geometry and test method. Since the X-ray machine needs to rotate around the specimen for scanning, hence a narrow/slender specimen was preferable since having the X-ray source and the CT-scan camera close to the centre of rotation means a higher scanning resolution and a better image quality. There are a number of test specimens that have been used for translaminar fracture testing, however, there are only some which can sustain a stable crack growth - a prerequisite for full R-curve characterisation. As mentioned in chapter 2, only the compact tension, extended compact tension, three-point bending and four-point bending tests can yield stable crack growth, shown in figure 2.8. With these requirements in mind, the single edge notched tension specimen is proposed due to its slender form factor and the fact that it is the specimen geometry recommended by ASTM E1922 [105] for translaminar fracture toughness

characterisation of composite materials.

4.2.1 ESET specimen details and test set-up

The material was manufactured at JAXA through Vacuum-assisted Resin Transfer Moulding (VaRTM). The material used was bi-axial carbon Non-Crimp Fabric (NCF) made from STS-24k fibres by SAERTEX Co. KG, and the epoxy resin XNR6809/XNH6809 was manufactured by Nagase Chemtex Co. The stacking sequence used was $[(45/\text{-}45)/(0/90)]_{2s}$. The specimen dimension was in accordance with the requirements of the ASTM E1922 [105] standard. The nominal laminate thickness was 2 mm, compared with the measured average value of 2.18 mm. Specimen geometries, including the notch, were cut from a large panel using 1 mm carbide end mills on a Computer Numerical Controlled (CNC) router. Figure 4.1 shows the specimen dimensions of the ESET specimens and figure 4.2 and 4.3 shows the test rig assembly and scanning setup. The ESET specimens were loaded onto the test jig inside a polymer tube, loading pins were inserted into the two holes at each end of the specimen, as shown in figure 4.2. The whole loading tube assembly was then installed on the test jig and was brought closer to the radiation source during CT scanning, as shown in figure 4.3. The CT scanner used was a Shimazu inspeXio SMX-225CT FPD HR with a customised in situ test rig. The in situ CT scans were conducted at JAXA. The test was displacement controlled. During the initial linear loading phase, in-situ CT scans were performed at regular intervals while the tests were paused, and the displacement was kept constant. During each pause an in situ CT scan was carried out. After the initial linear loading phase, a scan was carried out as soon as a load drop occurred.

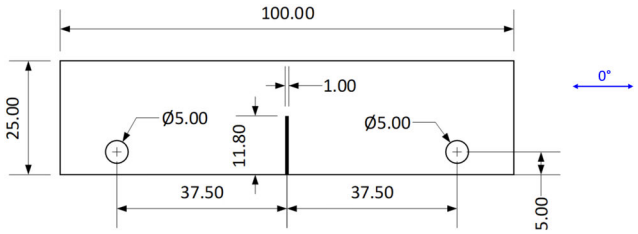

Figure 4.1: ESET specimen dimensions, used for characterisation of fracture toughness with in-situ computer tomography, dimensions in mm.

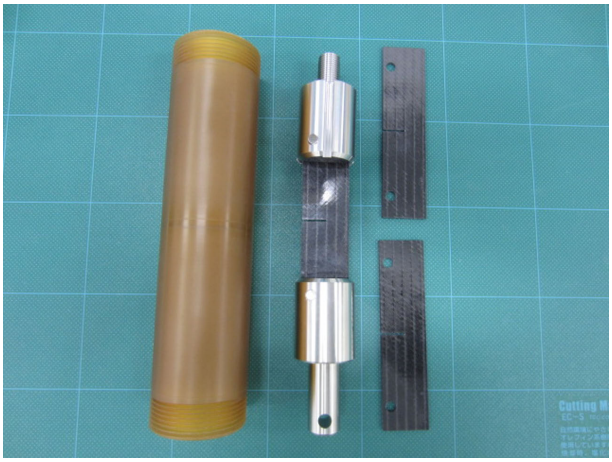

Figure 4.2: JAXA NCF material ESET specimen test rig assembly.

Figure 4.3: JAXA NCF material ESET specimen test jig set-up for scanning.

4.2.2 ESET specimen test results

Two NCF ESET specimens were tested using the in-situ CT scan method, figure 4.4 shows the load-displacement curves for these two tests. The following points can be deduced from the test results [10]:

- An approximately linear load-displacement relationship is apparent prior to the first load drop.
- A number of small incremental load drops were present before the catastrophic failure.
- Peak load and catastrophic failure did not occur at the same time - catastrophic failure occurred after the peak load. The large load-drops at 1.3 mm displacement and 1.2 mm displacement for SP1 and SP2 respectively correspond to the compressive failure of the rear of the specimen.

Slight load relaxations took place each time the test was paused for a CT scan. To avoid the load drops caused by load relaxation to be confused with actual load drops, the load relaxations have been removed from the load-displacement curves. The magnitudes of the load relaxation was very small (approx. 2%) and therefore it was reasonable to omit them. As during the pauses there were no further displacement increases and therefore there were no further damage to the specimen during the pauses. To back up this theory, a test previously carried out with IM7/8552 pre-preg with the same specimen geometries/dimensions using the same machine also showed very small load-relaxations [9], shown in figure 4.5. Therefore this is a reasonable assumption to be made.

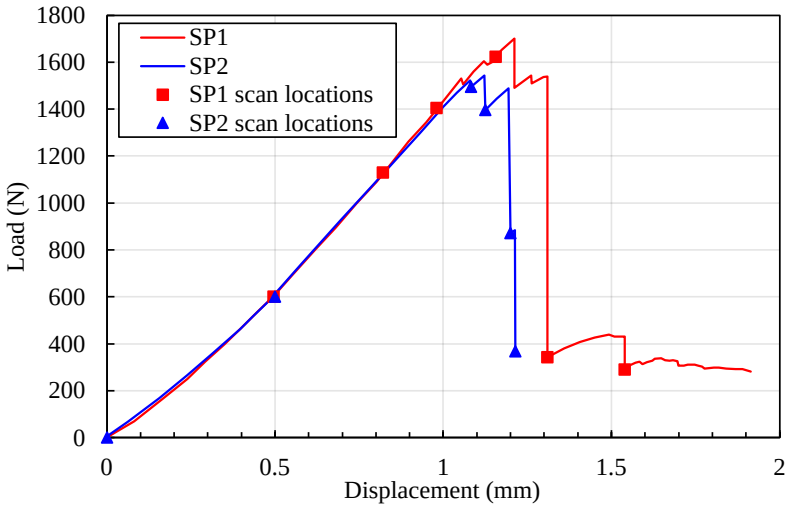

Figure 4.4: NCF ESET specimen load-displacement curves with pause locations.

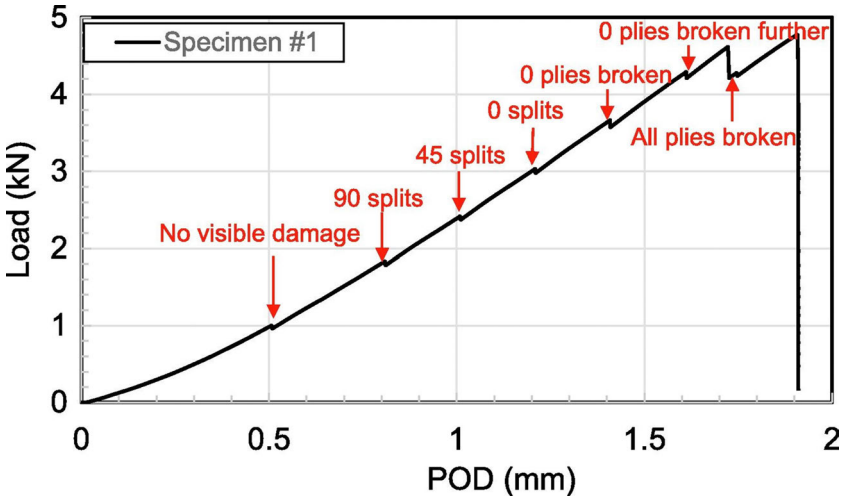

Figure 4.5: Raw load-displacement curve of a Eccentrically loaded Single-edge-notch Tension (ESET) specimen with identical dimensions to the JAXA NCF ESET specimens made from IM7/8552 pre-preg tested in the same test jig [9].

In figure 4.4 the in-situ CT scans are marked by rectangular and triangular markers. For every scan, a set of images through the material thickness were obtained. Figure 4.6 shows a set of typical in situ CT scan images for each ply orientation [10]. It should be noted that this set of images was taken from SP2 at 1.12 mm of displacement, which corresponds to the crack state just after the peak load. Based on these images, the damage state in the specimens is clearly visible. For example, in figure 4.6a), the crack in the 0° ply is clearly visible with nearly no splitting. Whereas in all of the 90°, -45° and 45° plies, limited fibre fracture could be observed, and damage mainly consisted of splitting, especially for the 90° ply where damage was splitting only [10]. No obvious delamination was observed except near the specimen surfaces in the current VaRTM processed NCF laminate.

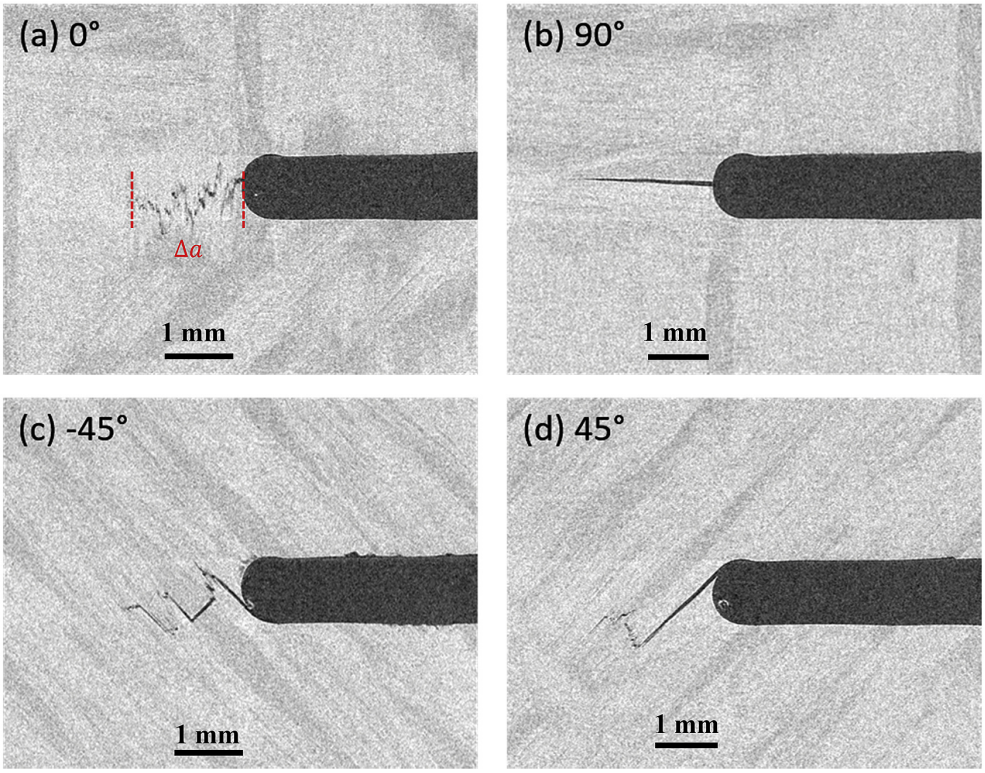

Figure 4.6: In-situ CT scan images of NCF ESET specimens [10]. Images taken from SP2 at 1.12 mm displacement. Δa indicates effective crack length. (a) 0°; (b) 90°; (c) -45°; (d) +45°. The in situ CT scanner used was a Shimazu inspeXio SMX-225CT FPD HR scanner, with a 5 kN load cell installed. The voltage used was 200 kV and the electric current used was 120 μA. The number of projections per scan was 2400 and the exposure time was 250 ms. The angle swept was 360°. The voxel size was 10 μm.

4.2.3 ESET specimen test analysis

With the in situ CT scan images established, an accurate correlation between the crack length and load can be deduced. The crack length were measured digitally using the CT scan data

analysis software VG Studios Max by VOLUME GRAPHICS. The crack length concerned in this study is the effective crack length - deduced by averaging the crack length of all of the 0° plies through the thickness. The advantages of employing the effective crack length have been investigated by Xu et al. [14]. There are two methods of defining the crack length - the true crack length, a, and the effective crack length, a_{eff}. The true crack length is defined as the distance over which all plies through the thickness are broken, which ideally happen simultaneously. But in reality some 45° plies still stay intact owning to the presence of delamination and splitting. To take the discrepancy of crack length caused by the intact ± 45° plies into account, it is proposed to measure the crack length by averaging the crack length of all 0° plies - named effective crack length, a_{eff}. In essence the effective crack length reflects the crack length which all plies are broken plus a fracture process zone. These ESET specimens were manufactured in accordance with the ASTM E1922 [105] standard, hence the data reduction method from it will be used -

$$K = \frac{P}{B\sqrt{W}} f(\frac{a}{W}) \tag{4.1}$$

where:

$$f\left(\frac{a}{W}\right) = \frac{\left(\frac{a}{W}\right)^{1/2}\left(1.4+\frac{a}{W}\right)\left[3.97-10.88(\frac{a}{W})+26.25(\frac{a}{W})^2-38.9(\frac{a}{W})^3+30.15(\frac{a}{W})^4-9.27(\frac{a}{W})^5\right]}{\left(1-\frac{a}{W}\right)^{3/2}} \tag{4.2}$$

for which:
P is the load of the interruption point, N;
B is the specimen thickness, m;
W is the specimen width as shown in figure 4.1, m;
a is the effective crack length determined from the in-situ CT scan images.

To convert fracture toughness K to fracture energy G, the following approach can be used, see equation 4.3.

$$G = \frac{K^2}{E} \tag{4.3}$$

where:
K is the fracture toughness, Pa $m^{1/2}$;
G is the fracture energy, J/m^2;
E is the Young's modulus of the material, N/m^2. For the current NCF material, the E value is 37.9 GPa, [11].
There are in total four layers of 0° plies in each specimen, and the effective crack length is calculated as the average crack length for each pause location in figure 4.4. The benefit of an in-situ CT scan is that only one specimen is needed to obtain many sets of CT images throughout the test duration, as opposed to carrying out multiple individual interrupted tests.

Each in situ CT scan was carried out right after the occurrence of a load drop to determine the crack increment Δa, and hence the effective crack length, a (Δa plus the initial machined notch length, a_0). It is assumed that the effective crack length does not change at the load drop, which is in accordance with [14] which implied that the load drops corresponded to the sudden fracture of the $\pm 45°$ plies rather than extension of the crack in the 0° plies. The failure load P used for each fracture toughness calculation is the value at the load drop.

The fracture energy of the specimen at each pause location is determined and thus the relationship between fracture energy and crack increment can be established. In figure 4.4 it can be seen that the pause locations are spread across the whole displacement range, however, meaningful information can only be extracted from a very limited displacement range after the initial crack extends and before the ultimate failure. As no effective crack propagation takes place during the linear loading phase nor after the major catastrophic load drop caused by compressive failure at the specimen rear end (at 1.3 mm displacement in SP1 and 1.2 mm displacement in SP2 in figure 4.4), only the pause locations which lie between approximately 1 to 1.3 mm displacement are valid for constructing the partial R-curve. Based on these results and assumptions, the partial R-curve could be established, as shown in figure 4.7. It should be noted that the last points (the two points after 4 mm effective crack length) on the R-curves were taken when compressive failure also occurred, so their values might be underestimated/invalid. These points have been included in figure 4.7 for illustration purposes and no quantitative analysis should be carried out in regards to these points. The following findings can be extracted from the graph:

- Fracture energy, G_C, increases with the crack increments.

- A plateau is not reached in the partial R-curve, but there were insufficient measurements prior to compressive failure at the rear end of the specimen.

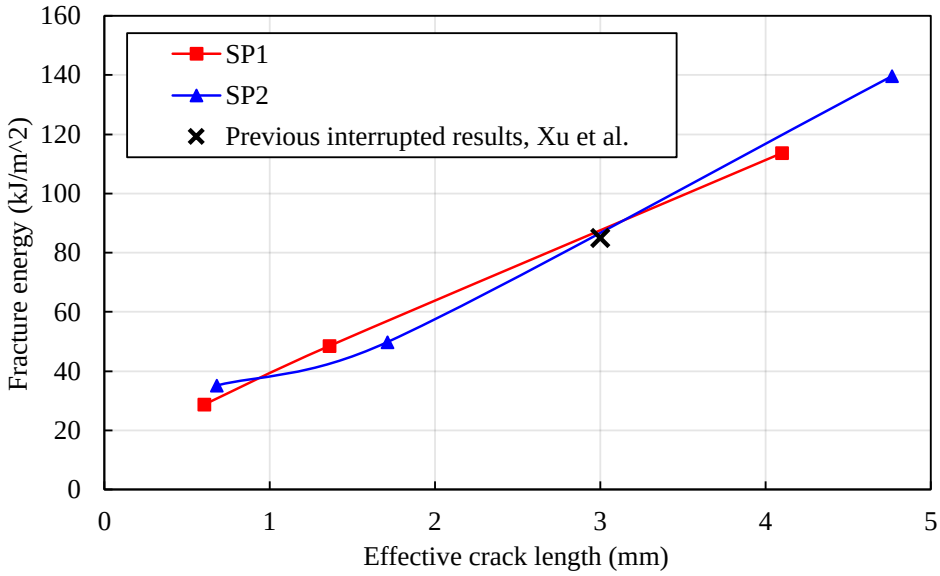

Figure 4.7: NCF ESET specimens' R-curve constructed with in situ CT scans. Previous interrupted results by Xu et al. [11].

It has been demonstrated that an R-curve exists [10] and can be measured by using a robust test method. The ASTM E1922 standard [105] is capable of generating a partial R-curve from in situ CT scans. A previous study carried out by Xu et al. [11] investigated the initial fracture propagation within a full-scale stiffened panel and coupons with the same material and stacking sequence as the current ESET specimens. It was reported that the G_C values of the four configurations carried out were all similar at approximately 3 mm crack length at about 85 kJ/m^2, which is similar to the results obtained by the ESET specimens, shown by the black cross in figure 4.7. Furthermore, the observed R-curve behaviour is also consistent with the previously observed stable fracture propagation after fracture initiation in the full-size stiffened panel reported in [11], which was postulated to be due to the existence of an R-curve [11].

However, the partial R-curves generated with these ESET specimens only provide valid G_c values up to approximately 1.8 mm effective crack length, which is a bit too short. Such a short R-curve is primarily due to the small form factor of the specimen - a constraint faced when using in-situ CT scan. To resolve this issue, it is proposed to carry out another set of tests where a bigger specimen would be used which will enable a longer R-curve to be constructed.

4.3 Compact tension specimen test

The size of the panels that were available to use for this study was not particularly big and it was preferable to have at least eight specimens for interrupted tests. Hence a physically smaller specimen was preferred as it would enable more specimens to be made from one panel. Both the compact tension and the ESET specimens fit the criteria of being small, but as per the discussion

in the previous chapter the ESET specimen geometry suffers the issue of having a short crack length for R-curve characterisation, therefore the compact tension specimen geometry will be used in the second batch of tests.

4.3.1 Compact tension specimen details and test set-up

The NCF panel was approximately 235 mm by 435 mm and eight compact tension specimens could be cut from the panel. The panel size with the specimen layout is shown in figure 4.8, and the compact tension geometry is shown in figure 4.9. The panel has a nominal thickness of 2 mm. The test panel has the exact same material properties, manufacturing method and stacking sequences as the material used in the ESET specimen tests, see section 4.2.1. The specimens' outer shape was cut out using a diamond blade saw cutter, while the notch was milled using a 1 mm diameter drill bit. A previous study [131] by Camanho et al. investigated the notch tip radius effect on fracture toughness of QI laminates showed a 1 mm diameter notch tip radius does not affect the results compared with a smaller tip radius. The loading holes were cut out using a hole saw of the correct diameter. The NCF compact tension specimen tests were carried

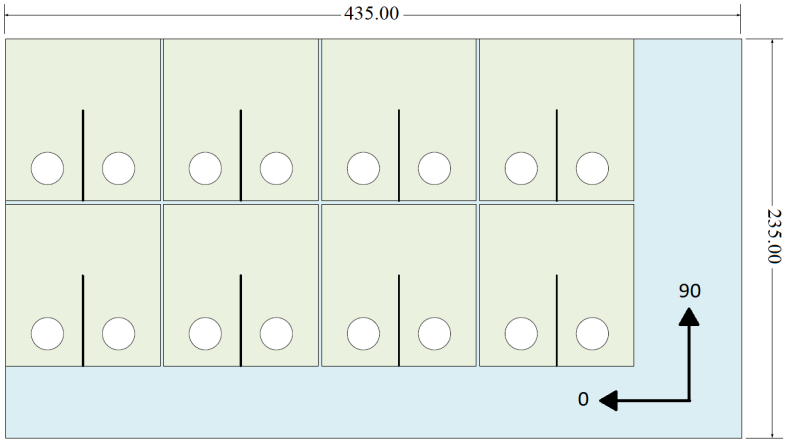

Figure 4.8: Panel geometry and specimen layout for the NCF compact tension specimens, all dimensions in mm.

out in a 100 kN universal hydraulic test machine from Instron. The specimens were loaded via two loading pins inserted into the top and bottom loading holes. The loading pins were secured to two rectangular metal rods which were clamped by the test machine cross-head. Specimens were loaded under displacement control with a loading rate of 1 mm per minute. Given the specimen was relatively thin, an initial test was carried out where the specimen was gently loaded to check if buckling would be an issue - and indeed the specimen showed a tendency to buckle at the rear, see figure 4.10. To eliminate the buckling, an anti-buckling jig was developed which consists of four aluminium plates. Two plates were lightly clamped to each side of the specimen providing constraint in the thickness direction to eliminate buckling. Figure 4.11 and 4.12 show the specimen set-up, including the loading jigs and the anti-buckling plates. The specimen itself is

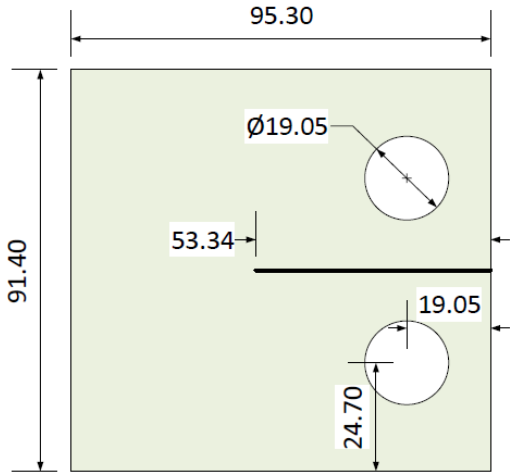

Figure 4.9: NCF compact tension specimen geometry, all dimensions in mm.

marked by the arrow. Since the anti-buckling plates were clamped in place via the two aluminium rods which were hand-tightened with nuts and bolts, hence minimal friction that could affect the results was introduced.

Figure 4.10: Initial NCF compact tension test showing buckling at the rear of the specimen.

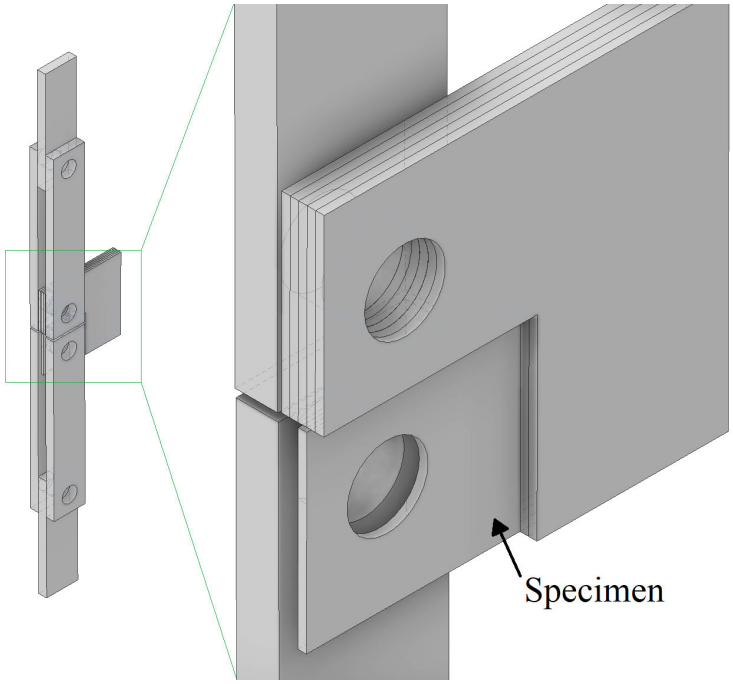

Figure 4.11: NCF compact tension specimen test set-up schematic with anti-buckling plates, the front loading rods have been hidden in the close-up shot. The anti-buckling plates were made from aluminium and the loading-rods were made of steel.

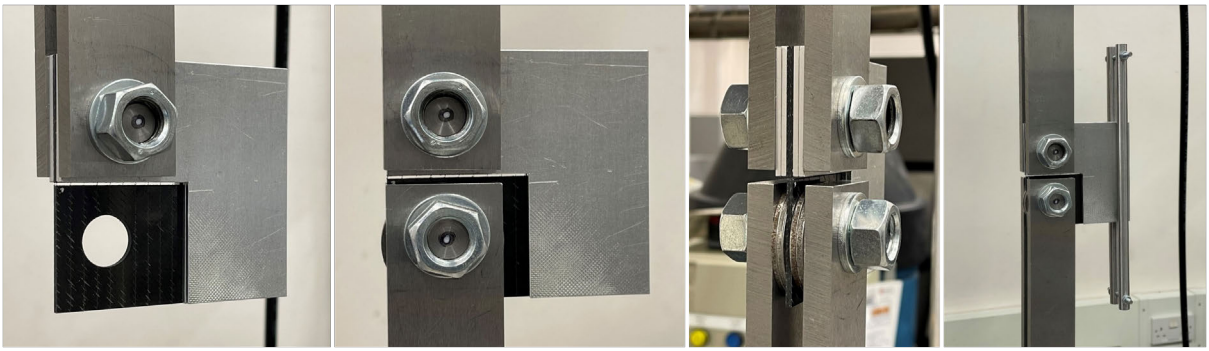

Figure 4.12: NCF compact tension test setup and anti-buckling jig.

4.3.2 Compact tension specimen test results

A total of seven tests were carried out with the NCF compact tension specimens - specimens 1 to 7 (SP1 to SP7). SP1 was the initial specimen used to carry out the buckling verification test hence it was not used for further tests. Two uninterrupted tests were carried out - SP2 and SP3. The load-displacement curves of SP2 and SP3 are shown in figure 4.13. A high degree of resemblance can be found between the two tests, where they have an almost identical peak load, stiffness, and even the magnitude of the first load drop. Both uninterrupted specimens yielded a peak load of around 3.7 kN at about 1.7 mm displacement. Followed by a load-drop of magnitude 1 kN.

The load was maintained at around 2.5 kN for a brief period then substantial load drops started occurring in both tests at 2.3 mm displacement. For SP2, the load decreased to as low as 0.7 kN and the test was stopped manually when compressive failure was observed at the rear of the specimen. On the other hand, for SP3, the test was stopped at the same displacement value as SP2, but no compressive failure was observed at the rear of the specimen. Figure 4.14 shows the pictures of the damaged uninterrupted specimens. With the anti-buckling jig installed, no buckling was observed in either of the uninterrupted tests, this could be further backed up by the fact that there is no non-linearity seen in the load-displacement curves - which is typically seen in samples experiencing buckling/bending.

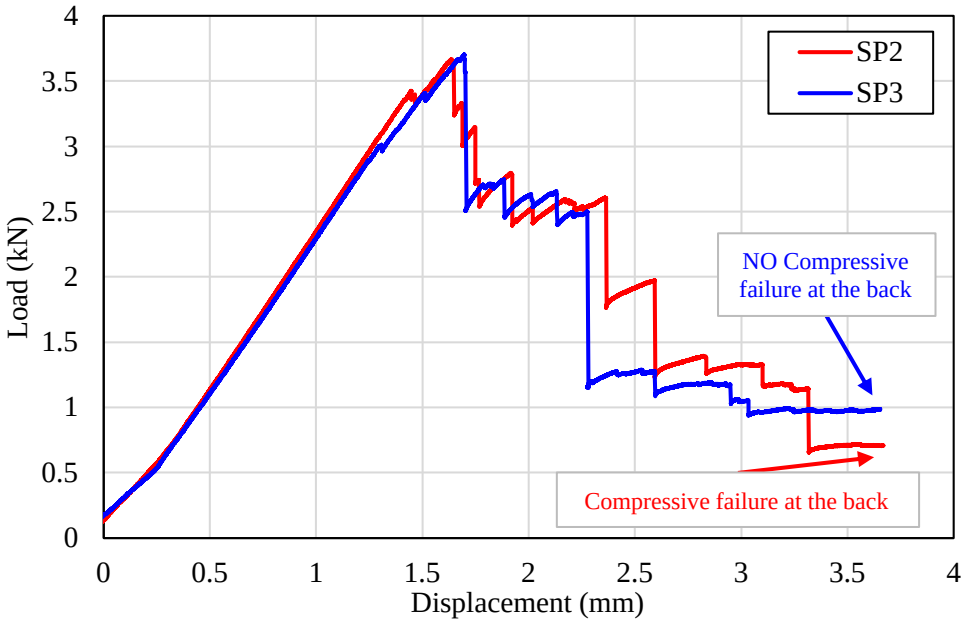

Figure 4.13: Load-displacement curves of uninterrupted NCF compact tension specimens.

Figure 4.14: Surface damage of SP2 and SP3, compressive failure at the rear for SP2 vs no compressive damage for SP3.

With the two uninterrupted tests established, four more interrupted tests were carried out - SP4, 5, 6, and 7. Three of these were successful as SP6 was damaged during testing and results are disregarded. The load-displacement curves of the three successful interrupted tests are shown in figure 4.15, with the crosses indicating the location of interruption. SP4 was stopped just before the major load drop took place in the failed specimens at round 1.5 mm displacement, which should give a good indication of the damage status prior to the major load drop. SP5 was the next in line, where it was stopped right after the first major load-drop took place at around 1.6 mm displacement. The magnitude of the load drop was substantial, hence SP5 should provide a good insight into the situation after some crack propagation. SP7 had a little difference compared to other specimens where the first load drop took place slightly later than the others and was of a smaller magnitude, but other characteristics were in line with the other specimens. SP7 was stopped after the second wave of major load drop at approximately 2.5 mm displacement, which would represent the situation where substantial crack propagation has taken place. There is a blue cross at the load-displacement curve for SP3 also - although SP3 was not meant to be an interrupted test but no compressive failure took place at the end, hence it could be argued that SP3 is a valid sample to be analysed as an interrupted specimen. The addition of SP3 would be greatly beneficial for the forthcoming CT scan and data analysis since it is at a very late stage of the loading process.

To summarise, a total of five tests were carried out with valid results. One of which failed in compression at the rear and was used as a guidance for the remaining four interrupted tests. The four interrupted tests were very successful in that they cover a wide displacement range which should provide an insight to the damage process.

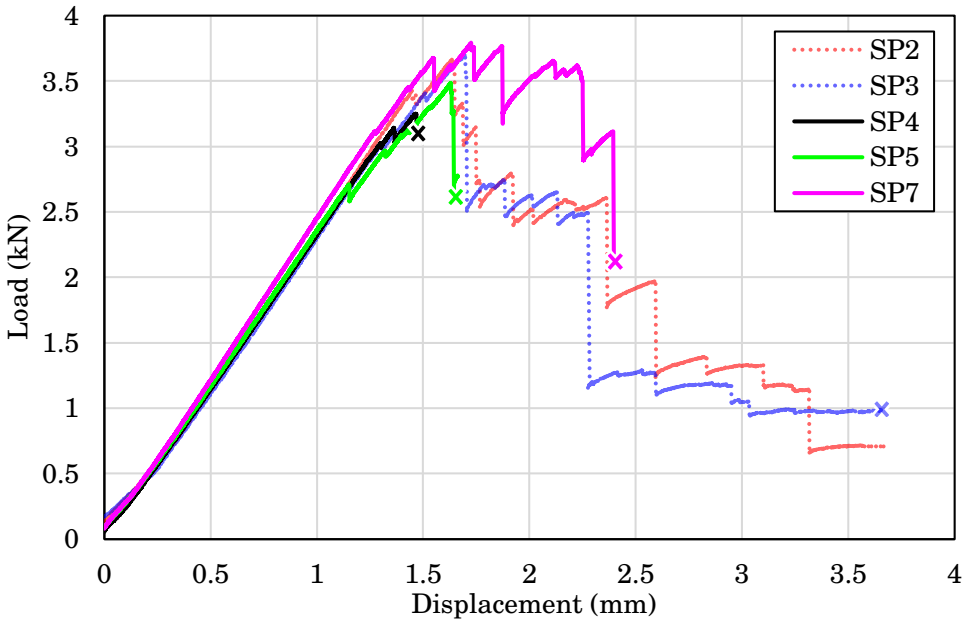

Figure 4.15: Load-displacement curves of interrupted NCF compact tension specimens.

4.3.3 Compact tension specimen analysis

The four interrupted test specimens - SP3, 4, 5, and 7 were sent for CT scanning to investigate the damage status through the testing process. The interrupted specimens were soaked in zinc oxide solution overnight to ensure a better image quality for CT scanning. With the help of the zinc oxide, the image contrast is increased substantially and can ensure even small cracks are visible in the CT scan images. Figure 4.16 shows the CT scan images of the four interrupted specimens. These images are taken from the 0° ply closest to the mid-plane of the specimen.

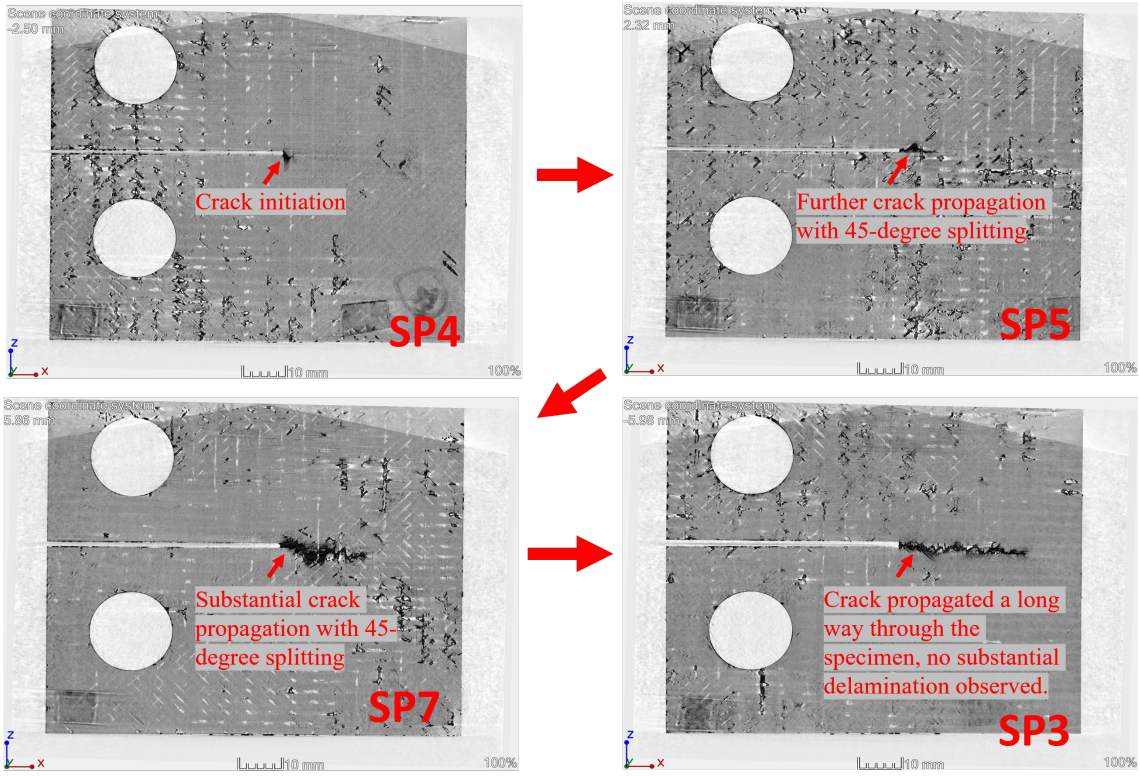

Figure 4.16: CT scan images of the four interrupted NCF compact tension specimens, images taken from the 0° ply closet to the mid-plane. The CT scanner used was a Nikon XTH 225ST CT scanner. The voltage used was 102 kV and the electric current used was 208 A. The number of projections per scan was 2000 and the exposure time was 500 ms. The angle swept was 360°. The voxel size was 19 m.

The red arrows in figure 4.16 indicates the sequence of damage throughout the test process, with SP4 being the earliest at 1.5 mm displacement and SP3 being the latest at 3.7 mm displacement. Although SP4 was stopped at 1.5 mm displacement just before the first major load drop, there is still signs of 0° damage shown in the CT scan images. Such damage may have induced the minor load drops seen prior to the test was stopped. Moving on to SP5, it is apparent that the crack length has increased significantly, which can be attributed to the first major load-drop at 1.6 mm displacement. There is no signs of delamination either at this stage. Turning to SP7, where it was stopped at a much later stage through the test process, at 2.4 mm displacement - a series of load drops have occurred prior to this point and the load has dropped to approximately 60% of the peak value. As expected, the crack has propagated by a significant length at this stage to about half of the ligament width. There is some signs of splitting in the CT scan image of SP7 but nothing major. And lastly for SP3, it was the specimen which almost reached its strain limit but did not undergo compressive failure at the rear. The crack has propagated further again to about 75% of the ligament width - an overall very clean crack with no signs of delamination.

It should be noted that the mismatch of the stitching orientation in figure 4.16 due to a

slight warping of the specimen, therefore the imaging plane can not be perfectly parallel to the specimen thickness. Hence each photo is slicing through more than one layer at different parts of the specimen - causing the mismatch in stitching orientation. Care was taken to make sure the images were at the 0-degree plane for the crack tip location.

With the CT scan images of the interrupted specimens established, an accurate relationship between the crack length and load can be deduced. The crack length was measured with the same method as the ESET specimens - using the CT scan data analysis software VG Studios Max by VOLUME GRAPHICS to digitally measure the crack length. The crack length concerned in this study is the effective crack length - deduced by averaging the crack length of all of the 0° plies through the thickness. The benefit of using the effective crack length is that it takes the fracture process zone into consideration.

Table 4.1 shows the numerical values of the effective crack length for each of the interrupted specimen. Figure 4.17 plots the effective crack length and load as a function of displacement for the interrupted samples - the rate of increase of the crack length decreases as the displacement value increases.

Table 4.1: Effective crack length of the interrupted specimens measured digitally using the CT scan images. Effective crack length is the average of all the 0° ply crack length. The c.v. value represents the variation of the measured crack length from the 0° plies.

Specimen number	Effective crack length (mm)	Load (kN)	Displacement (mm)	c.v.
SP4	2.65	3.13	1.47	11.8%
SP5	8.25	2.78	1.65	11.7%
SP7	19.55	2.15	2.40	6.8%
SP3	29.44	0.98	3.63	1.1%

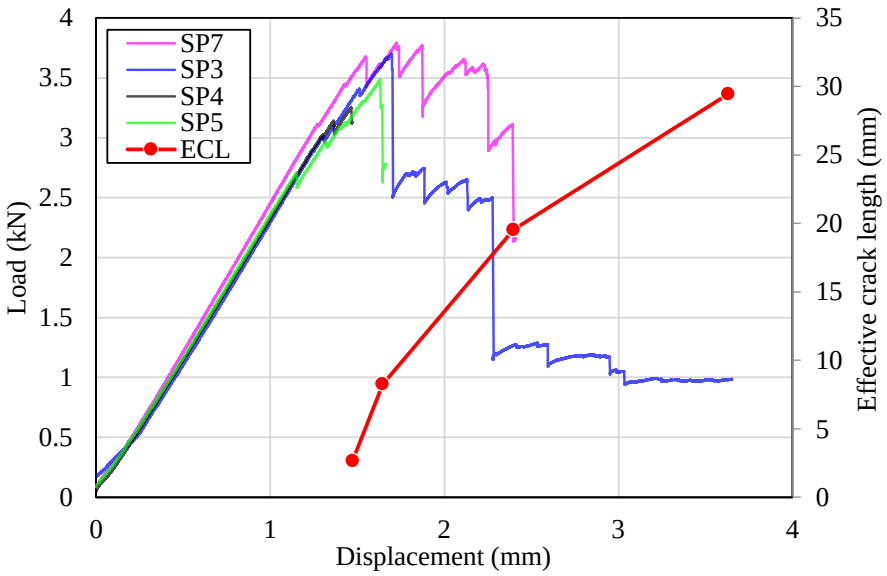

Figure 4.17: Effective crack length (ECL) and load as a function of displacement for the interrupted samples.

With the effective crack length established as a function of load and displacement, the R-curve of the NCF compact tension specimens can be constructed. The geometries of the NCF compact tension specimens are in accordance with the requirements of ASTM E399 [12] standard. The standard provides a data reduction method for calculating the fracture thoroughness value K -

$$K = \frac{P}{B\sqrt{W}} f(\frac{a}{W}) \tag{4.4}$$

where:

$$f\left(\frac{a}{W}\right) = \frac{\left(2+\frac{a}{W}\right)\left[0.886+4.64(\frac{a}{W})-13.32(\frac{a}{W})^2+14.72(\frac{a}{W})^3-5.6(\frac{a}{W})^4\right]}{\left(1-\frac{a}{W}\right)^{3/2}} \tag{4.5}$$

for which:

P is the load of the interruption point, N;

B is the specimen thickness, m;

W is the specimen width (from the centre of the loading hole to the edge away from the notch) as shown in figure 4.9, m;

a is the effective crack length as determined in table 4.1.

With the specimen geometries data in figure 4.9 and the data in table 4.1, a fracture toughness value K can be computed for each interrupted sample. The fracture toughness value K can be easily converted to fracture energy G using the equation presented in the previous section, see equation 4.3

In addition, for the calculated fracture toughness values to be considered valid, the following criterion needs to be met [132]:

$$(W - a) \geq 2.5(K/\sigma_y)^2 \tag{4.6}$$

where:
K is the fracture toughness calculated in equation 6.2, Pa/m$^{1/2}$;
W is the specimen width, see equation 6.2, m;
σ_y is the yield stress of the material, Pa.

This criterion ensures that $(W - a)$ is sufficient to avoid the fracture process zone extending beyond the boundary of material. With the help of the above four equations (equation 4.3 to 4.6), the R-curve of the NCF compact tension specimens can be calculated, shown in figure 4.18.

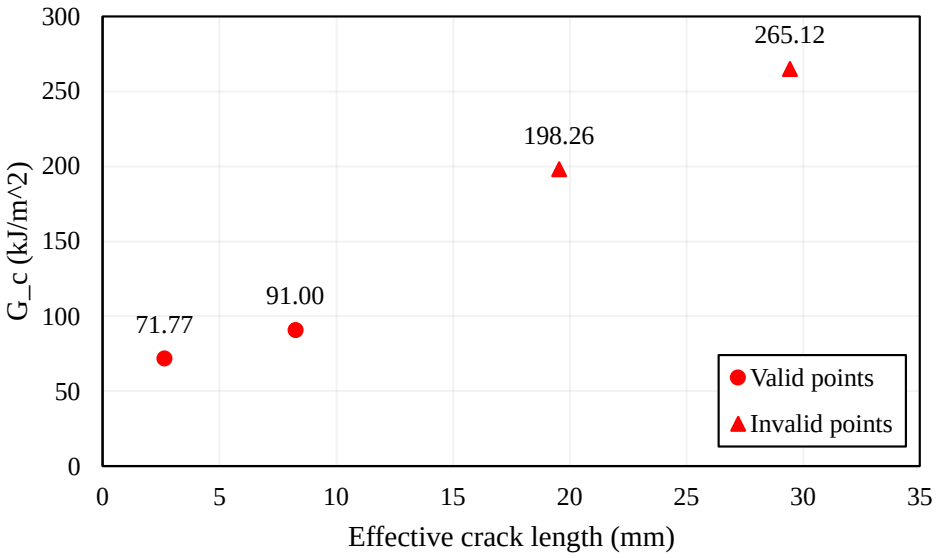

Figure 4.18: R-curve of the interrupted NCF compact tension specimen, calculated with the ASTM E399 data reduction method.

The critical strain energy release rate G_c is showing an overall increasing relationship with effective crack length/crack increment. According to the ASTM criterion [132], only the first two interrupted specimens (SP4 & SP5) are yielding valid results in relation to the crack-ligament ratio. As the latter two interrupted points are out of the validity range, no conclusions can be drawn from this set of tests regarding the plateau of the R-curve. Since the material used in the compact tension tests are custom therefore no published information regarding fracture toughness can be found for it.

4.4 Comparison and discussion

Two sets of tests were carried out to determine the R-curve of the proprietary JAXA NCF material. Figure 4.19 shows a comparison of the R-curves obtained from the two sets of specimens. The last points of the ESET specimen R-curves were invalid as the interruption took place after compressive failure took place at the rear of the specimen. The latter two points on the compact tension specimen R-curve are deemed invalid as they fail to meet the criteria that ASTM suggests [132]. Neither of the two sets of tests yielded R-curves long enough to determine the location/presence of the plateau. All three R-curves in figure 4.19 are showing an increasing trend in the valid region. The two R-curves from the in situ ESET specimens are showing high resemblance to each other - a sign of consistency. The last valid points of the ESET R-curves are at approximately 1.7 mm crack increment with a G_c value of 50 kJ/m^2. Turning to the compact tension specimen R-curve, the last valid point was at 8.3 mm crack increment with a G_c value of 91 kJ/m^2. Although the compact tension specimen test R-curve is longer than that of the ESET, still no conclusions can be drawn regarding the location of the plateau though.

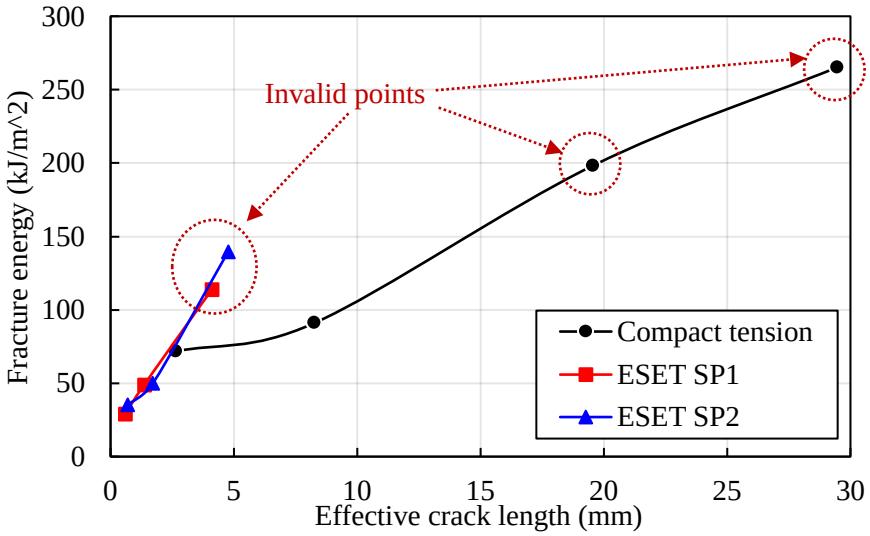

Figure 4.19: R-curves obtained from interrupted compact tension specimens and in situ ESET specimens.

4.5 Conclusions

Two sets of experimental tests using the JAXA NCF material were presented in this chapter. One set consists of testing a number of compact tension specimens, while the other set consists of two ESET specimens with in-situ CT scan. From the compact tension specimens set, one uninterrupted test and four interrupted tests were carried out. The interrupted test specimens were prepared and subsequently CT scanned. Test results and CT scan images suggest a positive correlation between crack length and displacement, and the rate of increase of crack length slows

down as displacement increases. No obvious delamination was found in the CT scan images of the interrupted compact tension specimens. R-curves for the compact tension specimens were calculated using the ASTM E399 data reduction method, only the first two points on the R-curve were in the valid range, reaching 91 kJ/m^2. For the ESET specimens, two tests were carried out with in-situ CT scan. In-situ CT scan enables each specimen to produce a R-curve on its own, hence two R-curves were produced for the ESET specimens. Data shows a linear increase in the R-curve of the ESET specimens with no evidence of plateau yet, the maximum valid value of fracture energy was 48.5 kJ/m^2.

While these two sets of tests provided an insight to the damage morphology and their corresponding R-curves, it could be argued the R-curves obtained here were still not long enough and there is still no evidence of the location of the plateau. Therefore it is proposed to conduct another set of tests where hopefully the R-curve plateau can be seen, details of which are given in chapter 5.

CHAPTER 5

THIN-PLY MATERIAL FRACTURE BEHAVIOUR

5.1 Background

The previous chapter experimentally investigated the translaminar fracture behaviour of JAXA NCF materials with compact tension specimens and ESET specimens. Test results suggest an increasing fracture energy as a function of effective crack length. These results are of paramount value to the ultimate goal of the PhD project - to develop a cost-effective modelling method for predicting translaminar fracture in large stiffened panels. However, the R-curves obtained from the previous chapter were still too short to view/determine the location of the R-curve plateau. It could be argued that the short R-curve was due to the specimen geometry being relatively small. Such finding was reported by Xu et al. in ref [13] also. The data from a larger coupon and thereby a longer R-curve would be beneficial for modelling of the full-scale stiffened panel from JAXA as it is large in size and would likely yield a long crack length.

Increasing the size of the specimen is one way of obtaining a longer crack growth, but there is a limit to how large the specimen can get until other factors start to interfere - test machine size limit, undesired failure modes such as buckling, and cost, to name a few. While a larger specimen would help, a reduced damage height may also contribute to a longer R-curve [14]. By manufacturing specimens from plies with thinner thicknesses, the damage zone and hence fracture toughness ought to decrease as they are approximately proportional to ply thickness [85, 133]. The reduced fracture toughness from thinner plies would cause crack propagation to begin at a lower load level and hence the potential to capture a longer R-curve.

This chapter presents the experimental characterisation of the R-curve for specimens made from thin-ply prepregs. The rationale behind this test is to reduce the crack initiation load by reducing ply thickness and thereby obtaining a longer R-curve - providing support for the large

stiffened panel modelling.

5.2 Specimen details and test set-up

Six compact tension specimens were manufactured using the Skyflex UIN020 carbon fibre/epoxy consisting of Mitsubishi Rayon MR40 carbon fibre and SK chemical K51 resin, with a nominal ply thickness of approximately 0.03 mm (0.024 mm measured). This thin-ply pre-preg material from Skyflex is a different material from the IM7/8852 pre-preg or the NCF materials used in the previous chapters, but the fibres have similar properties to the IM7/8552 pre-pregs. The compact tension geometry was chosen for this set of tests for the following reasons -

- The compact tension geometry enables stable crack growth, a must for R-curve characterisation.

- The square shape of compact tension specimens provides a good crack-length to specimen area ratio - less material needed means lower cost. The Over-height Compact Tension specimens used previously had the capability of avoiding buckling at the top and bottom of the specimen, but for the thin-ply specimens this property is unnecessary as the load level is lower which means buckling would not be an issue.

- The compact tension geometry is widely used for fracture toughness characterisation - even has an ASTM E399 standard [12] for it.

To obtain a long R-curve, the dimensions of the compact tension specimens shall be as large as possible. With other physical limitations considered (including available materials, test machine height etc.), the largest possible dimension of the compact tension thin-ply specimens is shown in figure 5.1. The in-plane dimensions of the thin-ply compact tension specimens were double that of the NCF compact tension specimens detailed in chapter 4.3.

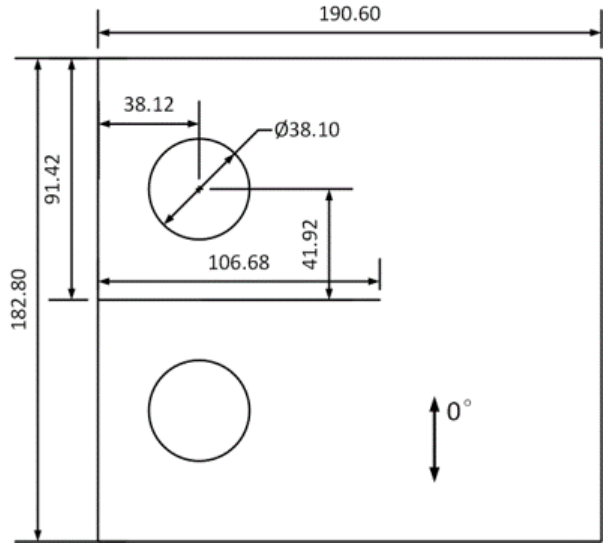

Figure 5.1: Schematic of the thin-ply compact tension specimens, dimensions in mm.

The thin-ply compact tension specimen has 128 plies with a stacking sequence of $[45/90/-45/0]_{16s}$. The same stacking sequence from the NCF compact tension specimen was employed here but with four times the number of plies. All six of the samples were cut from one panel using a diamond edge saw for the outer edges and a 1 mm endmill for the crack. The loading holes were drilled using the correct-sized hole saw. The thin-ply panel was hand layup and cured according to the manufacturer's specifications (heating up rate 3°C/min, dwelling at 80 °C for 30 mins and holding at 125 °C for 90 mins). Figure 5.2 shows all six thin-ply samples in a ready-to-test state.

Figure 5.2: Pictures of the six thin-ply compact tension specimens in a ready-to-test state.

The specimen was loaded at the loading holes by inserting two loading pins, the loading pins were secured in place via two metal rods - one for the top and one for the bottom. These two metal rods were then clamped by the test machine cross-heads. Tests were carried out in a 100 kN Instron hydraulic-driven universal test machine displacement controlled at a rate of 2 mm per

minute. Figure 5.3 shows a picture of the specimen in the test machine. Load and displacement readings from the test machine were recorded. An additional video gauge was used to optically track the pin-opening-displacement. A trial test was carried out to assess if buckling would be an issue. Results indicated no obvious buckling occurred during the trial test and therefore no anti-buckling jigs would be necessary.

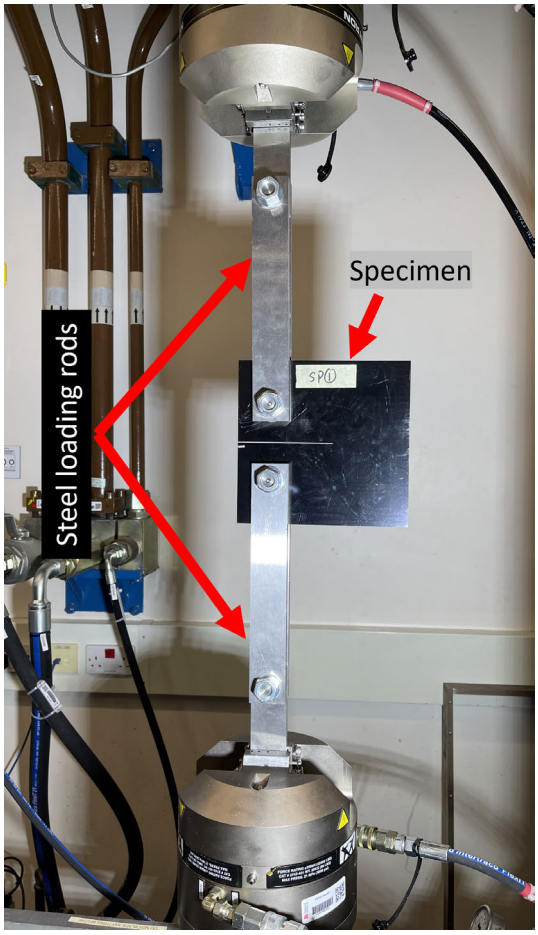

Figure 5.3: Picture of the thin-ply compact tension specimen loaded in the test machine.

5.3 Test results

A total of five thin-ply compact tension specimens were tested. Specimen No.1 (SP1) was the test-to-failure case which serves as a guide for the remaining tests. SP2, 3, and 4 were three interrupted tests. SP5 was a test-to-failure case also, but with the machined notch sharpened with a razor blade, as opposed to the other specimens where the machined notch tip has a 0.5 mm tip radius from the drill bit. Displacement readings obtained from the test machine cross-head were compared against pin-opening-displacement (POD) readings from the video gauge, no meaningful differences were observed - indicating that the compliance of the loading

jig is minimal for this set of tests. For the remainder of this chapter, no distinction will be made between test machine cross-head displacement and POD. Figure 5.4 shows the load-displacement curves for the test-to-failure specimen - SP1. Load increased linearly during the loading phase and peaked at approximately 5.2 kN at 1.3 mm displacement. The linearly increasing load was terminated by the biggest single load drop of about 2 kN, which is approximately 40% of the peak load. The peak load-drop was followed by multiple load-drops of much smaller magnitude, each bringing the load to a lower level. The load decreased in a stable manner to about 1 kN at almost 3 mm displacement. No compressive failure took place at the rear of the specimen even at a high displacement value. No obvious buckling was observed throughout the duration of the test. Figure 5.5 shows the surface damage morphology of SP1. A very neat and straight fracture path can be seen with minimal signs of delamination or damage process zone, no surface delamination was observed.

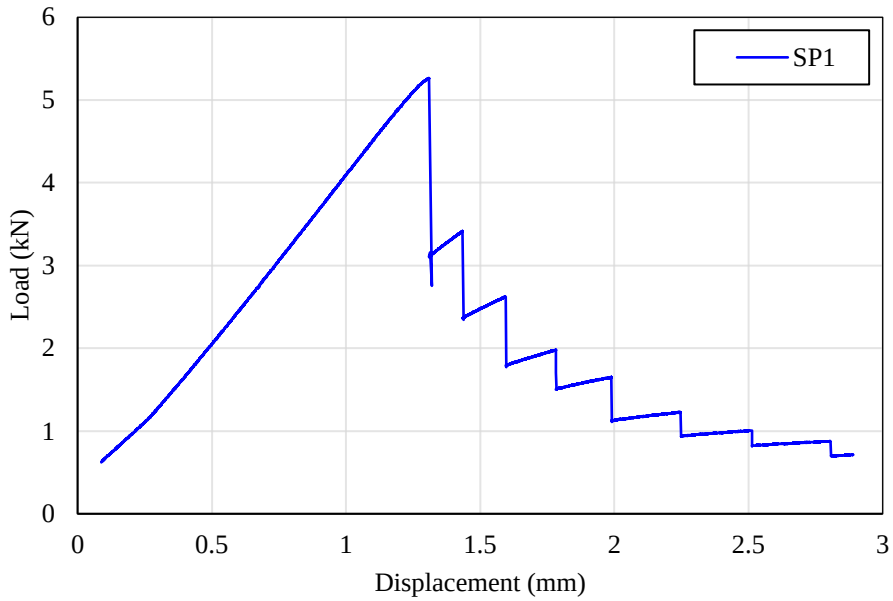

Figure 5.4: Load-displacement curve of the test-to-failure specimen - SP1.

Figure 5.5: Surface damage morphology of the test-to-failure specimen - SP1. Picture showing a straight and neat crack with minimal signs of delamination or damage process zone.

Following the test-to-failure case, three interrupted tests were carried out - SP2, 3, and 4. The three interruption points were spread across a wide displacement range which should give a good insight into the damage progression. Figure 5.6 shows the load-displacement curves of the three interrupted tests. The interrupted locations for each test are marked by a cross coloured correspondingly. The first interrupted test - SP2, was stopped just after the first major/peak load drop. A linear load-increasing trend was seen prior to the load drop at approximately 5 kN and 1.3 mm displacement. The load drop was of a similar magnitude to all other specimens - about 2 kN, and the test (SP2) was interrupted straight after the major load-drop occurred. This should provide a good indication of the length of the initial crack propagation. The second interrupted test - SP3, was stopped after the second load drop took place, marked in green. The second load drop was of 1 kN in magnitude, which saw the load drop from 3.3 kN to 2.3 kN at 1.5 mm displacement. This test should give a good indication of the crack propagation prior to the second load drop. The third interrupted test - SP4, was stopped at about 60% of the displacement range or after four load drops. At this point, the load has decreased dramatically to about 1.4 kN - approx. 30% of the peak load. SP4 ought to provide an insight into the damage situation at a late stage of the loading process. The load-displacement curves shown in figures 5.4 and 5.6 have been shifted in the x-axis such that the linear portion of the load-increase pass through the origin.

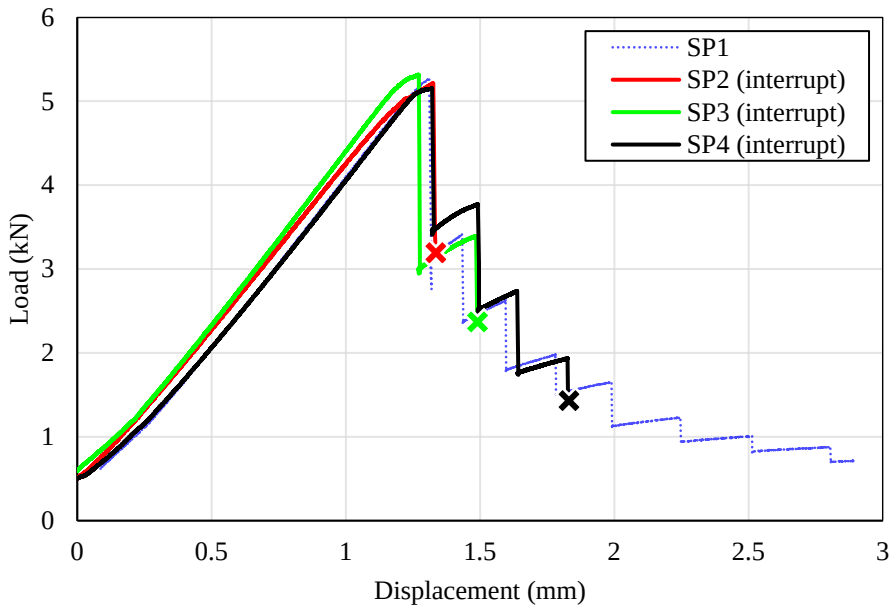

Figure 5.6: Load-displacement curves of thin-ply compact tension interrupted cases (SP2, 3, 4) and the test-to-failure case (SP1).

In addition to the first four cases mentioned previously, an extra test-to-failure case (SP5) was carried out where the notch was sharpened by tapping a razor blade into it. This would give the initial crack a sharper pre-crack, as opposed to the machined notch which has a radius of 0.5 mm. The rationale of this test will be explained in the following section. Figure 5.7 shows a picture of the sharp crack and figure 5.8 shows the load-displacement curve of the specimen with the sharp notch (SP5) compared to the specimen with a machined notch (SP1). The general trend between the load-displacement curves of the machined notch specimen and the sharp notch specimen is very similar - especially during the load-decreasing phase after about 1.3 mm displacement. A lower peak load was found in the sharp-notched specimen - 5.2 kN for the machined notch and 4.8 kN for the sharp notch. The magnitude of the first load drop was significantly smaller (approximately 56%) for the sharp-notched specimen compared to the machined notch specimen .

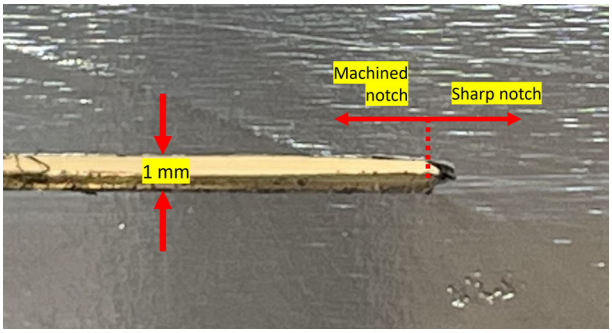

Figure 5.7: Picture of the sharp notch of SP5, produced by tapping a razor blade into the machined notch. Horizontal arrows in the figure are for illustration of the directions only and are not indicating the length.

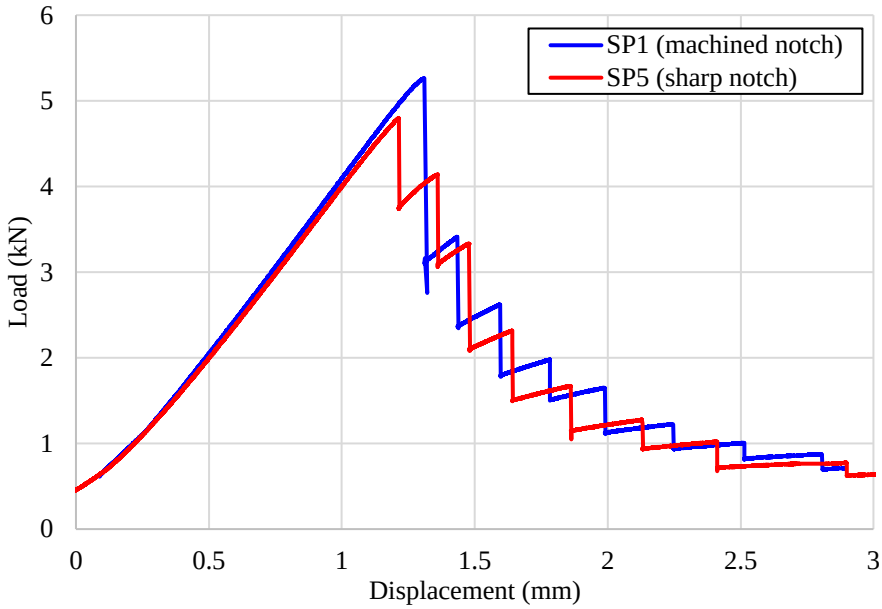

Figure 5.8: Load-displacement curves of thin-ply compact tension specimen with sharp notch compared to machined notch.

5.4 Results analysis with CT scan images

Judging by the clean fracture surface from all of the specimens, it is proposed that there is minimal delamination/splitting within the specimen, and hence the effective crack length ought to be the same as, or very similar to, the crack length measured from the surface. To check the validity of this hypothesis, SP1 was sent for CT scanning. Figure 5.9 shows a typical image of the internal damage morphology of SP1. The picture was taken at the mid-plane of the specimen, showing no visible signs of delamination or internal splitting. The damage morphology at other ply interfaces throughout the entire thickness was identical to that of the mid-plane (i.e. no signs of delamination or splitting in other plies). The same approach for measuring the effective

crack length (by averaging the crack length of all of the 0° plies) from chapter 4 was employed to measure the effect crack length of SP1, and results reveal the same measurement as the surface crack length, as indicated in figure 5.10. This indicates the surface crack length should be representative of the effective crack length and therefore for the thin-ply compact tension tests only, the surface crack length will be treated the same as the effective crack length.

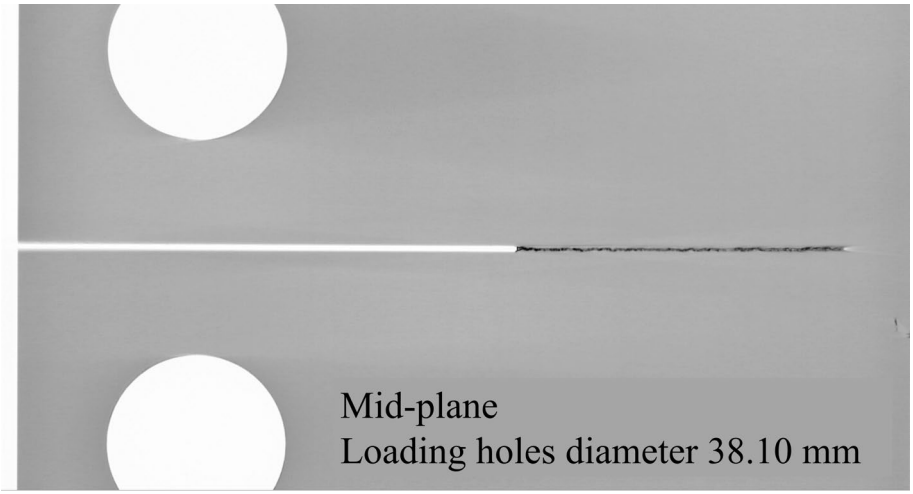

Figure 5.9: CT scan image of the machined-notch test-to-failure specimen, SP1, showing a clean and neat fracture path with no signs of delamination or splitting. The CT scanner used was a Nikon XTH 225ST CT scanner. The voltage used was 102 kV and the electric current used was 208 μA. The number of projections per scan was 2000 and the exposure time was 500 ms. The angle swept was 360°. The voxel size was 19 μm.

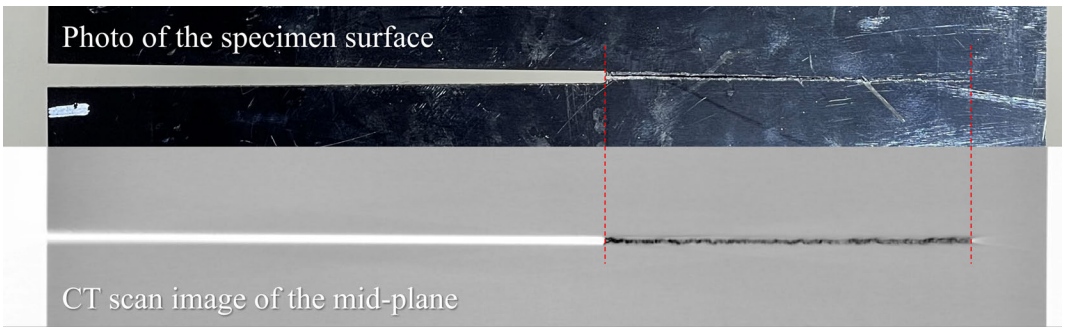

Figure 5.10: Crack length comparison between a photo of the specimen surface and CT scan image of the specimen mid-plane. (Photos at the same scale, surface specimen photo taken when specimen was still under load hence the slightly opened notch compared to the CT scan image)

During the thin-ply compact tension testing, a video gauge was employed to measure the POD and to record a video of the test. With the help of the video footage, the surface crack length can be measured optically throughout the test duration. Taking the peak/first load-drop at 1.3 mm displacement in figure 5.4 as an example - the crack increment at the first load drop would be 0 mm with a load value taken before the load-drop (5.2 kN). And for the second load-drop, the

crack length would be measured optically at a instance prior to the second load-drop taking place with the load value taken at the peak of the second load-drop (3.4 kN). This would permit a surface/effective crack length to be measured for each load-drop - enabling the calculation of the R-curve with a single specimen. Table 5.1 lists the optically measured surface crack length for each load-drop in SP1. ASTM E399 [12] details a data reduction method for calculating the fracture toughness, K_{IC}, for compact tension specimens - the same approach from chapter 4 (equations 6.2 to 6.3) was used to calculate the R-curve of the NCF compact tension specimens.

Table 5.1: Optically measured surface/effective crack increment as a function of load and displacement, thin-ply compact tension specimen SP1.

Load drop number	Effective crack increment (mm)	Load (kN)	Displacement (mm)
1	0.00	5.26	1.31
2	19.73	3.41	1.43
3	32.00	2.62	1.59
4	41.60	1.98	1.78
5	46.40	1.65	1.99

Figure 5.11 shows the R-curve of the test-to-failure thin-ply compact tension specimen SP1, calculated using the ASTM E399 [12] data reduction method (equations 6.2 to 6.3) with the readings from table 5.1. An increasing trend, albeit with a shallow gradient, in the thin-ply compact tension specimen R-curve can be found, especially for the latter four load-drops between 19 mm surface crack increment to 46 mm surface crack increment. It could be argued that a linear relationship is present in the R-curve between the aforementioned surface crack increment ranges. No obvious plateau was observed in the R-curve obtained. In addition, the first point on the R-curve at 0 mm surface crack increment is displaying a higher G_C value than the second point, against the trend of the remaining points, which is believed to have been caused by the machined notch having a notch tip radius of 0.5 mm. While the 0.5 mm tip radius did not pose an issue for other specimens with thicker plies (e.g. NCF compact tension specimen, IM7/8552 stiffened OCT specimens having a damage process zone size of approximately 3 mm), it has been identified to be attributable to the artificially high initial G_C value found in the thin-ply compact tension R-curve. To reduce the blunting effect of the machined notch tip, it was proposed to test a specimen with a sharp notch by tapping a razor blade into the notch tip - hence Specimen No. 5 (SP5) was carried out.

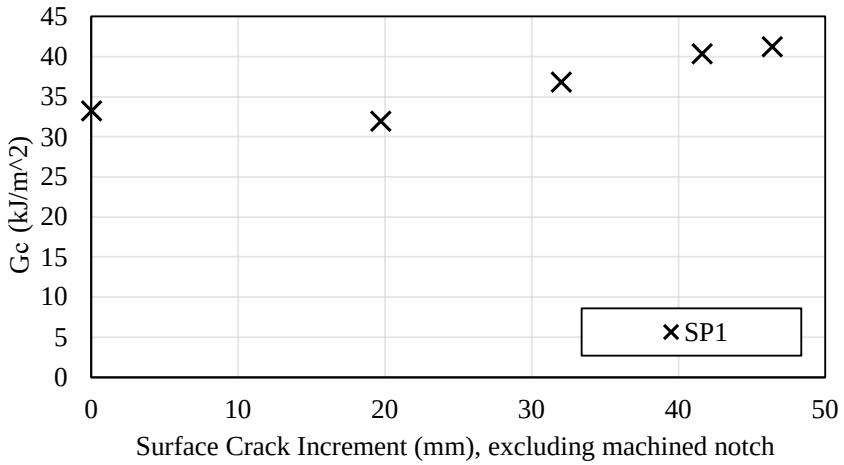

Figure 5.11: R-curve of the thin-ply compact tension specimen SP1, calculated using data reduction method detailed in ASTM E399 [12].

The load-displacement curves of the machined-notch specimen (SP1) and the sharp-notch specimens (SP5) are shown in figure 5.8. As mentioned previously, the two curves are showing very similar trends overall except for the region near the initial/peak load-drop. For the machined notch specimen, a higher peak load was observed with the first load drop of a much greater magnitude than the sharp notched specimen. Whereas for the sharp notched specimen, not only is the peak load at a lower level, the single major/initial load drop seen in the machined notch test was split into two load-drops of approximately half the magnitude. After which the two load-displacement curves show a high degree of resemblance. These results are a very strong indication of the machined notch having an artificial blunting effect on the crack initiation of the thin-ply compact tension specimens. Since the purpose of the sharp notched specimen (SP5) was to assess the notch-tip radius effect on the initial/peak load drop, hence only the first/peak load value from SP5 was used to calculate the G_C value at 0 mm surface crack increment. The remaining points were still from SP1 for consistency.

Figure 5.12 shows the updated R-curve with the addition of the sharp notched specimen's (SP5) crack initiation G_c value. As expected, the lower peak load level seen in the load-displacement curve has resulted in a reduction in the crack initiation fracture energy, shifting it to a lower level than the crack propagation. By replacing the crack initiation fracture energy point from the machined notch by the value from the sharp notch, it could be argued that a linear relationship can be found in the R-curve of the thin-ply compact tension specimen, as indicated by the dashed line in figure 5.12.

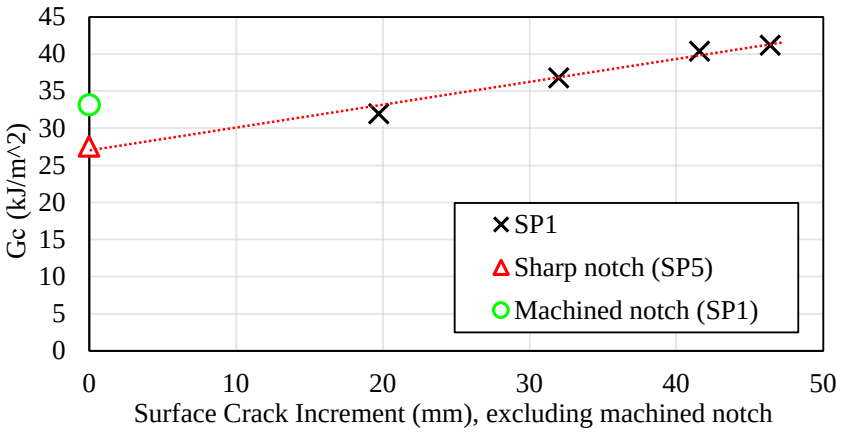

Figure 5.12: Updated R-curve with the addition of sharp-notched crack initiation G_C value.

The ASTM R-curve validity criterion [132] (equation 4.6) also needs to be checked for the R-curve points obtained. For an in-depth explanation of the validity criteria, the reader is referred to chapter 4. The validity check was carried out for all the points on the thin-ply compact tension specimen R-curve (material strength value used for the check was 1012 MPa, derived from QI laminate E = 53.3 GPa and 0° ply strain of 1.9% using the equation $\sigma = \epsilon \times E$, [134]). Unlike the results for the NCF compact tension specimen, where the latter two points both failed the validity check, all of the thin-ply compact tension specimen R-curve points have passed the check despite the two points after 40 mm surface crack increment being very near the rear edge of the specimen. Such a difference is caused by the substantially lower fracture energy values obtained from the thin-ply compact tension specimens. Therefore all of the six points in figure 5.12 are valid.

As for the interrupted specimens (SP2, 3, and 4), since it has been concluded that the surface damage state is representative of the internal damage state and that the surface crack length is the same as the effective crack length measured with CT scan, the remaining interrupted specimens were therefore not sent for CT scanning. However, the interrupted specimens could still provide evidence of the crack propagation throughout the loading process. Figure 5.13 shows a comparison of the surface damage morphology of the three interrupted specimens. As expected, the surface crack increment increases with displacement with no visible delamination or splitting - an overall very clean crack throughout the displacement range. Additionally, the three interrupted tests (SP2, 3, and 4) could also provide three points on the thin-ply specimen R-curve, shown in figure 5.14. The three points obtained from the interrupted tests are showing very similar values to the test-to-failure case SP1 - especially at 0 mm crack increment where SP2 was also a machined notch specimen.

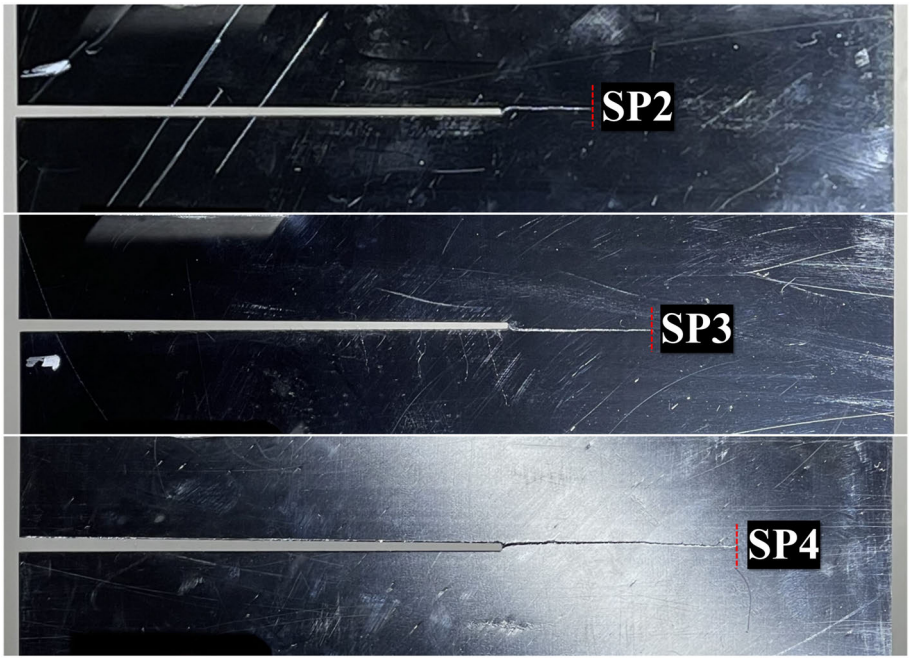

Figure 5.13: A comparison of the surface damage morphology of the three interrupted specimens, SP2, 3, and 4.

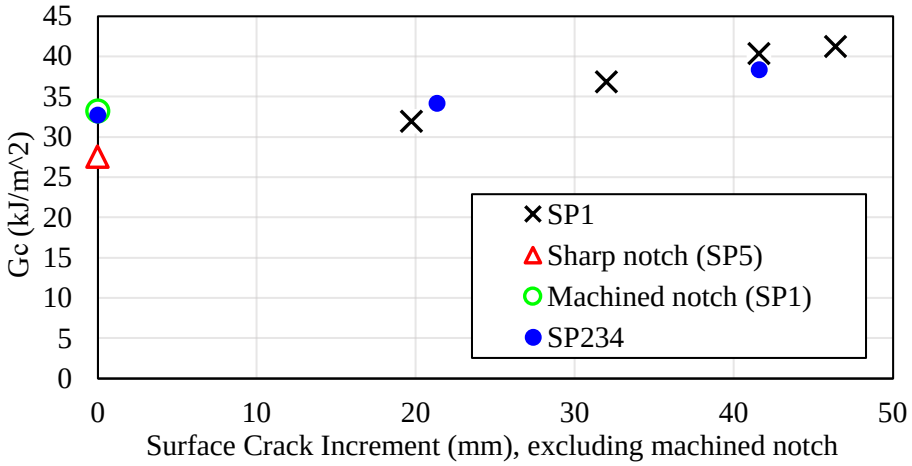

Figure 5.14: Updated R-curve with the addition of points from interrupted specimens - SP2, 3, and 4.

5.5 Discussion

The initial reason for carrying out this set of thin-ply compact tension specimen tests was to obtain a longer R-curve such that the location of the plateau would be revealed which will aid in determining the R-curve for the NCF material. However, due to the nature of the thin-ply material

of having virtually no delamination or splitting, still no obvious plateau can be observed in the R-curve. Up to this point, three sets of tests have been carried out for R-curve characterisation - NCF compact tension, NCF ESET and thin-ply compact tension. This section aims to compare the R-curves obtained from these tests and a conclusion is drawn based on the available evidence.

To compare the R-curves obtained from these three sets of results, some post-processing is needed to eliminate the effect of ply thickness differences. With the NCF material being a different material system from the UD pre-pregs, they will be compared separately. The Skyflex thin-ply material has a nominal ply thickness of 0.03 mm. To take the effect of ply thickness out of the equation when comparing R-curves between different material thicknesses, it is proposed to multiply the thin-ply specimens' G_C value by a factor of 7.5. This figure was derived based on the ply-thickness ratio and the volume fraction (V_f) ratio of the two materials (measured ply thickness ratio $\frac{0.125}{0.0234}$ and estimated V_f ratio $\frac{0.577}{0.41}$ of IM7/8552 to thin-ply). The rationale behind such comparison is based on the assumption that G_c is linearly dependent on ply thickness, and based on the fact that G_c is dependent on the quantity of fibres across the fracture surface, hence ply thickness ratio and V_f need to be taken into account. A previous study by Teixeira et al. [85] concluded that the translaminar fracture toughness and the R-curve is heavily dependent on the thickness of the 0° ply block thickness. Hence for the current study, a thicker ply is functioning as a thicker ply block which needs to be accounted for. Figure 5.15 shows a comparison of the R-curves of the two UD pre-preg specimens, the Skyflex thin-ply results were tested during this PhD project and the IM7/8552 over-height compact tension specimens were tested by Xu et al. [13].

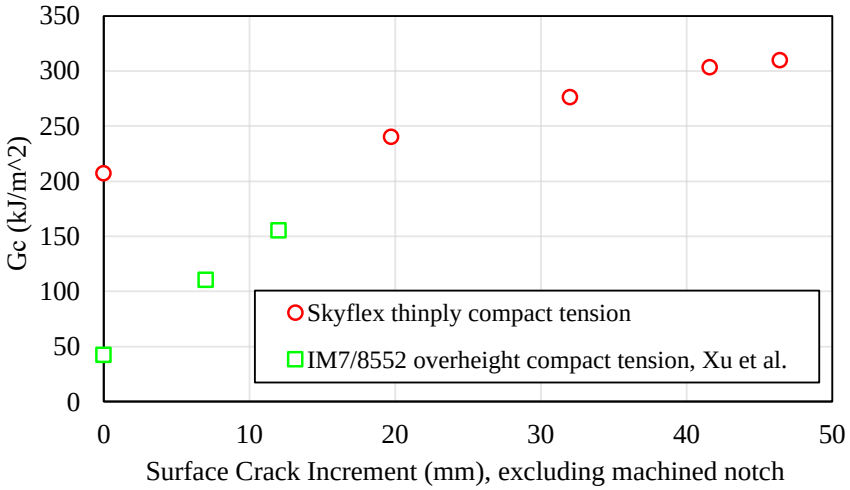

Figure 5.15: R-curve comparison of the UD pre-preg specimens - Skyflex thin-ply compact tension and IM7/8552 over-height compact tension [13]

The R-curves of the UD pre-reg tests are presented in figure 5.15. The sizes of the two specimens vary considerably - with the over-height compact tension specimens (shown in green)

being the smaller one with an initial ligament length of approximately 45 mm, and the Skyflex thin-ply compact tension specimen (shown in red) being the larger one with a ligament length of approximately 84 mm. Therefore the large deviation seen in the crack increment value and G_c value between the two specimens is to be expected given their inherent variation in size. Despite their variations in specimen size, a qualitative conclusion can still be drawn regarding the R-curve.

All the points shown in figure 5.15 are valid points according to the ASTM data reduction method validity check [132]. At least within the validity range, both R-curves are showing a linearly increasing trend with no indication of where the plateau would occur. The Skyflex thin-ply material compact tension specimen is showing higher fracture energy values compared to the IM7/8552 materials (after normalisation against ply-thickness and V_f. Therefore from these two R-curves it is safe to conclude that within the valid range of the ASTM validity check, the R-curve ought to possess a linearly increasing trend. The R-curve trend after the validity range or the location of the plateau can not be determined from these results. To better analyse the material concerned for the ultimate goal of this PhD project, figure 5.16 shows the two R-curves from the JAXA NCF material only.

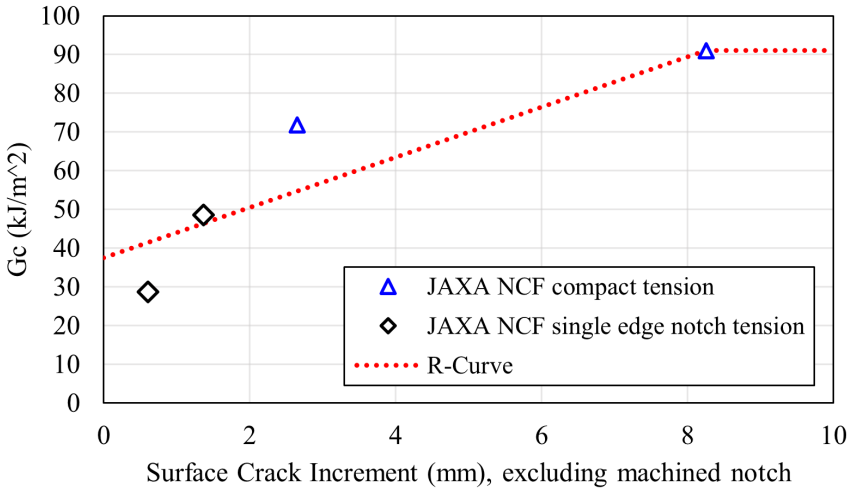

Figure 5.16: R-curves of the two tests using the JAXA NCF material - compact tension tests and single edge notch tension test. The R-curve obtained consists of a linear interpolation of the four valid points. No information about the R-curve after the last known point could be concluded, hence it was assumed that after the last known valid point the R-curve takes a constant value of 91 kJ/m^2.

As stated previously, it is safe to conclude that within the validity range determined by the ASTM criteria [132], a linear R-curve can be established. All four points in figure 5.16 are valid therefore it is safe to assume that a linear R-curve ought to be appropriate for this range. A linear regression line going through the points in figure 5.16 would be a good representation of the R-curve of the NCF material used within those crack increment ranges. No information can be

derived for the R-curve after the last known valid point, therefore an assumption had to be made. As for the R-curve after the last known valid point it was assumed that the R-curve after crack increment 8.1 mm to be constant at 91 kJ/m^2 (the G_C value of the last valid point).

To conclude, the R-curves derived from the four sets of specimens suggest a linearly increasing R-curve within the valid range. For the JAXA NCF material, a linearly increasing R-curve has been established to as far as the crack increment of the last known valid point, after which the R-curve has been assumed to be constant.

5.6 Conclusions

With the aim of obtaining a longer R-curve, this chapter designed and carried out a set of compact tension tests using a thin-ply material. Five of the thin-ply compact tension specimens were tested, all of which showed a very straight and neat crack surface with no signs of delamination and splitting. CT scans were carried out to verify the hypothesis that the surface crack increment is the same as the effective crack increment for this thin-ply specimen, results suggest the hypothesis is true. The effect of notch tip radius was assessed by testing a specimen with the notch tip sharpened by tapping a razor blade as opposed to other specimens where the notch tip has a radius of 0.5 mm. Results suggest the specimen with the sharp notch yield a lower peak load and a smaller magnitude for the initial load drop, with the rest of the load-displacement curve being very similar to specimens with a machined notch tip. The thin-ply compact tension specimen is showing a linearly increasing R-curve to approximately 55 mm crack increment with no sign of the plateau.

A comparison was made between the different R-curves obtained from this chapter and the previous chapter, results suggest all specimens' R-curves are showing a linearly increasing trend within the valid range. For the JAXA NCF material - which is the material of concern for this PhD thesis, a linearly increasing R-curve was concluded before crack increment 8.1 mm, after which the R-curve is assumed to stay constant.

This chapter has aggregated various results both from the current PhD project and from previous literature to form a coherent conclusion regarding the R-curve of the JAXA NCF material. This information obtained in this chapter will greatly help with creating a cost-effective modelling method for predicting fracture in large stiffened composite panels.

CHAPTER 6

NUMERICAL ANALYSIS OF STIFFENED OCT SAMPLES

6.1 Background

Based on the principles of linear elastic fracture mechanics (LEFM), the Virtual Crack Closure Technique (VCCT) criterion is suitable for evaluating crack propagation along a predefined surface. VCCT employs the assumption that the strain energy released when a crack is extended by a certain amount is the same as the energy required to close the crack by the same amount [64]. Consider the 2D example shown in figure 6.1, nodes 2 and 5 will start to release when the available energy release rate G_I is greater or equal to the critical energy release rate G_{IC}.

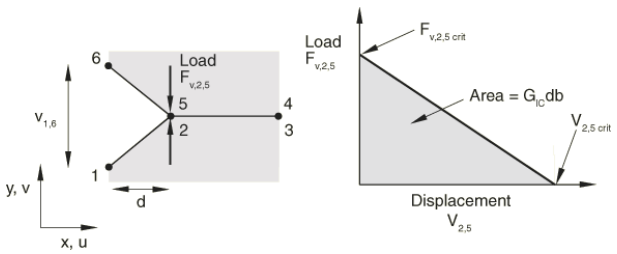

Figure 6.1: Pure Mode I VCCT

Provided our previous assumption is valid, then the available energy release rate G_I could be rewritten as the product of force and distance, which in this example would be

$$G_I = \frac{1}{2} \times F_{v,2,5} \times v_{1,6} \div (bd) \tag{6.1}$$

where, F_v, is the vertical force between two nodes, v is the vertical displacement between two nodes, b is the element thickness and d is the length of the elements at the crack front. Nodes 2 and 5 will start to release when $G_I \geq G_{IC}$.

The ultimate goal of the current PhD project is to develop a cost-effective modelling method for the prediction of translaminar fracture in stiffened composite structures under tension considering R-curves. VCCT-enabled ABAQUS models could analyse the crack propagation behaviour in composite structures, therefore, this chapter details the generation of an ABAQUS model for crack propagation evaluation based on VCCT for small coupons. Once the newly constructed VCCT model proves its capability of predicting fracture behaviour in small coupons, the method will then be implemented to predict the fracture behaviour of a large stiffened panel - achieving the ultimate goal.

The remaining content of the current chapter records the evolution of the VCCT model and how its capabilities increased step by step from the start, until the end where a good correlation was found between the modelling results and the stiffened OCT specimen test data from chapter 3.

6.2 VCCT model construction & verification

As this was the initial model construction phase, it was believed that a simple specimen geometry would be beneficial as this would reduce the number of variables considered. The VCCT failure criterion in ABAQUS requires the input of a critical strain energy release rate, G_{Ic}, for the nodes along the predefined fracture surface. It was initially proposed to model simple specimens with pre-existing test data. However, an issue quickly arose when considering this approach - the high number of variables involved in experimental tests means it is difficult to verify if any potential deviation between the test data and the modelling result is due to an inherent issue with the model or anything else. Hence it is crucial to find a method that involves as few variables as possible. Conveniently, the American Society for Testing and Materials (ASTM) publishes many standards for testing various specimens, one of which is of particular interest to this chapter - ASTM E399 [12] is a standard for determining the fracture toughness. The E399 standard provides detailed schematics and requirements for the specimen geometries, as well as a data reduction method for calculating the fracture toughness. Despite the E399 standard being developed for metallic structures, it is still of value to this chapter since the composite concerned has quasi-isotropic material properties.

The VCCT model development started off with constructing a specimen that is in strict accordance with the ASTM E399 standard which employed a compact tension specimen geometry. All specimen geometries were based on figure 6.2, with the width of the specimen being 100 mm and the notch length ranging from 50 mm to 58 mm with an interval of 2 mm. The specimen thickness is 4 mm. The value of W, as shown in the figure, is 80 mm.

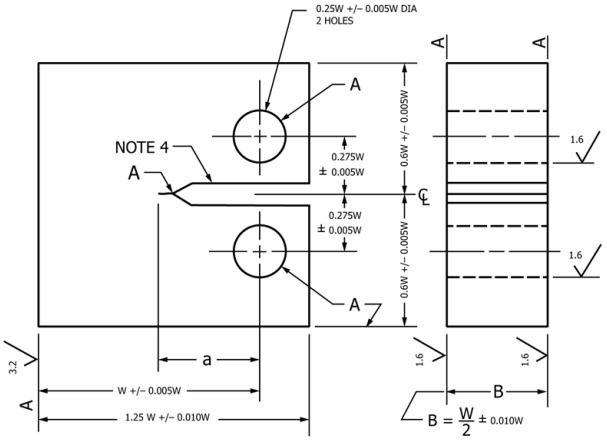

Figure 6.2: Compact C(T) Specimen—Standard Proportions and Tolerances [12]

The rationale behind choosing the compact tension specimen from ASTM E399 standard to be the geometry for the initial model is as follows - the standard [12] provides a set of detailed specimen geometry requirements and a corresponding data reduction method for calculating the stress intensity factor, K, shown in equation 6.2. As such, the VCCT model can be verified against a known analytical solution.

$$K = \frac{P}{B\sqrt{W}} f(\frac{a}{W}) \tag{6.2}$$

where:

$$f\left(\frac{a}{W}\right) = \frac{\left(2+\frac{a}{W}\right)\left[0.886+4.64(\frac{a}{W})-13.32(\frac{a}{W})^2+14.72(\frac{a}{W})^3-5.6(\frac{a}{W})^4\right]}{\left(1-\frac{a}{W}\right)^{3/2}} \tag{6.3}$$

for which:
P is the load of the interruption point, N;
B is the specimen thickness, m;
W is the specimen width as shown in figure 6.2, m;
a is the effective crack length as shown in figure 6.2, m.

Based on equation 6.2, K is a function of four variables - P, a, W, and B, out of which, B and W are both specimen geometrical parameters that are predetermined. P and a are two load/crack related variables that change throughout the duration of the test. To check the validity of the forthcoming VCCT model against the ASTM data reduction method, one could assume a load P_{ASTM} and a crack length a. Along with the two predetermined specimen geometries, the stress intensity factor K could be calculated via equation 6.2. On the other hand, the displacement controlled model requires specimen geometries and a G_{Ic} value for the VCCT failure criterion, with which it would output load, P_{VCCT}, as the result. The stress intensity factor K and the strain energy release rate G can be converted with the following equation - $G = K^2/E$, where E is the Young's modulus of the material. The VCCT model predicted P_{VCCT} value could then

be compared against the assumed P_{ASTM} value used previously as all other variables are kept constant between the two methods. Figure 6.3 shows the logic of the comparison behind the ASTM data reduction method and VCCT model.

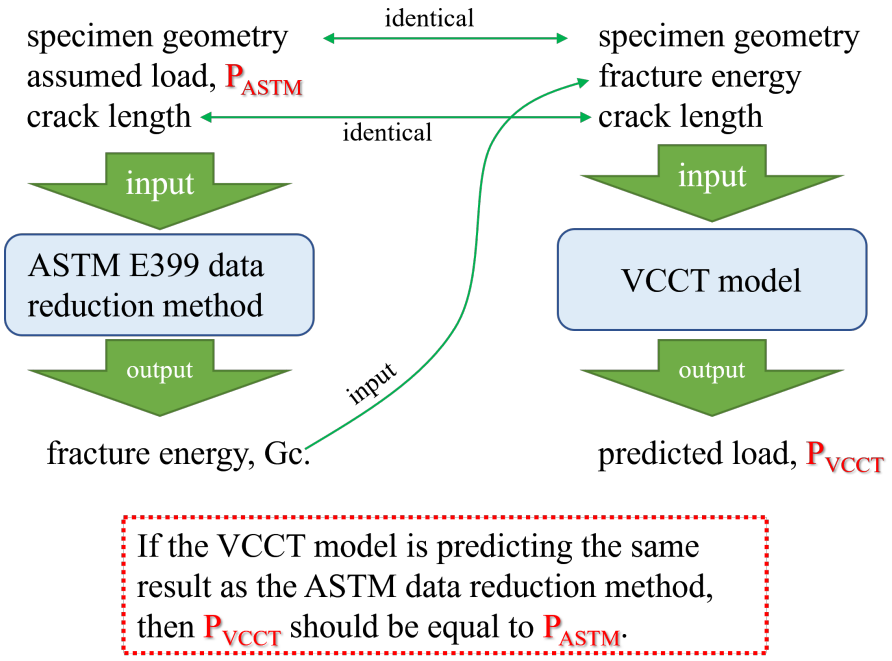

Figure 6.3: A graphical representation of the logic of comparing ASTM E399 data reduction method and the VCCT model. P_{ASTM} and P_{VCCT} should agree if the two methods were producing the same results.

The model consists of two parts: upper and lower, as the predefined fracture surface bisects the specimen in the centre line along its loading direction. Both the upper and lower parts are then placed into one single assembly. No loading holes were introduced in the model to reduce complexity as the loading holes are far away from the area of concern and do not impose much effect on the results. Figure 6.4 shows the assembly of the model. The material properties used in the model are as follows: homogeneous, elastic, isotropic, E=61400 MPa, and v=0.3, with 8-noded solid elements (C3D8). A static general step was created with nonlinear geometry turned on. Displacement control was applied to the centre of the loading hole locations, as marked by the red cross and arrow, with the red cross (bottom) indicating fixed boundary condition and the red arrow indicating displacement control in the positive y-direction. The detailed boundary conditions can be found in table 7.1, where directions 1, 2, and 3 correspond to the directions x, y, and z shown in figure 6.4. A 2 mm displacement was applied to the nodes at the centre of the upper loading pin at a rate of 1 mm/second. The minimum increment size was set to 0.002 seconds.

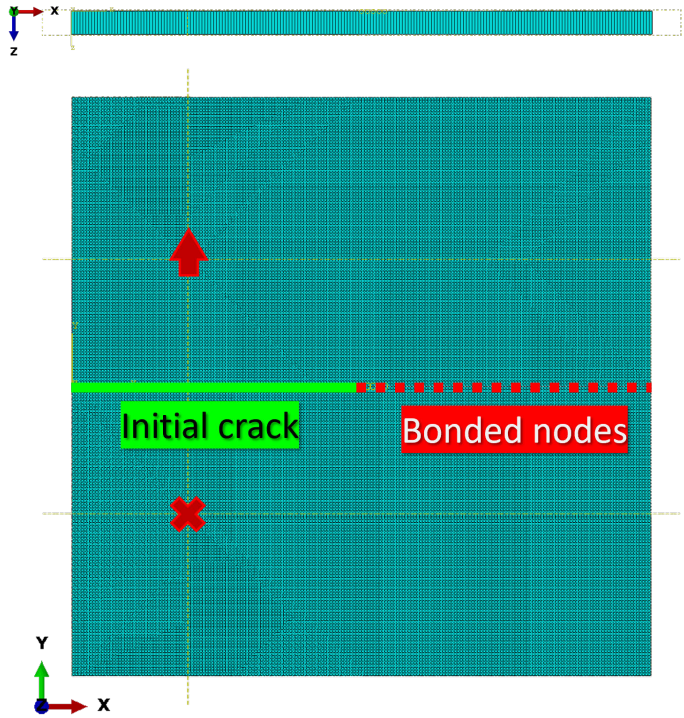

Figure 6.4: Compact tension specimen assembly in ABAQUS, based on the ASTM E399 standard.

Table 6.1: Boundary conditions applied to the top and bottom loading nodes. Boundary conditions applied to all nodes through the thickness at the centre of the loading locations. Directions 1, 2, and 3 correspond to directions x, y, and z in figure 6.4

Top	U1=U3=0; U2=2 mm
Bottom	U1=U2=U3=0

The key to an accurate crack propagation analysis is to correctly specify the parameters related to interactions. For this model, a surface-to-surface contact was employed, with the lower-part's top surface and the upper-part's bottom surface being the master and slave surfaces respectively. The contact interaction property was set to type VCCT, with their corresponding critical energy release rate set to the values calculated from ASTM E399 solutions. If the VCCT model is accurate, then its predicted load should match the assumed value used for the ASTM E399 calculations. A crack was introduced by defining a debonding node-set using VCCT, with the debonding force set to Ramp.

A meshing study was carried out to calculate the most cost effective mesh arrangements. The parametric study involved introducing various sizes of mesh (uniform mesh size across the whole model) to the same model with the same parameters, results approached an asymptotic value of 7.5kN and 10kN as mesh sizes decreased, however, the improvement was marginal as the size gets smaller than 1 mm. Two load levels were chosen as they would better represent the crack

Table 6.2: Numerical values of fracture energy used in VCCT modelling. All values in kJ/m^2. The fracture energy values in this table were calculated using the ASTM E399 data reduction method with the corresponding crack length shown.

	ASTM E399, CT Specimen				
	50mm	52mm	54mm	56mm	58mm
10kN	59.14	67.41	77.07	88.49	102.16
12kN	85.16	97.07	110.99	127.43	147.11

onset and propagation situation. Given the results from the parametric study, for the remainder of this study, 0.5 mm was chosen as the default mesh size. Based on these established settings, a compact tension specimen model was constructed in ABAQUS with VCCT as the failure criterion. To make correlation with the ASTM E399 data reduction method simpler, the specimen geometry was in accordance with the standard, with the width of the specimen, W, equal to 80 mm, and thickness, B, equal to 4 mm, resulting in a specimen with outer dimensions of 100 mm by 96 mm. Uniform mesh throughout the specimen was used, with an element size of 0.5 mm.

Two sets of modelling were carried out, each set consisted of five crack length intervals, from 50 mm to 58 mm with an interval of 2 mm. The equation given by the ASTM E399 data reduction method was firstly used to analytically calculate the critical strain energy release rate, G_C, given an assumed crack propagation load, P_{ASTM}. Set No.1 was given an assumed propagation load of 10 kN, while set No.2 was given an assumed propagation load of 12 kN. The rationale behind having two sets of assumed loads were to replicate the crack onset and propagation. These assumed P_{ASTM} values were chosen as they would induce a reasonable strain energy release rate. For each crack length and assumed failure load combination, a unique strain energy release rate was obtained, these G_C values were then input into their corresponding ABAQUS models to model the crack propagation behaviour. Figure 6.5 shows the load-displacement curves of the two sets of models, with the lower load set representing an assumed propagation load of 10 kN, while the higher load set representing an assumed propagation load of 12 kN. For numerical values of the fracture energy used during the simulation for all models, please refer to table 6.2.

Results from the compact tension specimens yielded high resemblance to the ASTM E399 data reduction method. As can be seen in figure 6.5, for both the 10 kN load level and 12 kN load level, almost identical results were obtained at 50 mm crack length. Disagreement between modelling results and analytical solution increases as the crack length increases, reaching a maximum of 3% difference at crack length 58 mm, with the modelling prediction being higher than its respective assumed load.

The high resemblance seen between the VCCT modelling results and the ASTM E399 data reduction method demonstrates the validity of the VCCT modelling method. Therefore, the methods and the concepts used in this VCCT model will be used as a foundation in the next section to develop a more sophisticated model.

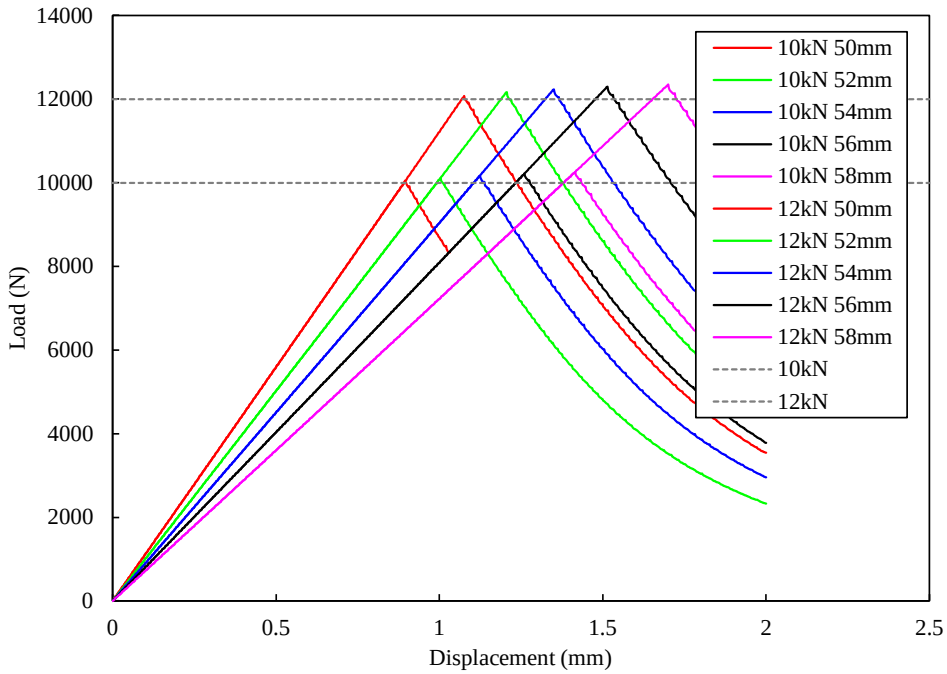

Figure 6.5: Load vs displacement curves obtained from VCCT modelling of a CT specimen based on ASTM E399. The horizontal black dashed lines represent the assumed load of 10 kN and 12 kN for calculating the input G value using the ASTM data reduction method.

6.3 Enhanced VCCT & nodal energy rates methods

Until this point, the model utilised the VCCT fracture criterion, where the crack onset and propagation are based on one single critical energy release rate. While such a failure criterion may be sufficient in predicting the crack onset load, however it is unable to capture any change in the critical energy release rate during the crack propagation, also known as the resistance curve (R-curve). R-curves describe the relationship between the fracture resistance R and the crack increment Δa. To partially resolve this shortcoming, the ABAQUS Enhanced VCCT (EVCCT) method could be employed, where two values of critical fracture energy release rate can be specified, for the onset and propagation of the crack, respectively. Compared to curves obtained from the VCCT fracture criterion, EVCCT enables a two-stage crack propagation, where the linear portion of the curves prior to the peak load now includes a slight change in gradient. While EVCCT can capture the onset and propagation of the crack, it lacks the ability to define an R-curve where the critical strain energy release rate needs to be defined as a function of crack length.

To resolve this issue, there is a third type of VCCT criterion – nodal energy rates. Compared to the VCCT and EVCCT criteria where only one or two values of critical strain energy release rate can be specified, nodal energy VCCT permits the specification of a critical strain energy release rate for every node along the crack front. Thus an R-curve can be specified. Figure 6.6

shows a graphical comparison between VCCT, EVCCT and nodal energy VCCT. Where VCCT assigns one value of G_c for the entire crack length, EVCCT enables a separate initiation and propagation G_c value; and lastly, nodal energy VCCT permits the specification of a G_c value for every node.

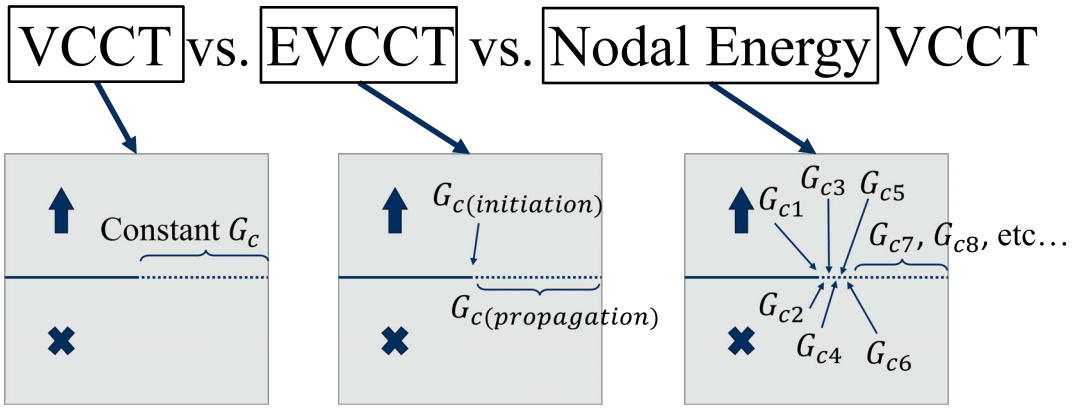

Figure 6.6: Graphical comparison between VCCT, EVCCT and nodal energy VCCT.

To compare the nodal energy VCCT model with the ASTM E399 data reduction method, the compact tension specimen from the ASTM E399 standard was chosen to be the geometry for the initial nodal energy VCCT model as it is a large specimen with a long crack length which enables a refined R-curve specification. In addition, the E399 standard data reduction method showed a very good correlation with the initial VCCT model in section 6.2. Figure 6.7 shows the compact tension specimen with its mesh arrangements in the nodal energy VCCT model. The loading points are marked by the red cross and arrow, where the cross at the bottom indicates the bottom loading point where a fixed boundary condition was applied and the arrow at the top indicates the top loading point where an upward displacement was applied. The machined notch, denoted by the red horizontal line, is represented in the model via detached nodes. The nodes on the fracture surface to the right of the machined notch are in contact via surface-to-surface contact. With the first set of nodes to the right of the machined notch being at 0.5 mm, the second set at 1 mm, etc. The nodal energy VCCT model requires the input of G_C values for every node along the crack path, data used were obtained from figure 9 in reference [14]. Figure 6.8 details the strain energy release rate values used as a function of crack increment in the model. The extra low value at 0.5 mm is a numerical trick to get the propagation started, if left at zero, the crack would not start to propagate.

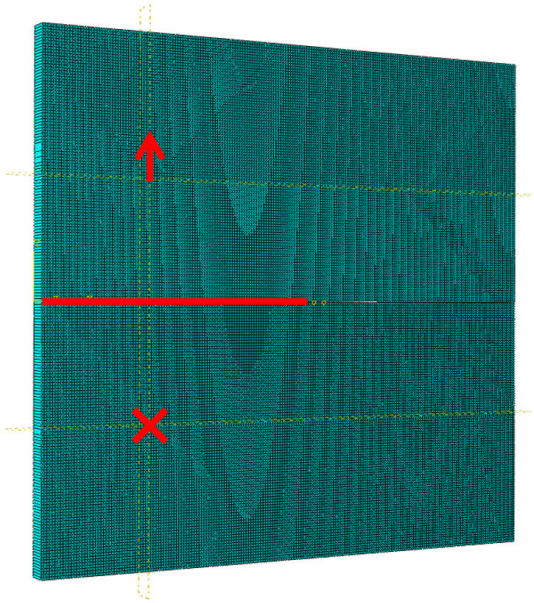

Figure 6.7: Compact tension specimen used in the initial nodal VCCT model.

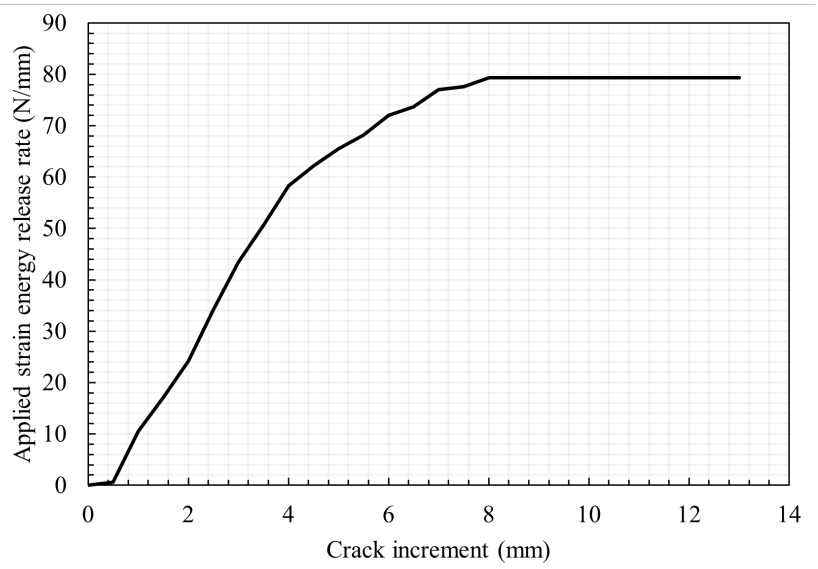

Figure 6.8: Strain energy release rate, G, applied to the compact tension nodal energy VCCT model, data from [14].

Figure 6.9 shows the load-displacement curve of the nodal energy VCCT model. Compared to load-displacement curves from previous VCCT model, the nodal energy load-displacement curve displays a more gradual transition with less sharp load drop between 1 mm to 1.5 mm displacement, a clear indication of an R-curve effect. Furthermore, every small load drop visible in the POD curve represents a crack propagation by one element.

To compare the nodal energy VCCT solution against the ASTM E399 data reduction method,

data from figure 6.8 could be utilised. By plugging each tip location's corresponding crack length and G_C value into the ASTM E399 data reduction equation, a load value for every crack length can be calculated. The blue markers in figure 6.10 represent the ASTM E399 calculated load values for each crack length and G_c value combination. An extremely high degree of agreement can be found between the nodal energy VCCT model and the ASTM E399 data reduction method, proving the validity of the nodal energy VCCT model. It should be noted that the oscillations seen in the FE curve are load-drops that occur as the crack propagates by one element, and because the R-curve is increasing, the load goes up again, hence the oscillations. This phenomenon does not occur during the unloading part as that part has a constant R-curve. Without the clear load-drops it is difficult to correlate crack length with displacement, therefore it is difficult to accurately add the ASTM calculated points (red) to the unloading part of the FE load curve (blue).

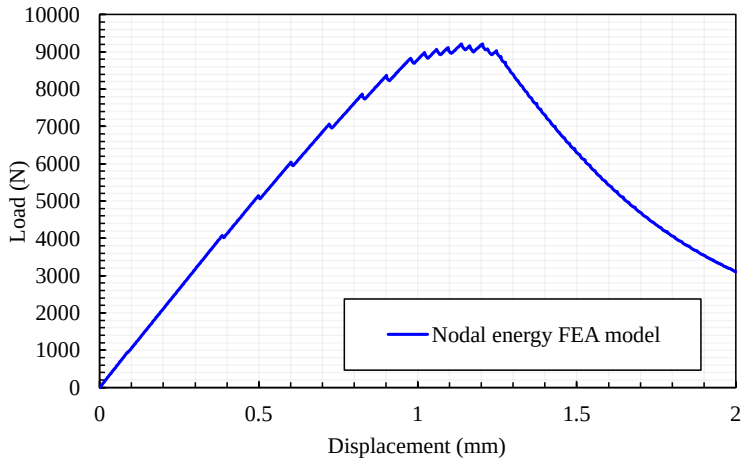

Figure 6.9: Load vs displacement curve obtained from nodal energy VCCT model of a compact tension specimen.

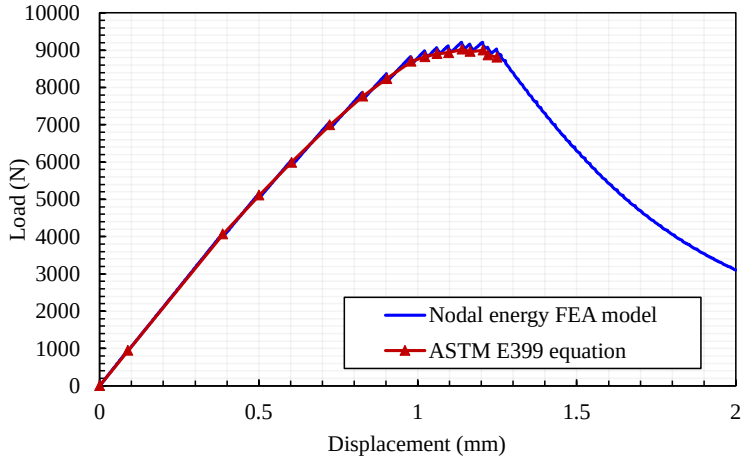

Figure 6.10: Load vs displacement curve obtained from nodal energy VCCT model of a compact tension specimen compared with ASTM E399 data reduction method.

6.4 Stiffened OCT model with cohesive elements

6.4.1 Background

In the previous sections, the three types of VCCT models have been looked into, those being - VCCT, enhanced VCCT, and nodal energy VCCT, shown in figure 6.6. Nodal energy VCCT is the most comprehensive and advanced type of VCCT implementation out of the three as it enables the customisation of the critical strain energy release rate on a node-by-node level. Thanks to nodal energy VCCT, very accurate results have been achieved when compared against the data reduction method of ASTM E399, as demonstrated in figure 6.10. However, there are still some shortcomings that need to be addressed -

1. All models so far are based on ABAQUS implicit, it poses the issue of not converging when faced with complex contact/boundary conditions. The alternative to implicit analysis is explicit analysis, which is very suitable for models with complex interactions and loading/boundary conditions. The ability of explicit models to cope with complex conditions would be especially useful when modelling large stiffened panels. In addition, explicit models can also be less computationally demanding compared to implicit when faced with complex/large models with many elements.

2. The models so far are based on a simple specimen geometry, namely the compact tension specimen from the ASTM E399 standard, shown in figures 6.2. While this simple specimen geometry offers the possibility to compare the FEA model with a published standard data reduction method, it lacks the ability to investigate some more interesting failure mechanisms, namely delamination and debonding.

3. The models so far have been using a uniform mesh across the entire model, while this practice offers the highest possible degree of accuracy, it is very computationally demanding on the other hand. Hence a coarse mesh would be required away from the crack surface to aid in reducing the computational resources required.

4. To further reduce computing time, a half model through the thickness could be introduced with the plane of symmetry in the thickness direction leading to an almost 50% reduction in computing time.

6.4.2 Model construction

Given the ultimate goal of the PhD project to develop a cost-effective modelling method for translaminar fracture in stiffened panels, it is of vital importance to have a sound method to model the crack-stringer interaction. To investigate the interaction of crack propagation with stringers, the previously modelled compact tension specimen geometry was no longer fit for

purpose. A great alternative to the afore-modelled compact tension specimen would be the Over-height Compact Tension (OCT) specimen with stringer foot due to its stable damage growth [135] and the reduced probability of failing under compression at the top and bottom edges. There has been some existing work by Xu et al. [8] on the fracture response in OCT specimens of three sizes, scaled down, baseline, and scaled up, and each size has a factor of two in the in-plane dimensions compared to its smaller version. For the purpose of this model, the baseline specimen geometry will be used. For a detailed specimen geometry please refer to figure 6.11.

The updated stiffened OCT model consists of three parts - the skin, cohesive elements, and the stringer. The cohesive elements are located in between the skin and the stringer which enable debonding to take place if necessary. The half model consists of a half-skin of thickness 2 mm, a layer of cohesive elements in contact with the skin of thickness 0.01 mm, and finally a stringer of thickness 0.5 mm. The cohesive element thickness of 0.01 mm was chosen to be thin enough not to introduce additional compliance to the model. This half model would represent a real specimen with a skin thickness of 4 mm and a 0.5 mm thick stringer co-cured to each side of the skin. Figure 6.12 shows a side view of the specimen modelled. The properties of the skin and stringer elements are kept unchanged from before, while the properties of the cohesive elements are: Nominal strength normal– 60 MPa, nominal strength 1st and 2nd shear directions – 90 MPa; G_{Ic} = 0.2 kJ/m^2 & G_{IIc} = 1 kJ/m^2. Mixed mode behaviour was set to energy based power law with power = 1. The model has a uniformly fine mesh (0.5 mm) around the crack surface, with a coarse mesh around the other areas to reduce runtime, shown in figure 6.13. The model has one element through the thickness.

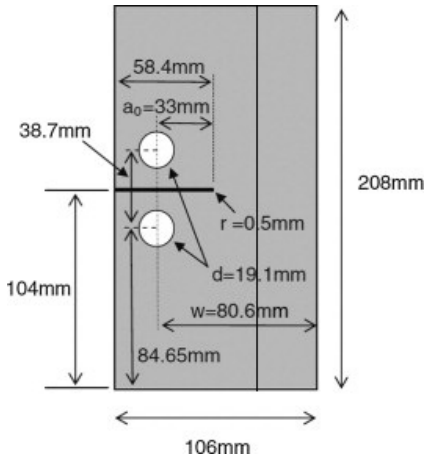

Figure 6.11: Schematic of the baseline OCT specimen [8]

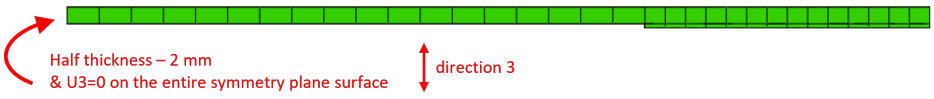

Figure 6.12: Schematic of the half model, top view.

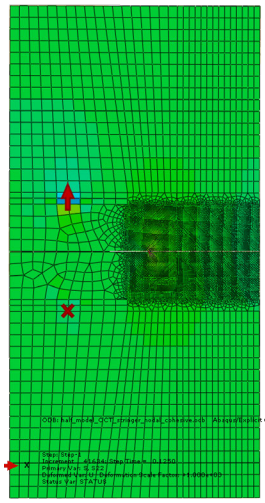

Figure 6.13: Mesh distribution and loading points of the VCCT half model.

The nodal energy VCCT fracture criterion requires the specification of a critical strain energy release rate, G_c, for every node on the crack plane. For instance, the set of nodes located 0.5 mm away from the machined notch would be assigned a critical strain energy release rate, G_{C1}, the set of nodes located 1 mm away from the machined notch would be assigned a critical strain energy release rate, G_{C2}, etc. But when it comes to assign the G value to the stringers - two methods arise - Type 1 and Type 2.

1. Type 1 indicates the G_c value assigned to the stringer is the same as the node on the skin right behind it.

2. Type 2 indicates the G_c value assigned to the stringer has its own ramp up and is independent of the skin behind it.

To better visualise the difference between Type 1 and Type 2 nodal energy VCCT criterion please refer to figure 6.14. The G_c profile applied in this model, shown in figure 6.15, is based on the predicted effective R-curve based on effective crack increments from the Hi-FEM analysis by Xu et al. [14], shown in figure 6.16. The rational of introducing the Type 1 and Type 2 R-curves is that these two types of stringer R-curves represent the two extreme ends of the spectrum, where the stringer either has exactly the same R-curve as the skin beneath it or the stringer has its own independent R-curve. The length of the crack where the stringer R-curve ramps up was chosen such that the skin and stringer R-curve would meet at the end of the nodal energy portion. It should be noted that when this piece of study was carried out, no experimental R-curve was available yet. The distribution of the nodal energy VCCT nodes along the crack face is illustrated in figure 6.17.

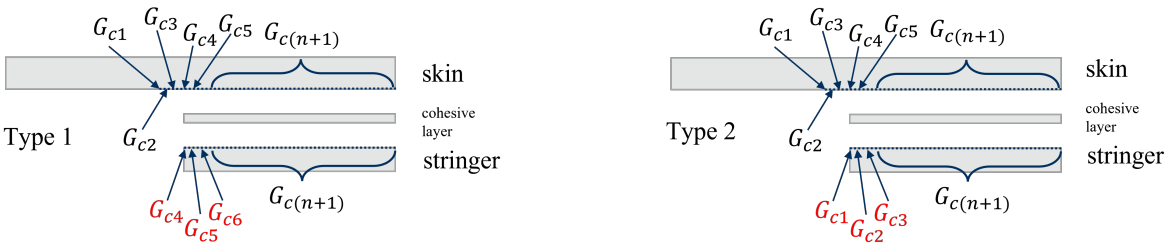

Figure 6.14: Schematic comparison between Type 1 and Type 2 nodal VCCT.

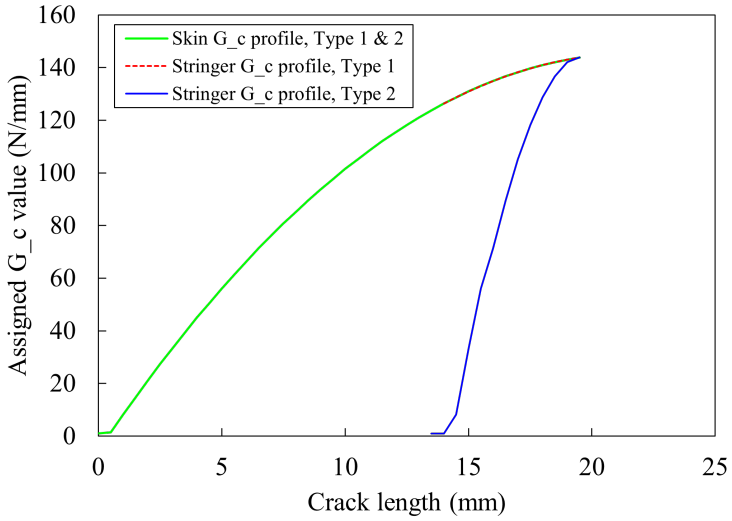

Figure 6.15: Comparison of the applied R-curves against crack length for Type 1 and Type 2 nodal energy VCCT.

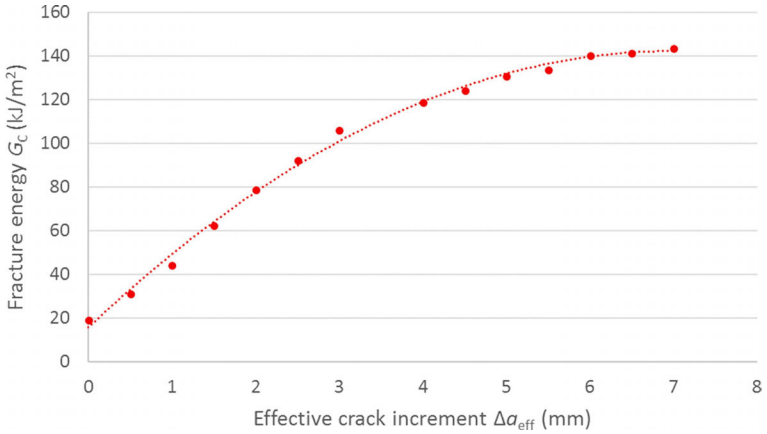

Figure 6.16: The predicted effective R-curve based on effective crack increments from the Hi-FEM analysis [14].

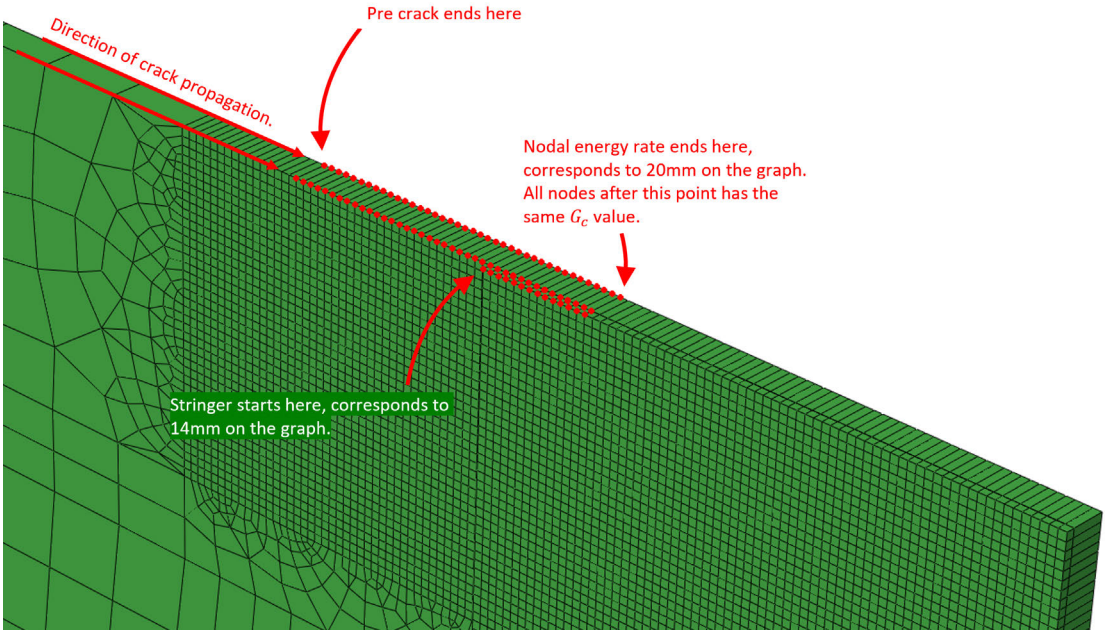

Figure 6.17: The distribution of the nodal energy VCCT nodes along the crack face.

6.4.3 Preliminary results of the half model with cohesive elements

Figure 6.18 shows the preliminary results of the nodal energy VCCT model with cohesive elements, where normal VCCT represents a single-stage VCCT model which has the same plateau G_c assigned to the entire crack path. Type 1 (green curve) nodal energy VCCT model displays an earlier crack onset compared to the normal VCCT case, which is to be expected as the G_c value starts from zero at the beginning of the crack. When the crack propagates to the stringer, the load increases slightly, at around 1.6 mm displacement. Towards the end of the crack, type 1 and the normal VCCT curves meet again as both cases have the same far field G_c value. On the other hand, the type 2 (red curve) nodal energy VCCT model curve displays a higher load than both of the others towards the end of the curve. This raises some questions which will be addressed at a later stage. Type 1 & 2 G_c curves represent the two extreme cases, where type 1 indicates the stringer has exactly the same G_c curve as the skin behind it, and type 2 indicates the stringers G_c curve is completely independent from that for the skin. It could be argued that the reality is somewhere in between these two cases, where the stringer would have its own G_c curve, to begin with, and slowly merges with the skin. The exact distribution is yet to be confirmed and requires further work, especially some sound experimental results. In both types of the R-curve application, the very first sets of nodes in the stringer were disconnected which artificially creates a crack with a length of one element (0.5 mm). This would firstly enable the nodal energy VCCT criterion to function and secondly can mimic the damage done to the

stringers when a crack in the skin propagates underneath/past the stringer. Furthermore, an assumption was made that the nodal energy crack length is 20 mm, after which, the G_c stays constant at this maximum value. This has been done to reduce the modelling complexity and has no negative effects on the result as the R-curve reaches a plateau before 20 mm.

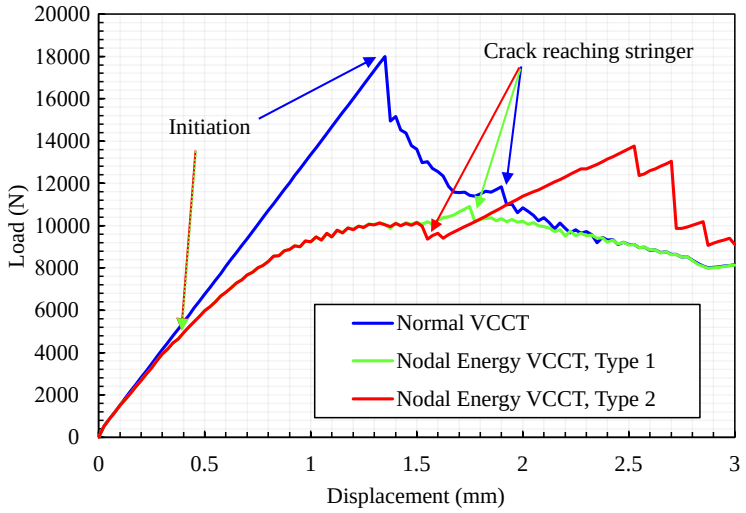

Figure 6.18: Load displacement curves of the half model nodal energy VCCT model.

The higher load level seen in the type 2 nodal energy VCCT curve is still open for consideration. Given that the type 2 G_c distribution is identical to that of type 1 after 20 mm of crack length, the load displacement curves ought to be identical. However, initial results states the opposite – load levels of the type 2 curve is substantially higher than type 1. After some careful examination of the FEA stress contour, it is believed the substantial higher load level seen in the type 2 curve is attributable to an asymmetric crack propagation occurring between the front and centre plane of the specimen, shown in figure 6.19.

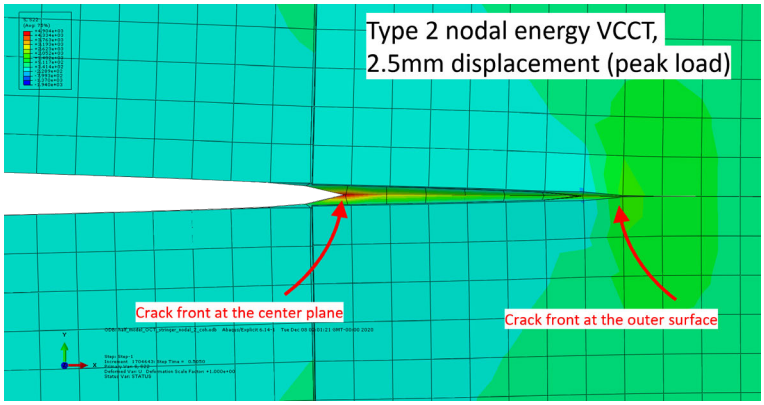

Figure 6.19: Asymmetric crack propagation between the front and back surface.

To resolve the issue of asymmetric crack propagation in the thickness direction, four layers

of elements were introduced in the thickness direction, shown in figure 6.20. This was found to be sufficient to eliminate the numerical errors associated with one element through the thickness. The reduced element through thickness dimension means a smaller load deviation between the two nodes in one element, hence rendering a more symmetric crack propagation pattern. Figure 6.21 shows the load-displacement curve of the model without asymmetric crack propagation. The normal VCCT curve (red) ought to yield the highest strength as the entire crack length was assigned the max G_c value of 143 kJ/m^2. Type 1 nodal VCCT (blue) corresponds to the stringers having the same G_c value as the skin, hence exhibiting higher stress between 1.5 to 2.5 mm displacement. Type 2 nodal VCCT, as the stringer has its own G_c curve, yields the lowest stress overall. All three types of VCCT curves coincide after 3.8mm of displacement, which is to be expected as the G_c value all reaches the max value of 143 kJ/m^2.

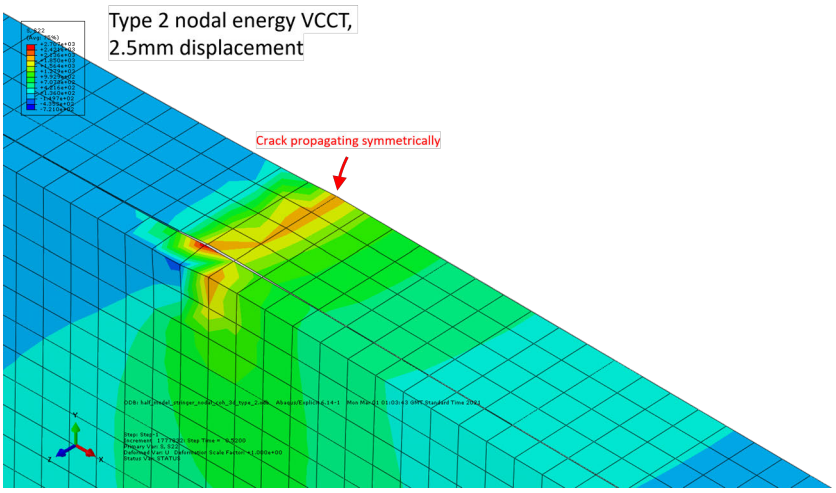

Figure 6.20: Asymmetric crack propagation resolved by introducing four elements through the half thickness.

In addition, each curve has a load drop associated with the crack propagation in the stringers, indicated by the correspondingly coloured circles, see figure 6.21. The normal VCCT curve exhibits the largest load drop as the G_c value at the front of the stringer is the highest, at 143 kJ/m^2. The crack has to propagate quite far in the skin in order to trigger crack propagation in the stringer. Similarly, Type 1 nodal VCCT has a higher stringer front G_c value than Type 2 nodal VCCT, hence the larger load drop. Figure 6.22 shows the status of the cohesive elements located between the skin and stringer just before the major load drops with blue indicating pristine cohesive elements and red indicating failed cohesive elements - meaning the area shown in red have debonded. The dots on the curves in figure 6.21 indicate where each snapshot was taken. Since the normal VCCT failure criterion is a basic type of the nodal-energy VCCT criterion, it will be replaced with the nodal-energy VCCT criterion hereafter.

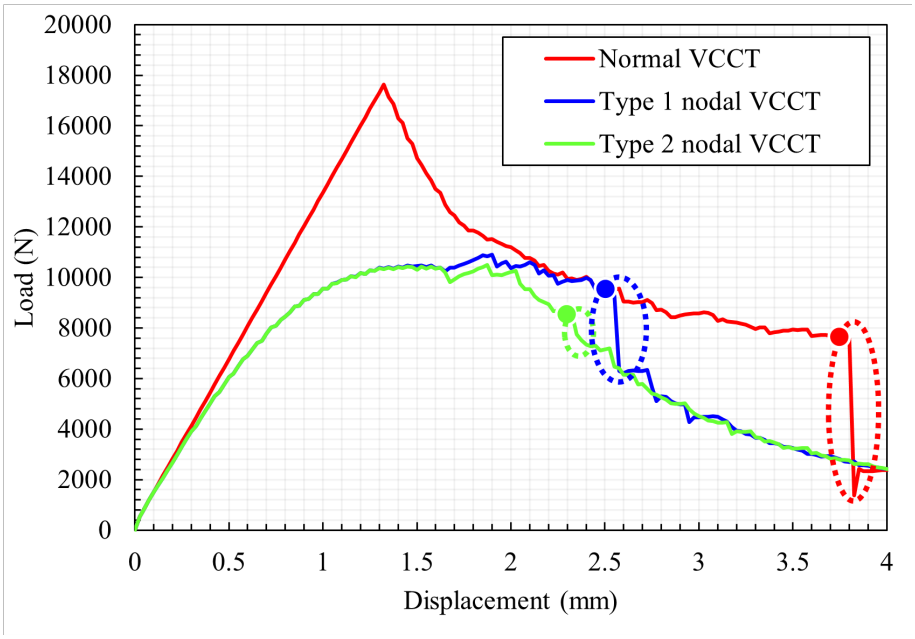

Figure 6.21: Load displacement curves of the half model nodal energy VCCT model with four elements in the thickness direction.

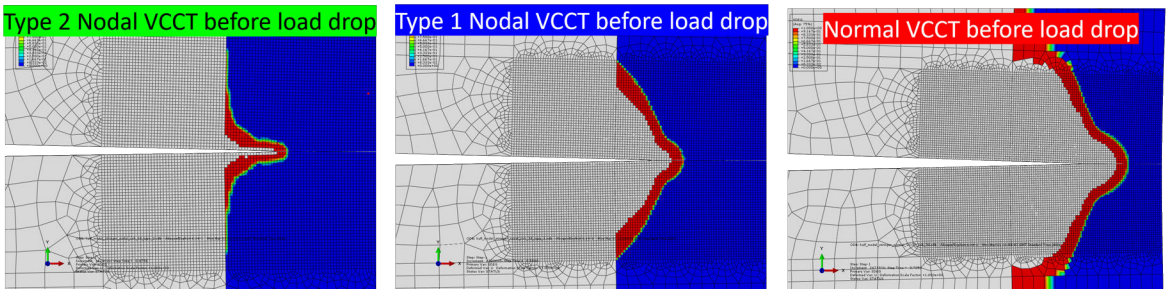

Figure 6.22: Delamination between skin and stringer before major load drops indicated in figure 6.18.

6.4.4 Limitations of the half model with cohesive elements

Currently the model contains a 0.5 mm thick stringer foot only, it is proposed that a thicker stringer foot model would offer more insight into the crack stringer interaction, hence a 2 mm thick stringer foot model will be added. In addition, the R-curve applied currently is based on the Hi-FEM analysis carried out by Xu et al. [14], some experimental input for the R-curve would be a much needed addition as test data have now become available.

6.5 Model with new experimental R-curve

So far the modelling of crack interaction with stringers in OCT specimens has been looked into. It is obvious that the critical strain energy release rate curve applied, G_c, plays a vital role in

the model. Up till this point Xu's [14] Hi-FEM R-curve has been the only source of data despite its numerical origin. A set of OCT specimens of the same material, geometry, and layup as the one modelled previously were tested [13] which provided the experimentally derived R-curve. This is a much-needed addition as it provides a second source of R-curve data that is completely independent of the previous modelling results. The specimens contained three sizes - scaled-down, baseline, and scaled-up. The baseline geometry is identical to those modelled previously. All specimens are geometrically proportional in-plane, with a factor of two between each size. The baseline specimen has the same dimensions as shown in figure 6.11. Figure 6.23 shows the experimentally determined R-curve. Based solely on the data shown, we can not see a plateau at the top of the R-curve. Hence either the plateau does not exist or the specimen is still not large enough. As such, one of the two assumptions is made with regard to the R-curve plateau -

1. The plateau takes place straight after the last known point in figure 6.23.
2. The R-curve keeps its linear trajectory and plateaus at a later stage.

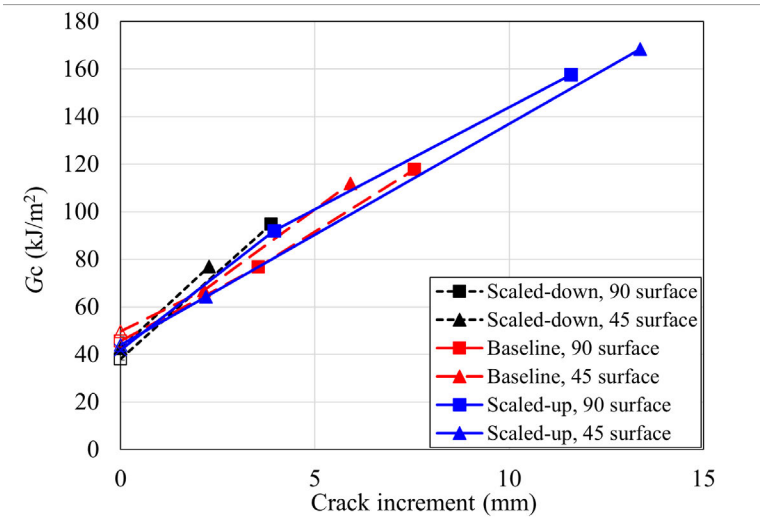

Figure 6.23: Experimentally determined initial R-curves [13].

The implementation of the experimental R-curve can be found in figure 6.24. The mesh size of the model around the crack surface is 0.5 mm, hence a fracture energy value is given to each element at an increment of 0.5 mm for a total nodal energy length of 20 mm, after which the fracture energy value stays constant. Figure 6.25 shows a schematic of the nodal energy implementation on the crack surface.

Results of the models with the new experimental R-curves are in figure 6.26 and 6.27. For the 0.5 mm stringer thickness case, type 1 nodal energy VCCT criterion induces higher loads when the crack reaches the stringer as expected due to its comparatively higher fracture energy, though the trend of the two curves is the same. For now no conclusion can be drawn as to whether type 1 or type 2 nodal energy VCCT is more representative of reality. Type 1 nodal energy VCCT will be

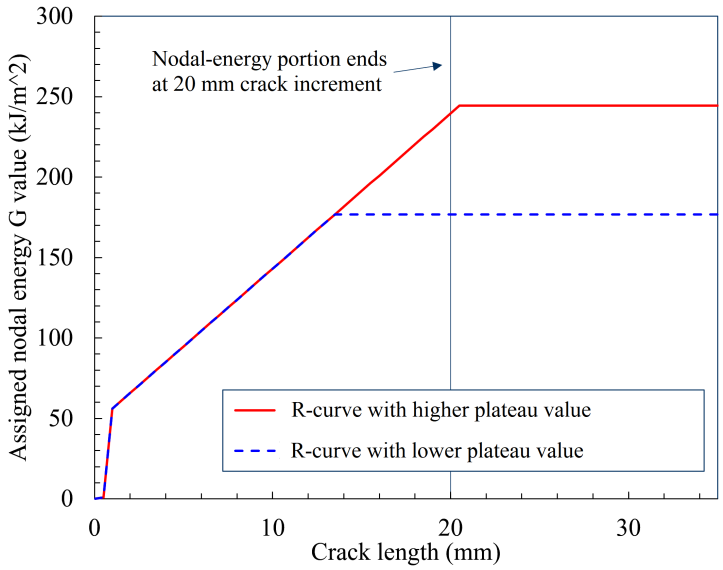

Figure 6.24: Implementation of the experimental R-curves in nodal energy VCCT model.

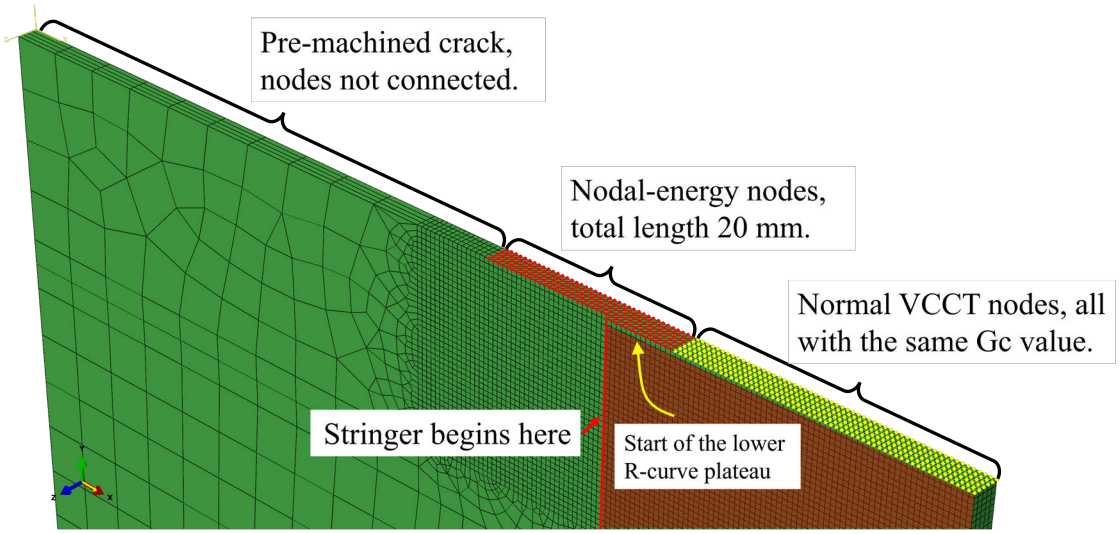

Figure 6.25: Schematic of the nodal energy nodes on the crack surface.

used for now for simplicity, however, this assumption will be reviewed with experimental data which is presented in the following section. For the 2 mm stringer thickness model, as expected, the higher plateau R-curve model yields higher loads after the crack reaches the stringer due to the R-curve's linear trajectory. No conclusion can be drawn as to which is more accurate, the higher plateau or the lower plateau R-curve, until some experimental data are introduced for comparison.

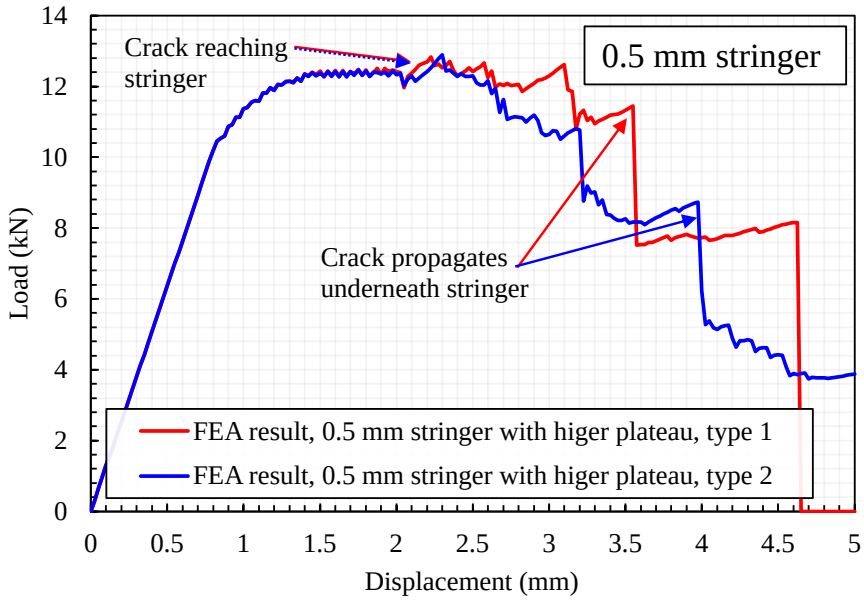

Figure 6.26: Load displacement curves for Type 1 and Type 2 nodal energy VCCT model with 0.5 mm stringers with the higher plateau R-curve.

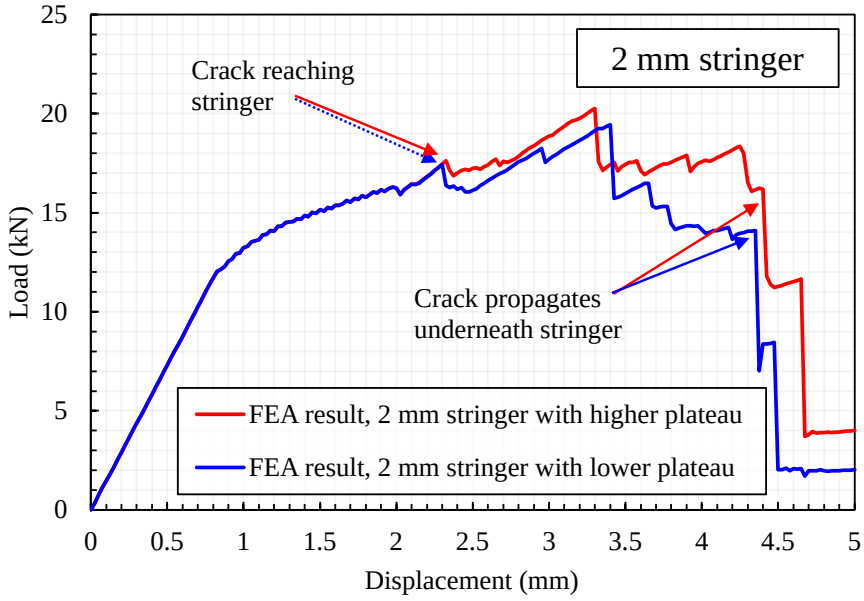

Figure 6.27: Load displacement curves for Type 1 nodal energy VCCT model with 2 mm stringer with lower and higher plateau R-curves.

6.6 Comparison with experimental data

In chapter 3, test data of the stiffened OCT specimens were detailed and presented. Test results showed both the 0.5 mm stringer and 2 mm stringer specimens suffered from skin-stringer

debonding, although to a different extent. As debonding area grew, more load was transferred from the skin to the stringers, which led to the thinner 0.5 mm stringers failing in tension while the 2 mm stringers were still intact. With the additional modelling data from this chapter, the logical next step would be to compare the experimental results against the modelling results. Figure 6.30 and 6.31 shows the correlation between nodal energy VCCT model and test results for 0.5 mm stringer specimens and 2 mm stringer specimens respectively. The comparisons here for the load-displacement curves are with the type-1 nodal energy curve as type-2 nodal energy curve has been found to be less accurate. In addition, figures 6.30 and 6.31 show the crack length as a function of displacement for the 0.5 mm case and 2 mm case respectively.

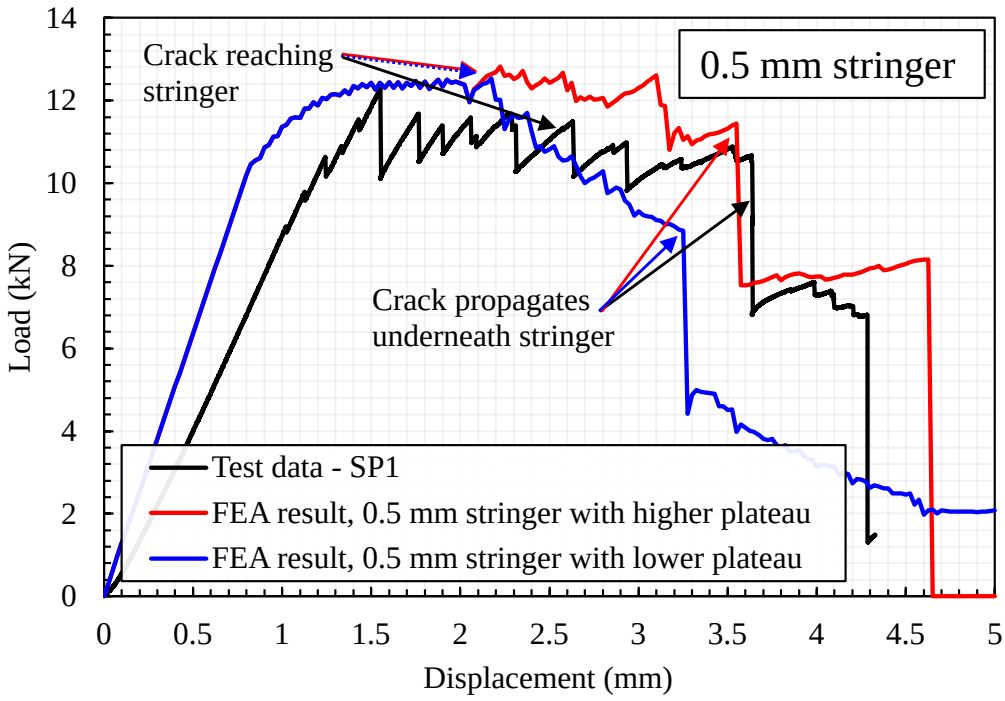

Figure 6.28: Correlation between FEA results and test results (0.5 mm stringer case).

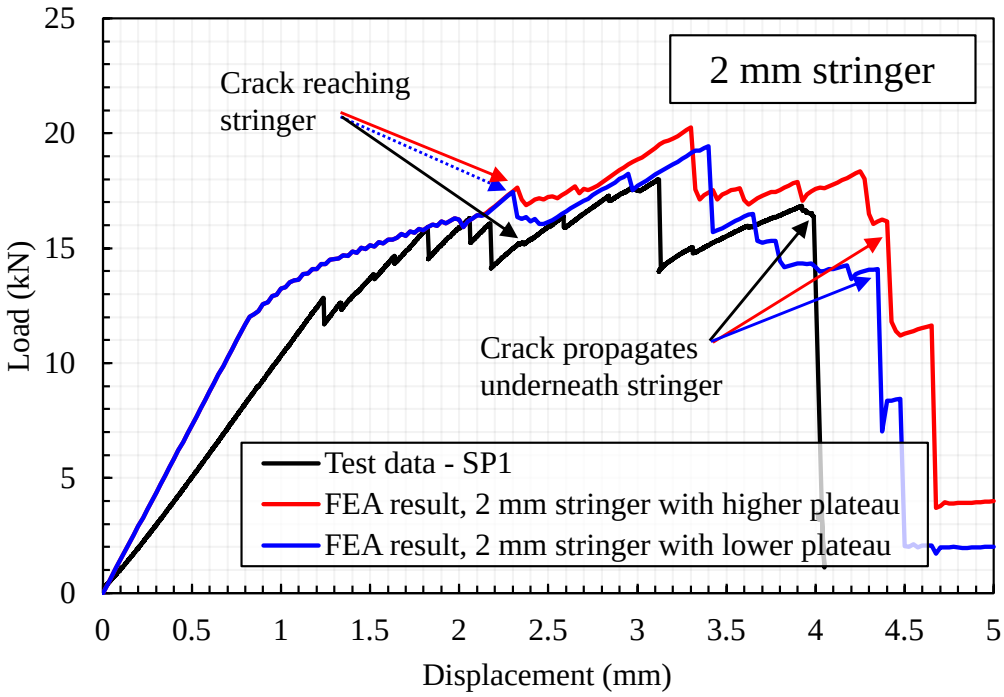

Figure 6.29: Correlation between FEA results and test results (2 mm stringer case).

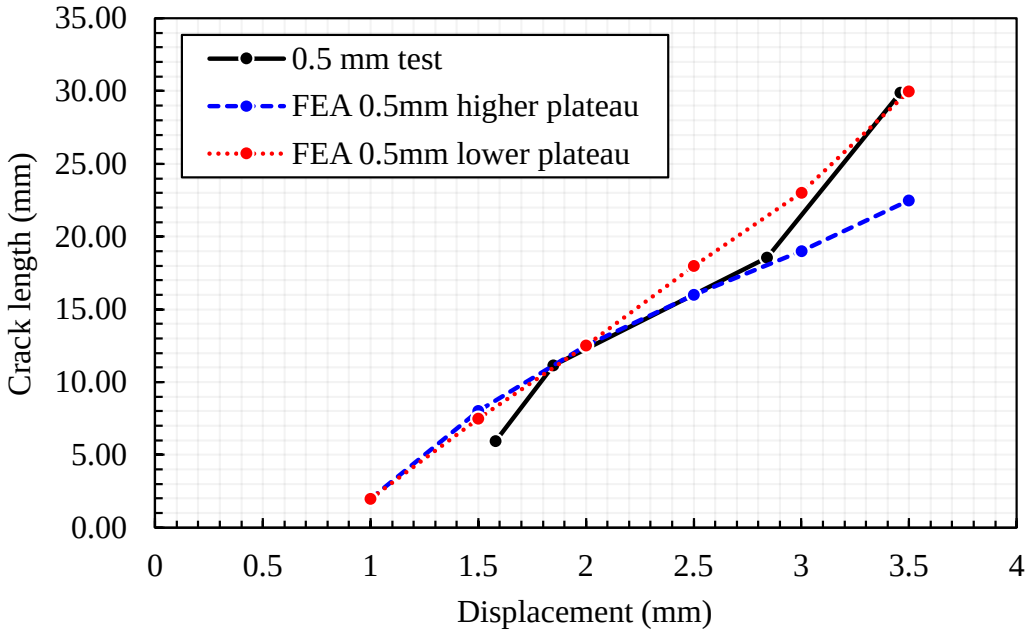

Figure 6.30: Crack length as a function of displacement (0.5 mm stringer case).

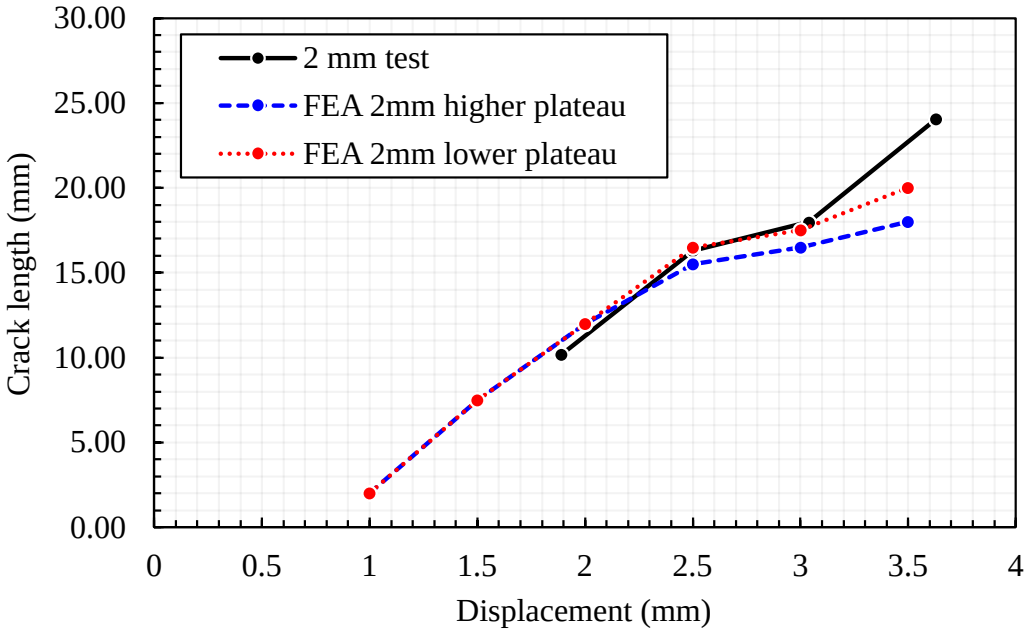

Figure 6.31: Crack length as a function of displacement (2 mm stringer case).

Results demonstrate a very good correlation between FEA and test results, both for 0.5 mm and 2 mm stringer cases. Both model results have a higher initial stiffness than their corresponding test result, which is understandable as the test machines would unavoidably have some slack and compliance. For the 0.5 mm stringer case, the maximum load achieved during testing and the predicted max load were almost identical at approximately 12 kN. It could be argued that the higher plateau R-curve model for the 0.5 mm stringer cases correlated with test results marginally better than the lower plateau R-curve model. The higher plateau R-curve model showed a relatively flat load level between 1 to 3 mm displacement - showing a slight over prediction compared to the test result. As per the annotations in the figure, the modelling results show the crack reached the stringers at approximately 2.3 mm displacement. This is in line with the findings from the CT scans of the stiffened OCT tests, where the crack reached the stringers between the two interrupted specimens - SP5 and SP6 (corresponding to 1.8 mm and 3 mm displacement), see figure 3.11. Likewise, the load drop seen at 3.6 mm displacement is owing to the crack propagating in the stringer that has been very well captured by the nodal energy VCCT model.

For the 2 mm stringer case, the general trend of the test results was predicted by the nodal energy VCCT model very well, both the higher plateau R-curve model and the lower plateau R-curve model showed equally satisfactory results. Modelling results show that the crack reached the stringer at around 2.3 mm displacement, which is in a very good agreement with test results, shown in figure 3.10 and 3.12. Additionally, the load drops at 3.5 mm displacement in the modelling results also correspond well with the load drop at 3.1 mm in the test result - where a significant crack propagation is seen in the skin. The model also correctly reflected the fact that

the stringers themselves did not fail but rather debonded from the skin.

The mismatch in stiffness between the simulated results and the test results in both the 0.5 mm case and the 2 mm case is believed to have been caused by the simplified assumption of the loading methods between the two cases. For the tests, the specimens were loaded via a loading pin with a 19.1 mm diameter. Whereas in the simulation models the loading boundary conditions were applied at the centre point of the loading holes. The high stresses at the loading points in the simulations could have caused some local deformation, which in turn would result in the stiffness mismatch seen. Since the stiffness does not come into the calculation of K as shown in equation 6.2, and the E used when calculating G from K were taken from previous literature, hence it is an acceptable simplification to be made.

6.7 Conclusion

To summarise, this chapter detailed the evolution and progress of the VCCT model, from a simple VCCT model with very simple geometries and a single critical strain energy release value to a nodal energy VCCT model that is capable of predicting translaminar fracture in stiffened OCT specimens using R-curves. A good correlation was found between the numerical predictions and test results, for both sets (0.5 mm and 2 mm stringer stiffened OCT) of specimens also. For a fairly computationally inexpensive model (typically 6 hours on a PC with 28 cores), the results predicted are relatively accurate and conservative, two factors that would make it especially appealing for industrial applications. With the nodal energy VCCT model established for the stiffened OCT specimen, the next step would be to implement this method to the large stiffened panel, fulfilling the ultimate goal of this PhD project.

CHAPTER 7

VCCT BASED MODELLING OF LARGE STIFFENED COMPOSITE PANELS

The previous chapter detailed the construction and development process of the nodal-energy-VCCT based modelling method for stiffened coupon geometries, modelling results showing a promising similarity against test data. This chapter builds upon the results from the previous chapter and pursues the ultimate goal of the PhD project - constructing a cost-effective modelling method for predicting translaminar fracture in large stiffened composite panels.

Two sets of experimental tests were carried out by Dr. Takeda back in 2013 which involved testing two smaller stiffened coupons and one large stiffened panel with three hat shaped stringers. The experimental results presented in this chapter can be found in ref. [11]. The goal of this PhD project is to develop a modelling method which can predict the failure of the large stiffened panel tested by Dr. Takeda to an acceptable degree of accuracy with a relatively low computational cost. This chapter starts by providing some background information regarding the previous experimental tests carried out by Dr. Takeda followed by the new modelling work from this PhD project. To facilitate a smoother large panel modelling process, it was decided to first model the two smaller stiffened coupons before attempting to model the large panel.

7.1 Background - previous experimental results

The two sets of tests carried out by Dr. Takeda involved one large centred notched panel with three hat-shaped stringers, and two smaller stiffened centre notched coupons. The coupons were cut from the pristine/undamaged areas of the large stiffened panel after it has been tested, therefore all three specimens have the same material properties and lay-up since they are from the same panel, but the geometries of the small and large specimens are dissimilar. Figure 7.1

shows photos of the large and small specimens tested for general impressions only and detailed geometries can be found in the following sections. The panel was manufactured at JAXA through Vacuum assisted Resin Transfer Moulding (VaRTM) from a bi-axial carbon Non-Crimp Fabric material. The materials of the specimens were Tenax STS-24k fibres and Nagase #6809 matrix. The layup of the specimen was $[45/\text{-}45/0/90]_{2s}$ with a skin thickness of 2 mm and flange thickness of 4 mm. Two variants of the small stiffened coupons were tested - one with a long centre notch of 70 mm and the other had a short centre notch of 17.5 mm. In total three individual specimens were tested (two small coupons and one large panel).

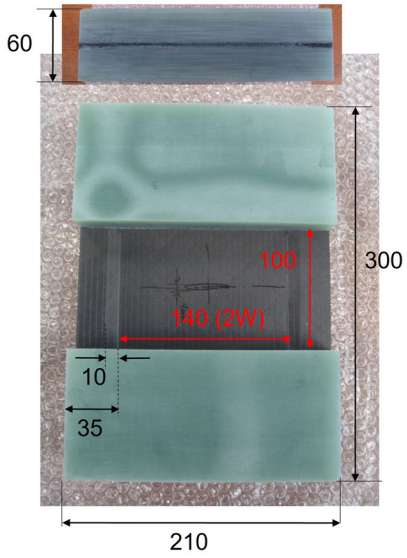

(a) Small stiffened coupon with glass fibre end tabs.

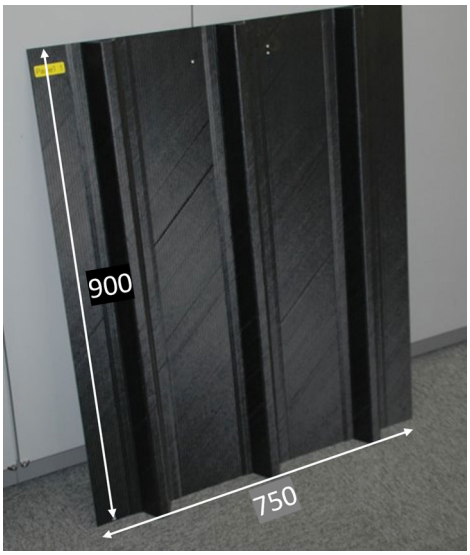

(b) Large stiffened panel with hat-shaped stringers.

Figure 7.1: Photos of the small coupon and large panel, detailed geometries can be found in the following sections.

All three sets of specimens had strain gauges installed on the surface along the crack path to measure the strain and assess the crack propagation progress. The tests were carried out in a hydraulic driven universal tensile testing machine at a loading rate of 0.5 mm/min. Figure 7.2 and 7.3 show the load-displacement curves of the small coupons and the large panel respectively.

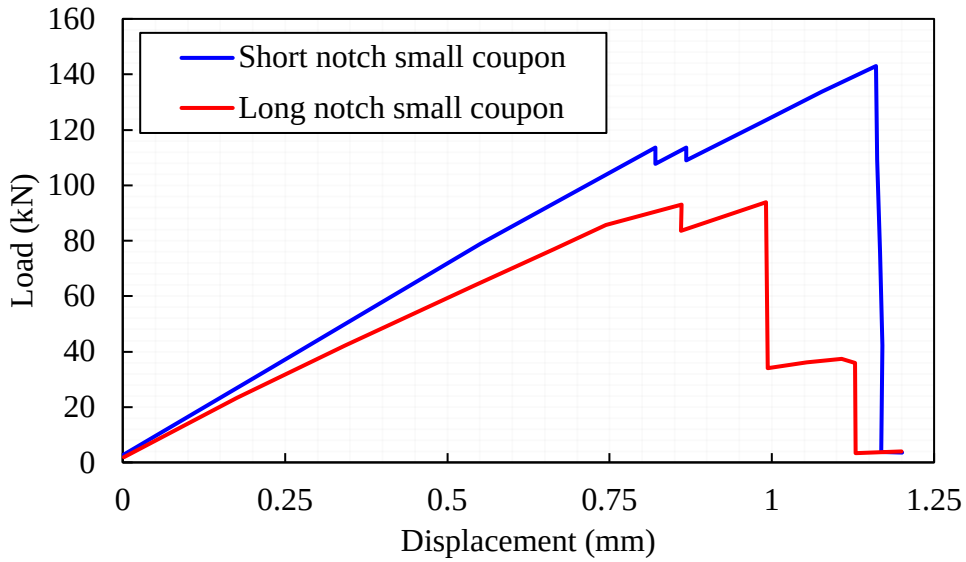

Figure 7.2: Centre-notched small stiffened coupon test data, long notch and short notch [11].

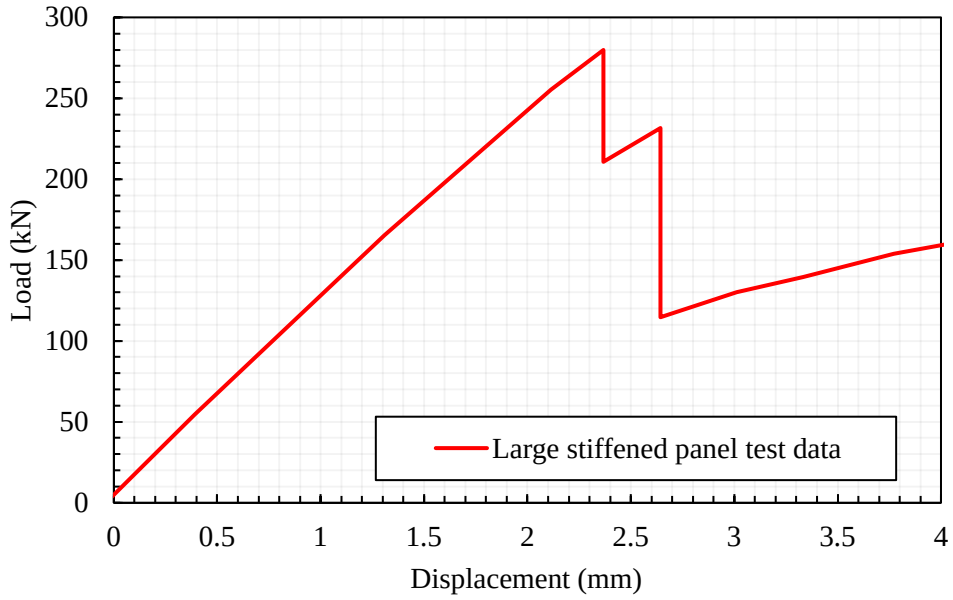

Figure 7.3: Centre-notched large stiffened panel with hat-shaped stringers test data [11].

The purpose of these photos of the specimens and load-displacement curves are to provide a high-level overview of the tests carried out by Dr. Takeda and to put the upcoming models in context for the reader. Detailed analysis and comparison of the test data are embedded in the following sections along with modelling results.

7.2 Modelling of small stiffened coupons

7.2.1 Model set-up

Two small stiffened coupons were tested, both of which had the exact same geometries and materials except the centre-notch length were different - one specimen had a long notch and the other a short notch. Figure 7.4 shows the schematic and geometry of the long-notch small stiffened coupon. The long notch coupon had a machined centre notch length of 70 mm and the short notch specimen had a machined notch length of 17.5 mm. The specimen itself is 210 mm in width and 300 mm in length, with the loading direction parallel to the specimen's long edge. The centre notch is at the geometric centroid of the specimen with the notch perpendicular to the loading direction. Two stiffeners (35 mm width) were co-cured to one side of the specimen at both edges of the specimen parallel to the loading direction and the stiffeners have got a 10 mm wide taper (the 35 mm width figure includes the taper). The specimen has four glass-fibre end-tabs bonded to the loading area as shown in the schematic in figure7.4. The thicknesses of the bonded glass-fibre end-tabs were relatively thick in comparison to the skin thickness, ensuring an even distribution of the loading shear. The machined notch had a width of 1 mm. Figure 7.5 shows a comparison of machined notches between the short and long notch specimens. For a general impression of the small stiffened coupon, please refer to figure 7.1a. The material used for the small stiffened centre-notched specimens were a Non-Crimp-Fabric (NCF) material - Tenax STS-24k fibres and Nagase #6809 matrix. The layup of the specimen is $[45/\text{-}45/0/90]_{2s}$ with a skin thickness of 2 mm and flange thickness of 4 mm. The stiffeners have the same layup as the skin. The specimen was loaded in a hydraulically driven 250 kN Instron tensile testing machine, load was applied via a pair of clamping grips to the top and bottom glass-fibre end tabs. The test was displacement controlled at 0.5 mm per minute.

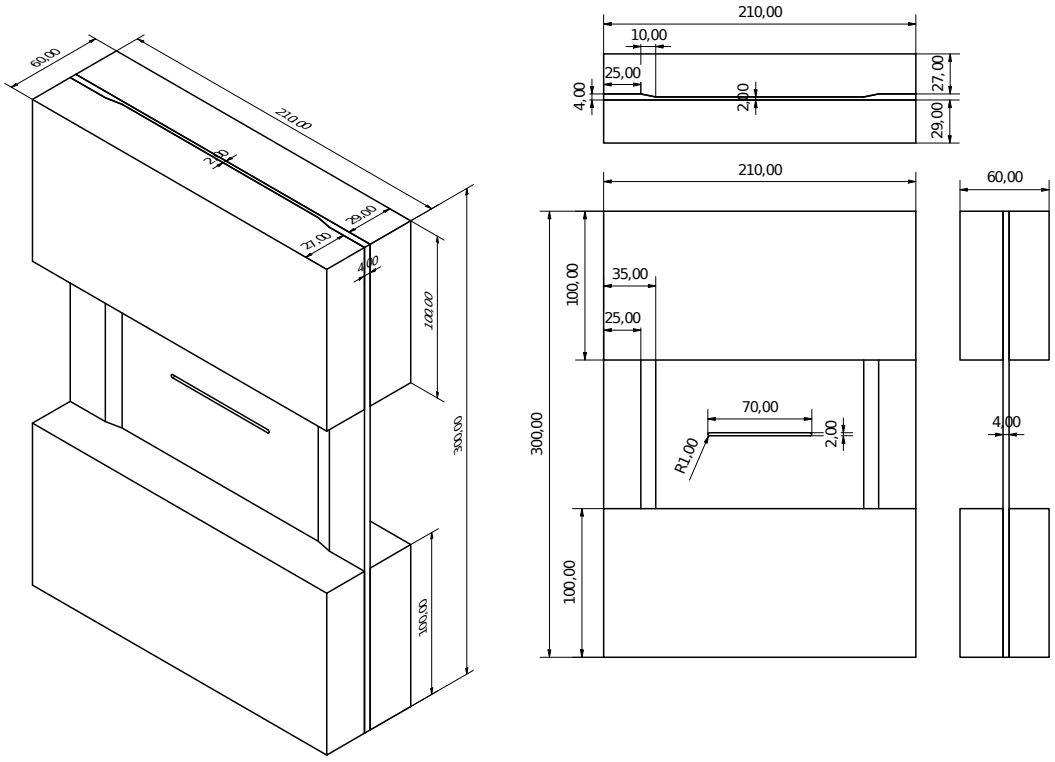

Figure 7.4: Schematic of the small stiffened coupon tested by S. Teakeda. Long notch (70 mm) specimen shown in the figure, the short notch specimen has the same geometries except the centre notch being 17.5 mm long. All dimensions in mm.

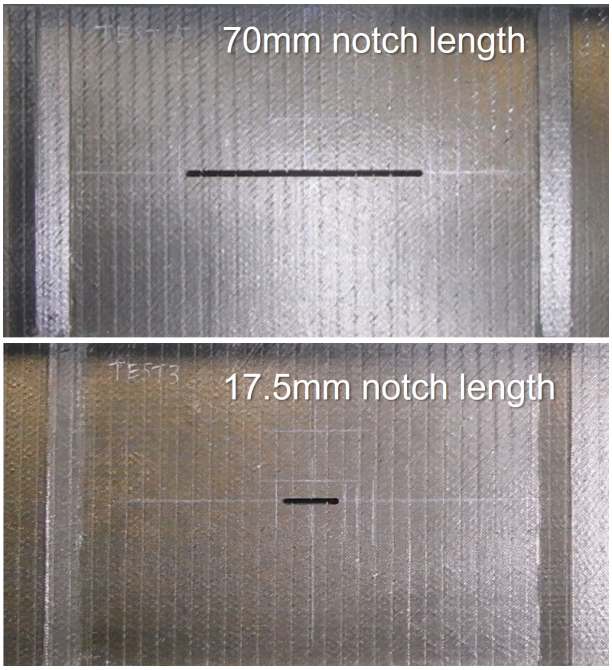

Figure 7.5: Photo comparison of the long and short notch small stiffened coupon tested by S. Takeda.

The nodal-energy VCCT model of the small stiffened coupon was mostly similar to the models presented in the previous chapter - a half model was constructed with the plane of symmetry in the loading direction passing the mid point of the horizontal notch. Figure 7.6 shows a illustration of the model. The model consists of three main components - the skin, the stringer foot and a layer of cohesive elements of thickness 0.01 mm between the skin and stringer foot to facilitate delamination. The model has a uniformly fine mesh around the crack surface with a element size of 0.5 mm and coarser mesh away from the area of interest to reduce run time. There are three elements through the thickness in the skin and the stringers (including the stringer foot taper). The model assumes the material to be quasi-isotropic with a Young's modulus of 37.9 GPa and a Poisson's ratio of 0.29 [11]. The element type used in the model is C3D8. The properties of the cohesive elements are: Nominal strength normal– 60 MPa, nominal strength 1st and 2nd shear directions – 90 MPa; G_{Ic} = 0.2 kJ/m^2 & G_{IIc} = 1 kJ/m^2. Mixed mode behaviour was set to energy based power law with power = 1. Figure 7.7 shows a close up of the mesh arrangements with a top view of the specimen.

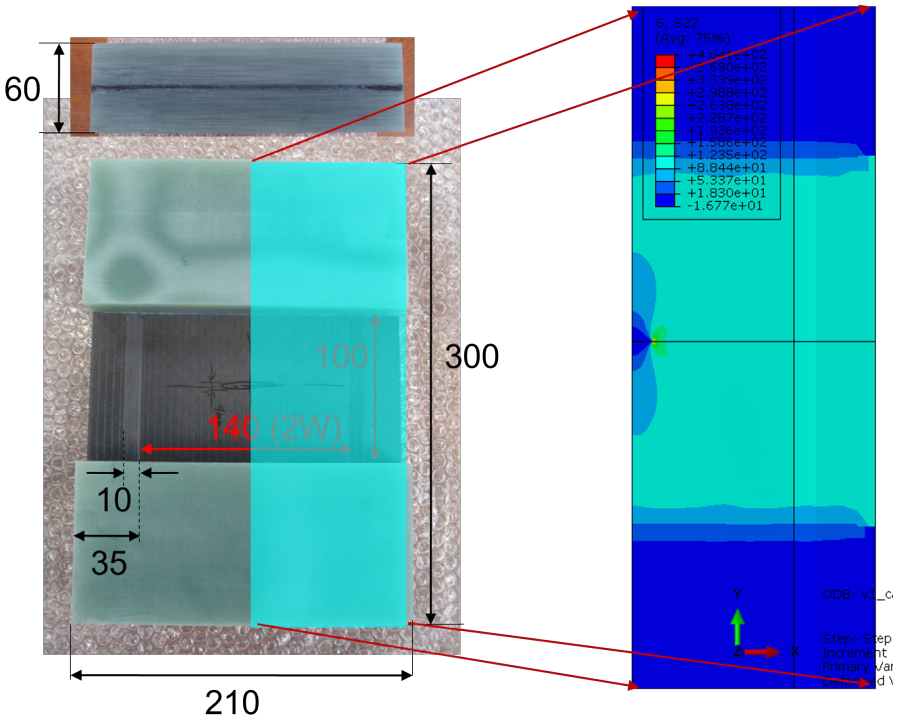

Figure 7.6: Illustration of the half-model in the context of the small stiffened coupon.

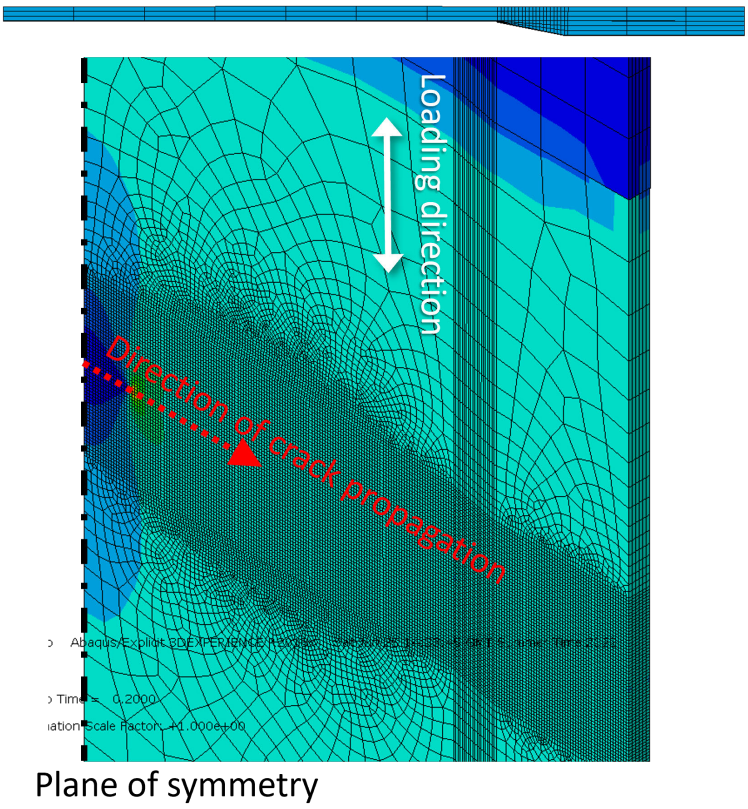

Figure 7.7: Close-up of the mesh set-up around the crack surface.

The stiffened coupon tests were carried out using a hydraulic driven universal test machine that was displacement controlled. The test machine's cross-head compressed the glass fibre end tabs top and bottom to apply the loading by shear. The loading arrangement was simplified during modelling by applying a uniform displacement boundary condition to all nodes at a given height. Figure 7.8 shows a graphical illustration of the actual loading conditions during testing and the simplified loading conditions applied within the model. Since the area of interest was relatively far away from both the end tabs, therefore the omission of the end-tabs in the model should not affect the results apart from the initial stiffness. A parametric study was carried out to assess the location of the boundary condition that would replicate the compliance provided by the glass end tabs - results suggest by applying the boundary conditions at 80 mm from machined notch the stiffness of the glass end tabs could be best replicated. Therefore for the bottom loading conditions, the layer of nodes at 80 mm below the fracture plane were applied with boundary condition U2=0, where directions 1, 2, and 3 corresponds to directions x, y, and z in figure 7.8. This bottom loading condition would represent the fixed cross-head in the test. For the top loading conditions, the layer of nodes at 80 mm above the fracture plane were applied with boundary conditions U2=2, where it represents a 2 mm displacement applied by the top cross head during testing. For the symmetry plane nodes, the boundary condition was U1=0.

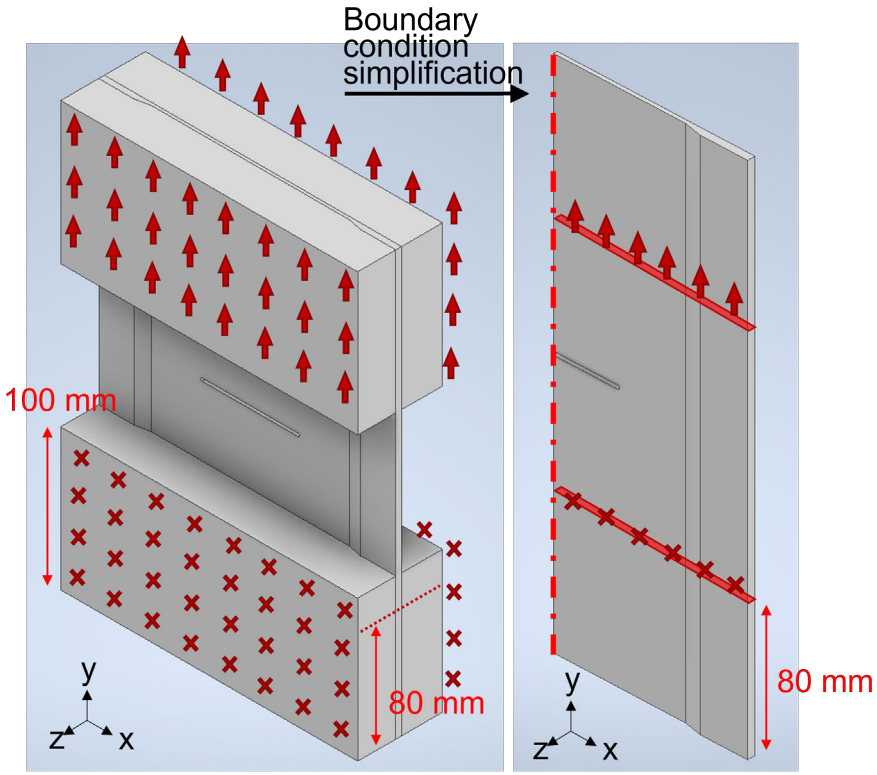

Figure 7.8: Comparison of the simplified modelling loading conditions (right) to the actual loading conditions during testing (left).

As for the machined notch, a 1 mm diamond cutter was used to machine the notch in the specimens, giving it a 0.5 mm notch tip radius. The notch in the model is a sharp notch and has no radius. This would not pose an issue as the nodal energy VCCT criterion used in the model would take the notch tip radius effect into account with the application of the R-curve. Additionally, the notch-tip radius only exerts an effect on the crack initiation phase, as a sharp crack will be naturally formed from crack propagation. Identical model set-up methods and properties were used for the 17.5 mm notch length specimen and the 70 mm notch length specimen, and they will be referred to as the short-notch specimen and long-notch specimen for the remainder of this chapter. The model was set up with the plane of crack dividing the upper and lower portions of the specimen, as shown in figure 7.6. The bottom surface in the x-z plane of the upper part and the top surface in the x-z plane of the lower part meet in the middle to form the crack surface. Surface-to-surface contact was used as the contact option for this interaction. The nodes on the crack plane that are located on the machined notch are not in contact and the nodes that are located on the ligament section were in contact via the nodal energy VCCT criterion where a critical strain energy release rate G_C is assigned to each node which in turn determines the crack propagation.

The R-curve applied to the nodal energy VCCT criterion in the model was based on the results

obtained in chapter 5 section 5.5 for the NCF material. The R-curve takes the form of a bi-linear curve, where the initial linear portion was derived from the linear regression line of the valid points of the NCF materials in section 5.5, and when the linear increasing portion reaches the last known valid point of around 91 kJ/m^2, the curve plateaus and stays constant at the maximum value. For a detailed explanation of the origin of the R-curve, please refer to section 5.5. The mesh size of the elements on the fracture plane is 0.5 mm, hence a fracture energy value is given to each node at an increment of 0.5 mm for the entire width of the specimen. The stringer foot has the same fracture energy as the skin at each corresponding location. Figure 7.9 and 7.10 show a graphical explanation of the implementation of the nodal energy VCCT criterion on the small stiffened centre-notched coupon and figure 7.11 shows the R-curve assigned to the short notch and long notch specimen.

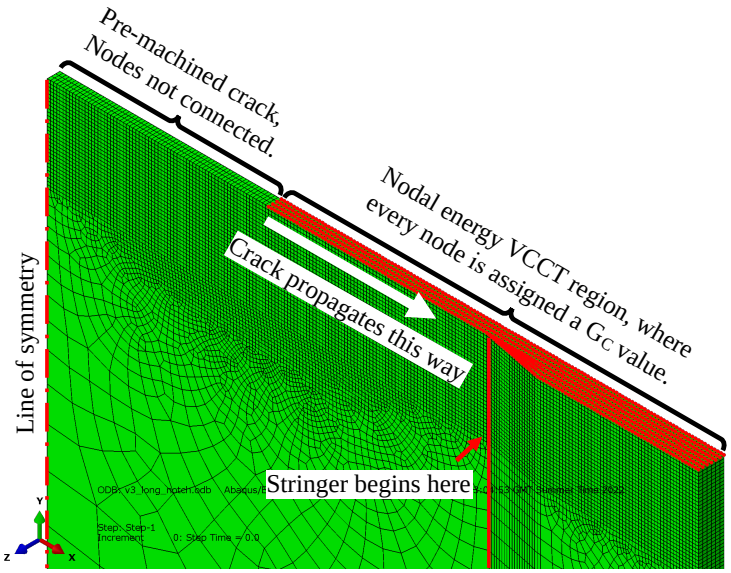

Figure 7.9: Graphical illustration of the implementation of nodal energy VCCT to the centre-notched small stiffened coupon.

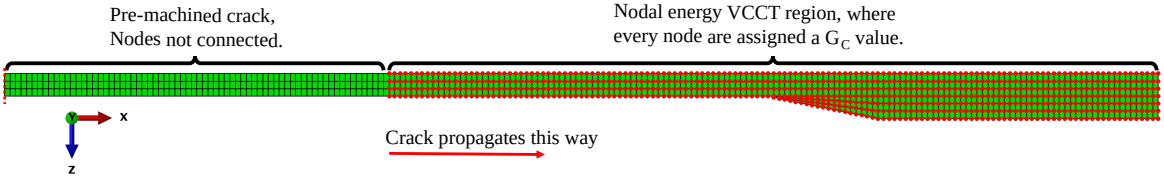

Figure 7.10: Top-down view of the implementation of nodal energy VCCT to the center-notched small stiffened coupon.

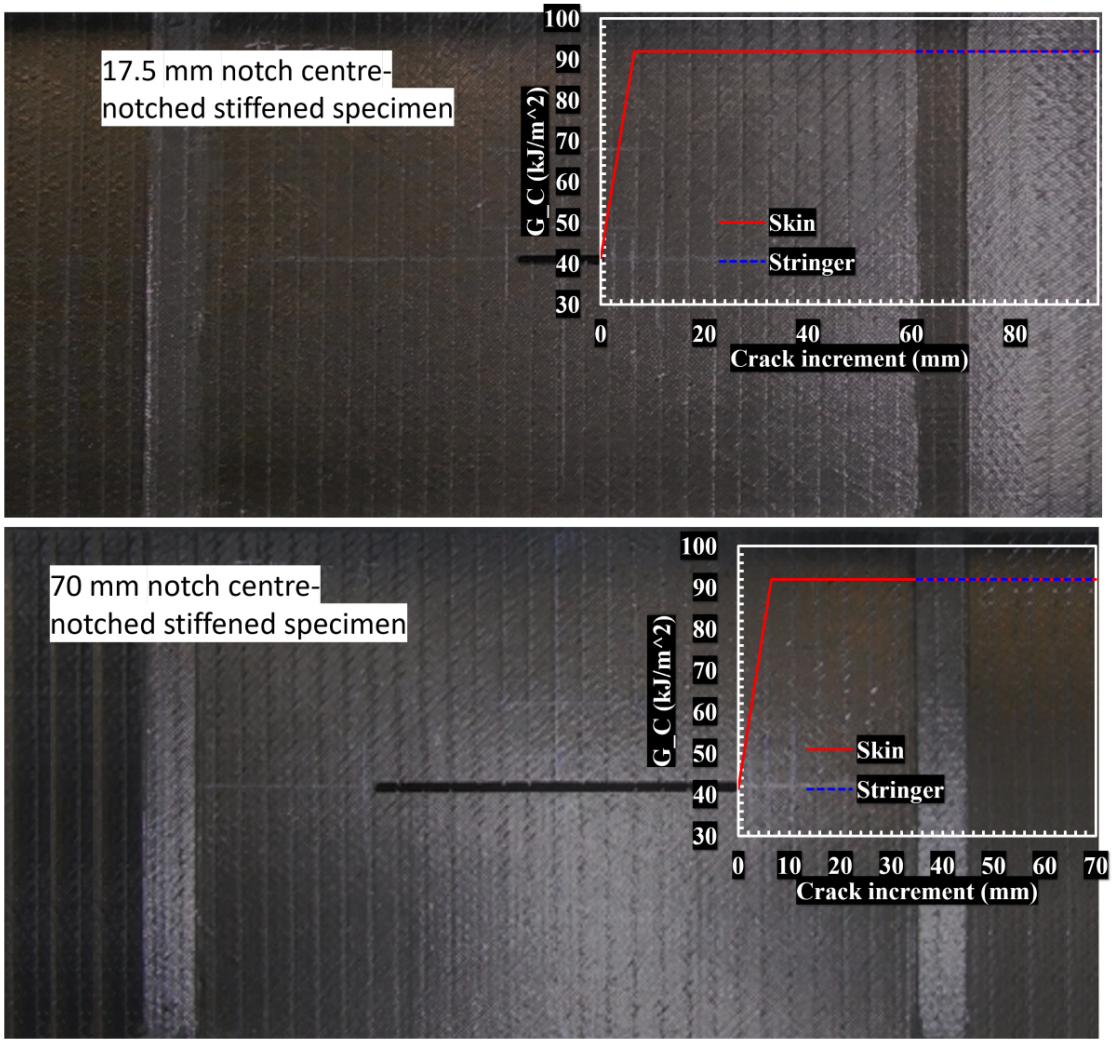

Figure 7.11: Illustration of the R-curves applied to the nodal-energy VCCT model of the short and long notched small stiffened coupons. The R-curve plateau value was 91 kJ/m^2.

7.2.2 Small stiffened coupon simulation results

With the modelling method established in the previous section, the short and long notch models were each sent for simulation. The run time for both of these models were similar at around 16 hours on a computing cluster with 28 CPU cores. The load-displacement curves of the two small stiffened coupons are shown in figure 7.12. Both the short and long centre notched coupon simulation results display a linear initial load increasing trend, with the short notch specimen having a higher initial stiffness. The long notch specimen peak load occurred at approximately 0.9 mm displacement with a peak load value of 97 kN, followed by a two-stage load drop that brought the load down to about 40 kN at 1.25 mm displacement. Whereas for the short notch specimen, the linear load increasing trend kept on its trajectory for an extra 0.3 mm displacement range - peaking at 152 kN. The peak load of the short notch specimen was approximately 57%

higher than that of the long notch specimen. The load drop that took place after reaching the peak load in the short notch specimen was of a significantly greater magnitude - dropping by approximately 72% from the peak value. Such a drastic difference in the simulated load-displacement curves of the two specimens is to be expected as their substantially different centre-notch length ought to induce different behaviours. Both models are showing the same load level (approximately 40 kN) after the load drop as the crack propagated through the skin, and the stringers were taking the load. Since the stringers are the same on both specimens therefore the same load level are found. More detailed analysis can be found in the following sections.

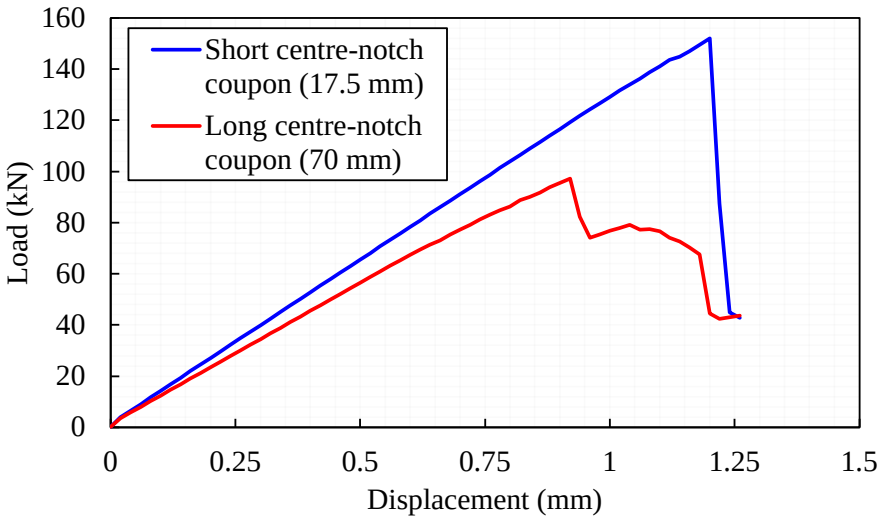

Figure 7.12: Comparison of load-displacement curves from the stiffened centre-notched coupon nodal-energy VCCT model.

7.2.3 Analysis

Having the results of the nodal energy VCCT model of the two specimens compared with each other, the logical next step is to assess the simulated results against test data. This section compares and analyses the simulated results with test data to provide a starting point for the large stiffened panel modelling presented in the following section.

7.2.3.1 Short-notch specimen simulation vs. test data

A comparison of the short-notch coupon load-displacement curves from test data and modelling results is shown in figure 7.13. The overall trend of the test data was very well captured by the model. Both the test data and modelling results are showing a very similar initial stiffness thanks to the adjusted application of the boundary conditions. Test data shows a peak load value of 143 kN compared to the peak load value of 152 kN suggested by the model - a 6% variation. The peak load value occurred at approximately 1.2 mm displacement for both results.

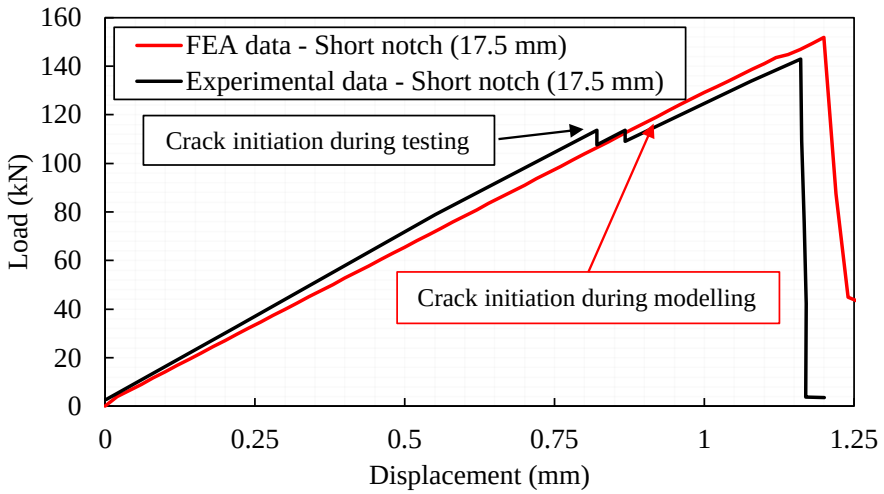

Figure 7.13: Comparison of the load-displacement curves of test data against modelling results of the short center-notched small stiffened coupon.

Test results suggest two major events took place - crack initiation and the substantial crack propagation which led to the failure of the test specimen. Crack initiation during testing took place at 0.82 mm displacement where the two minor load drops are located (black line in figure 7.13). The load subsequently kept on growing without any further crack propagation until the peak load was reached and a major crack propagation took place where the crack propagated all the way through the remaining ligament - reflected by the ultimate load-drop at 1.2 mm displacement. Turning to the modelling load-displacement curve - although there is not an obvious load drop, nonetheless crack initiation took place at approximately 0.9 mm displacement with a 116 kN load level, a very similar location compared to what the test data suggest. Following the crack initiation, a short period of stable crack propagation took place where the crack propagated by small amounts (0.5 mm) resulting in the slight non-linearity seen in the modelling load-displacement curve at around 1.1 mm displacement - followed by the peak load/ultimate failure. Additionally, the ultimate failure of the model took place at a very similar load and displacement value to the test data - demonstrating the validity of the nodal energy VCCT model for predicting failure of notched stiffened structures under tension. To further validate the nodal energy VCCT model, the test data and modelling results comparison for the long-notch specimen can be found in the following subsection.

7.2.3.2 Long-notch specimen simulation vs. test data

The failure sequence of the long-notch specimen is a little more complex compared to the short-notch specimen. Figure 7.14 shows a comparison of the load-displacement curves obtained from the test and the nodal-energy VCCT model. Simulation results and test data yield almost identical initial stiffness and peak load value. The peak load values obtained are 97.2 kN and 94.0 kN

from simulation and testing, respectively - a 3.4% discrepancy. The peak load value occurred at 0.92 mm displacement for the simulation and 0.99 mm for the test - overall they are in very good agreement.

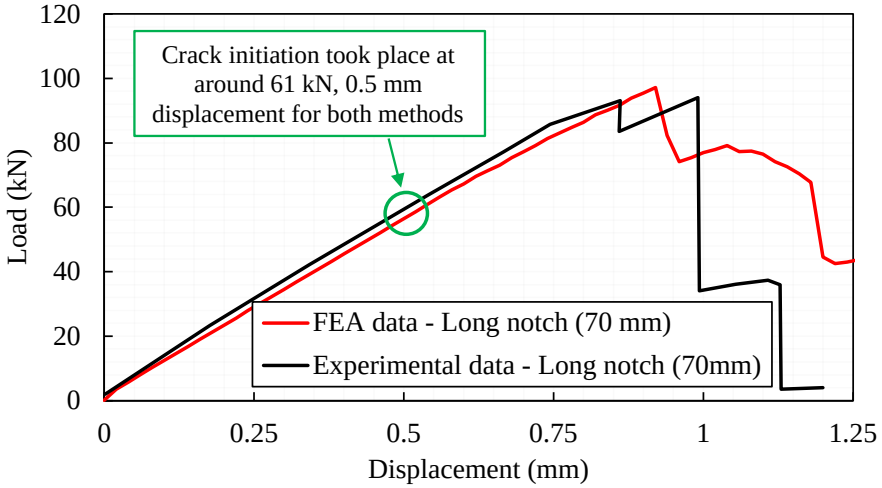

Figure 7.14: Comparison of the load-displacement curves of test data against modelling results of the long center-notched small stiffened coupon.

Unlike the short-notch specimen where a sudden failure occurred, the long-notch specimen underwent more of a staged crack propagation process, as indicated by the multiple load-drops. Multiple strain gauges were installed on the surface of the specimen during testing to measure the strain and to give an indication of crack propagation. Figure 7.15 shows the strain gauge readings for the long-notch specimen as a function of displacement. From the strain gauges the following observations can be made regarding the failure sequence during testing -

- Strain gauges 3 and 4 which are located 1.5 mm from the machined notch edge both failed at 61 kN, indicating crack initiation took place at 61 kN, 0.5 mm displacement.

- Strain gauge 5 located 5 mm away from the machined notch edge failed at approximately 89 kN, 0.8 mm displacement. This indicates crack propagation took place between 0.5 mm and 0.8 mm displacement despite no obvious plateau.

- Strain gauge 6 failed right at the peak load 0.9 mm displacement, indicating a substantial crack propagation in the skin (i.e. more than 10 mm). However, it is unclear from the strain gauge readings exactly where the crack has propagated to.

- The major load drop at 1 mm displacement saw strain gauge 7 extending significantly but did not fail. Strain gauge 7 is located on the stringer foot. Such a dramatic increase in strain in the stringer foot can only be caused by a dramatic increase in load in the stringer -

implying the crack propagated all the way through the skin during the load drop at 1 mm displacement hence transferring the load to the stringer foot.

To summarise the test results, crack initiation took place at 61 kN followed by a steady crack propagation. A substantial crack propagation took place in the skin at 0.9 mm displacement causing the first/peak load drop. It is unknown where exactly the crack was stopped at this point but it is speculated to have been arrested by the stringers based on the fact that the next load drop saw the crack propagating through the remainder of the skin. The stringer foot did not crack with the skin but failed separately later at 1.15 mm displacement.

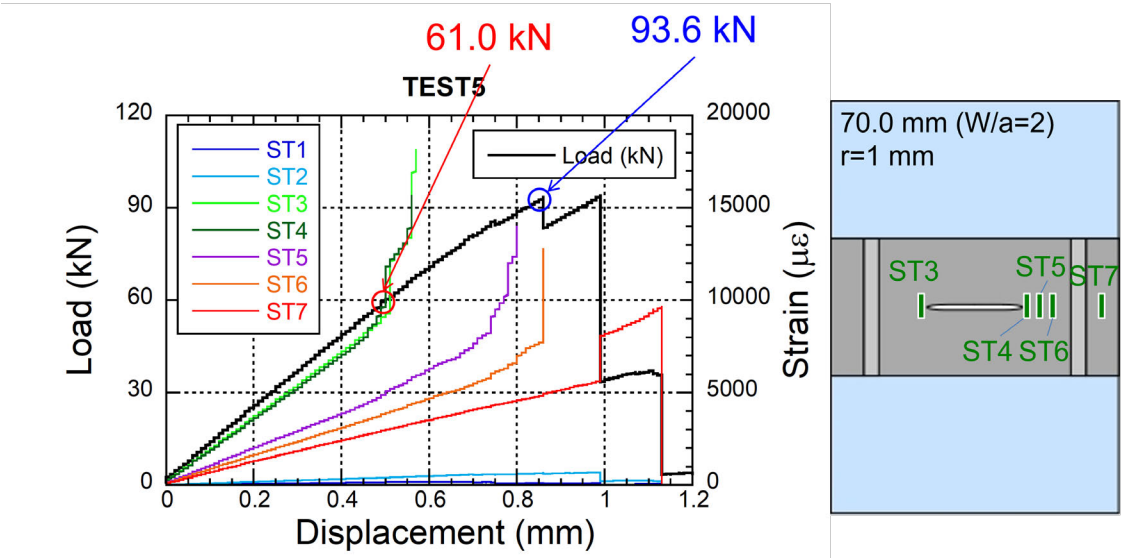

Figure 7.15: Surface strain-gauge readings and load as a function of displacement for the long-notch small stiffened coupon.

Now taking a closer inspection of the simulation results would reveal the following -

- Although not obvious on the modelling load-displacement curve, crack initiation took place at 0.55 mm displacement with a load of 62 kN. This is in a very similar range to the findings from the experimental tests - 61kN at 0.5 mm displacement.

- Following the crack initiation, three small crack propagations occurred, all three were of 2 mm crack increment. This can be correlated to strain gauge 5 (located 5 mm from the machined notch tip) failing in the test.

- Peak load was reached after the three small crack propagations and the peak load drop occurred as the crack propagated by 29 mm reaching and subsequently arrested by the stringer foot. This can be correlated to strain gauge 6 failing where the crack propagated substantially in the skin.

- As the crack was arrested by the stringer foot, load increased slightly and was followed by the crack propagating all the way through the remaining skin ligament at 1.2 mm displacement - represented in the test by the extension of strain gauge 7.

Figure 7.16 shows the screenshot of the damage status of the long-notch model at 1 mm displacement, where the crack propagated substantially, reaching and subsequently arrested by the stringer foot. The colour contour in the screenshot indicates the status of the cohesive elements between the stringer foot and the skin, where red indicates delamination/debonding and blue indicates pristine cohesive elements. From figure 7.16 it is clear that despite the crack not propagating into the stringer there is still an area of delamination - approximately 3.5 mm in length.

Figure 7.17 illustrates the relationship between crack length and displacement for both the short notch and long notch small coupon specimens. In the case of the long notch specimen, there is a strong similarity between the test data and the results obtained from FEA when it comes to crack development with respect to displacement. Conversely, for the short notch specimen, the FEA results indicate a delayed crack propagation compared to the test data. However, it's important to note that this difference doesn't necessarily imply an inherent distinction between the two sets of results. Rather, it is attributed to the sampling frequency during the test. Specifically, there were no additional data points recorded between displacements of 0.8 mm and 1.2 mm, making it unclear at which exact displacement within this range substantial crack propagation occurred.

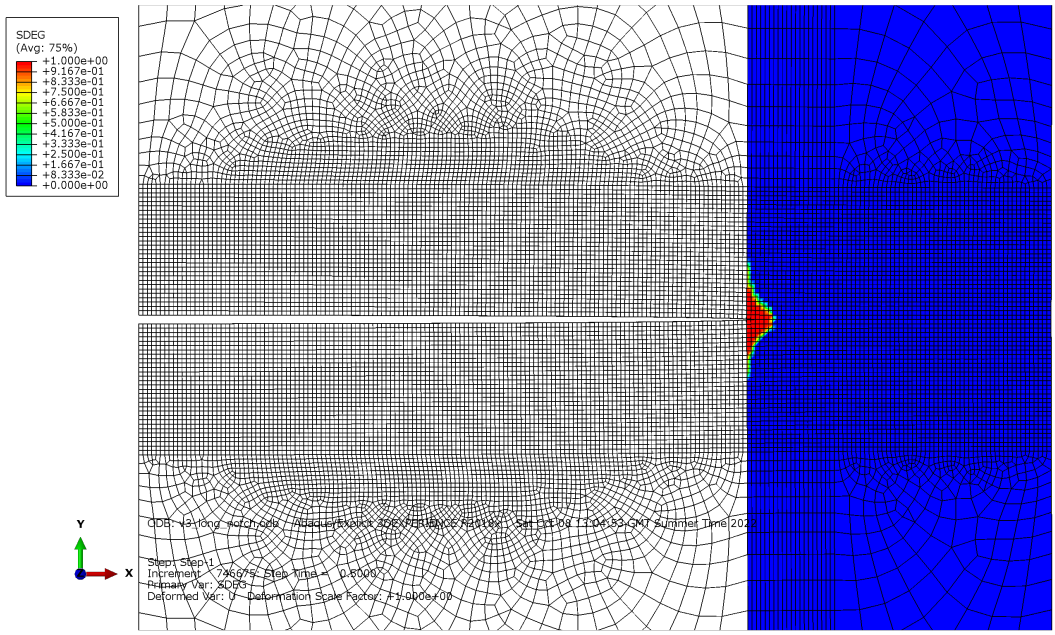

Figure 7.16: Screenshot of the damage status of the long-notch model at 1 mm displacement. Image shows the crack reaching/arrested by the stringer foot and an area of delamination.

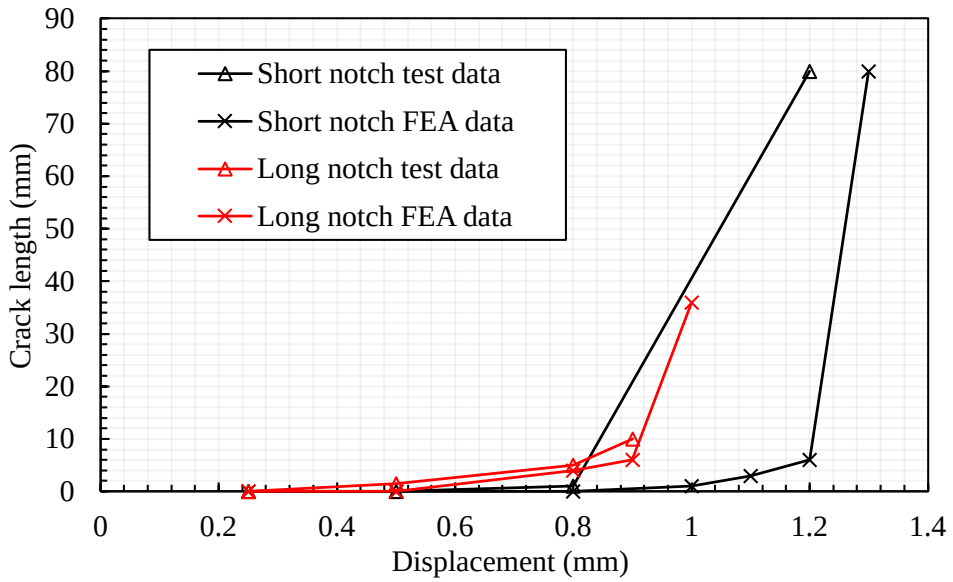

Figure 7.17: Crack length as a function of displacement for the short and long notch small coupons.

7.2.4 Conclusion for small stiffened coupon simulation

Overall the simulations of the short and long-notch stiffened coupons show a very good correlation with test results. The models employ a simple nodal-energy VCCT failure criterion to simulate the crack initiation/propagation and use cohesive elements inserted between the stringers and skin to address delamination. Both the short and long-notch models provide satisfactory accuracy against test results in the peak load department. For the short-notch specimen, crack-propagation was found to be mostly unstable and the simulation reflects this fact in addition to the resemblance of peak load. For the long-notch specimen, crack propagation was stable and was split into three stages - initiation, propagation in the skin, and the ultimate skin failure. All three stages were very well captured by the model. The crack initiation load and displacement values were almost identical between the test and the simulation. Despite these promising results, the run-time of the model was kept to an acceptable level - approximately 16 hours on a computing cluster with 28 CPU cores.

With these promising results in hand, the following section will address the ultimate goal of the PhD project - constructing a cost-effective modelling method for predicting crack propagation in a large stiffened composite panel.

7.3 Modelling of large stiffened panel with hat-shaped stringers

This section details the set-up process of the large stiffened panel model and evaluates the results by comparison with test data.

7.3.1 Model set-up

The large stiffened panel tested had an overall dimension of 750 mm by 900 mm, with the long edge in the loading direction. Three hat-shaped stringers were co-cured to one surface of the specimen running in the loading direction. The stringers are evenly spaced in the horizontal direction. Figure 7.18 shows an overall impression of the specimen with an enlarged view of the cross-section of the hat-shaped stringer. For a detailed specimen/stringer geometry, please refer to figure 7.19. A horizontal rectangular notch that runs perpendicular to the loading direction is located at the geometrical centre of the specimen. The length of the notch is 200 mm with a width of 4 mm. Figure 7.20 shows a photo of the actual specimen with a detailed view of the centre notch.

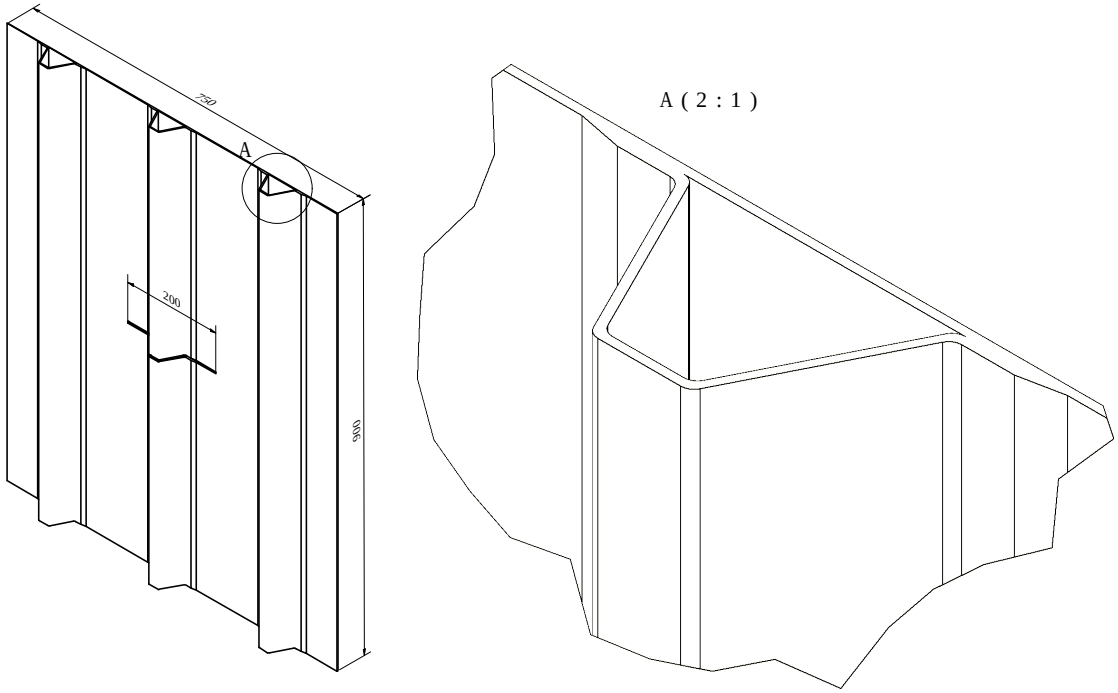

Figure 7.18: Overall impression of the large stiffened panel with three hat-shaped stringers co-cured to one side of the specimen, and a detailed view of the cross-section of the stringer. All dimensions in mm.

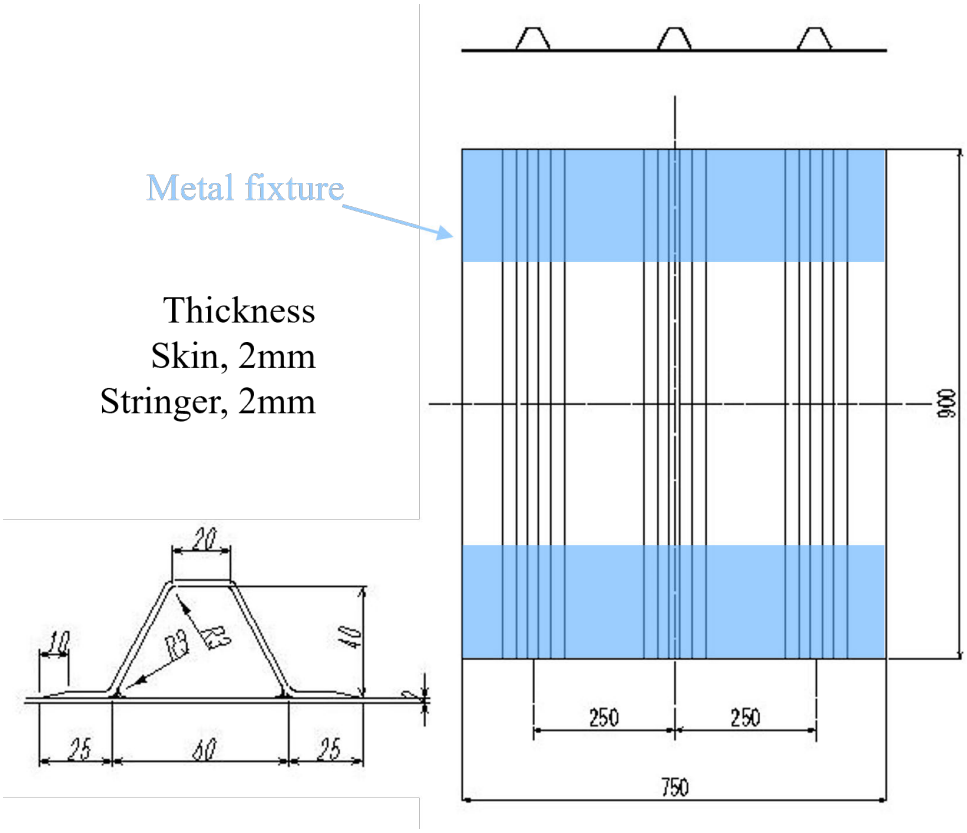

Figure 7.19: Detailed dimensions of the large stiffened panel and the hat-shaped stringers. All dimensions in mm.

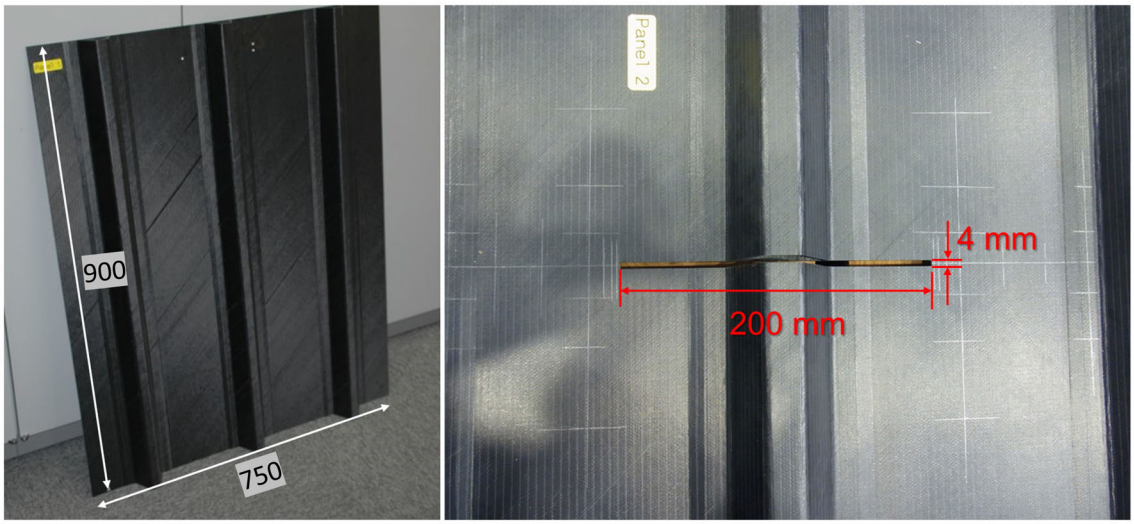

Figure 7.20: A photo of the specimen and a detailed photo of the machined centre-notch. All dimensions in mm.

The large stiffened panel specimen was made from the same NCF material as the small

stiffened coupons in the previous section - biaxial-NCF fibres (STS-24K) made by Saertex and #6809 matrix made by Nagase Chemtex Co. The specimen was made using Vacuum-assisted Resin Transfer Moulding (VaRTM). The skin and stringers are both 2 mm in thickness, each with 16 plies. The stacking sequence of the material is $[45/\text{-}45/0/90]_{2s}$. The specimen was loaded in a universal tensile testing machine via two metal fixture bolted to the upper and lower portions of the specimen to act as a shear transfer interface. The locations of the metal fixture are indicated by the blue shaded area in figure 7.19, the metal fixture are of the same width of the specimen with a height of 200 mm each. Figure 7.21 shows the specimen installed in the test jig and the arrangements of the metal fixtures.

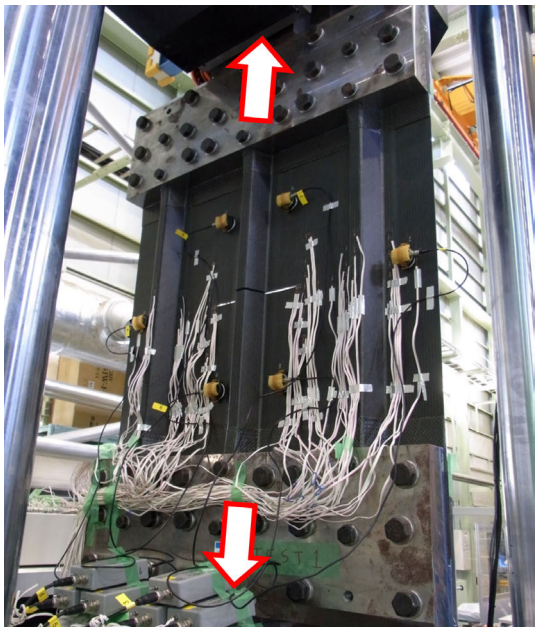

Figure 7.21: Large stiffened panel in the test jig showing the location of the metal loading fixtures. Arrows indicate loading direction.

With the test specimen and set-up established the following step is to create a model that is representative of the test. The basic philosophy of model construction is the same as the small stiffened centre-notch specimens in the previous section. The model is a half model with the symmetry plane parallel to the loading direction and orthogonal to the machined notch, as shown in figure 7.22. The model is split into two parts - upper and lower, where the two parts meet at the crack plane. Each part consists of the skin, the stringers, and the cohesive elements sandwiched between the skin and stringers to model delamination. The model contains one element through the thickness of the skin and two elements through the thickness of the stringers, as the meshing structure with two elements through the thickness in the curved stringers provide a better element aspect ratio. The thickness of the skin and stringers are both 2 mm as per the test specimen, and a layer of cohesive elements of thickness 0.01 mm was sandwiched between the skin and stringer foot. A uniform 1 mm square mesh was placed around the crack plane

with coarser mesh further away. The parametric mesh size study showed minimal difference between 0.5 mm and 1 mm element size. The large stiffened model assumes the material to be quasi-isotropic with a Young's modulus of 37.9 GPa and a Poisson's ratio of 0.29. The element type used in the model is C3D8. Figure 7.23 shows an overview of the mesh arrangements and a detailed view of the mesh arrangements around the stringer-skin interface.

A simplification was chosen when constructing the full scale panel FEA model - omitting the tapering on the stiffener feet. By neglecting the tapering, the model construction and simulation speed could be decreased. As one of the key characteristics of the novel VCCT model is its low computational cost, this was a reasonable/necessary simplification to be made. In addition, without the taper this represents a more conservative simulation which is beneficial for industrial applications. With the addition of the taper, it would promote translaminar fracture and prohibit skin/stringer debonding within the tapering region. However, the tapering width only represents a very small fraction of the specimen ligament width (2.6%), and the results would be unchanged after the tapering region. In conclusion, the tapering has been neglected to reduce the modelling constructing and simulation costs. The lack of tapering also represents a more conservative scenario which is beneficial for industrial applications. Lastly, the effect of the tapering only represents a very small portion of the crack length, and after the tapering region has finished, the results are unaffected.

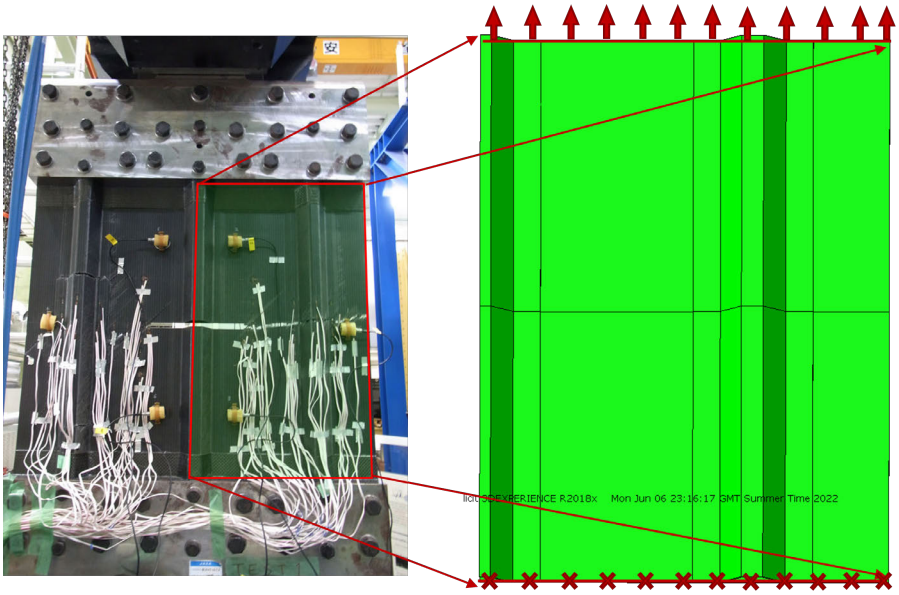

Figure 7.22: Illustration of the modelled region with respect to the whole specimen.

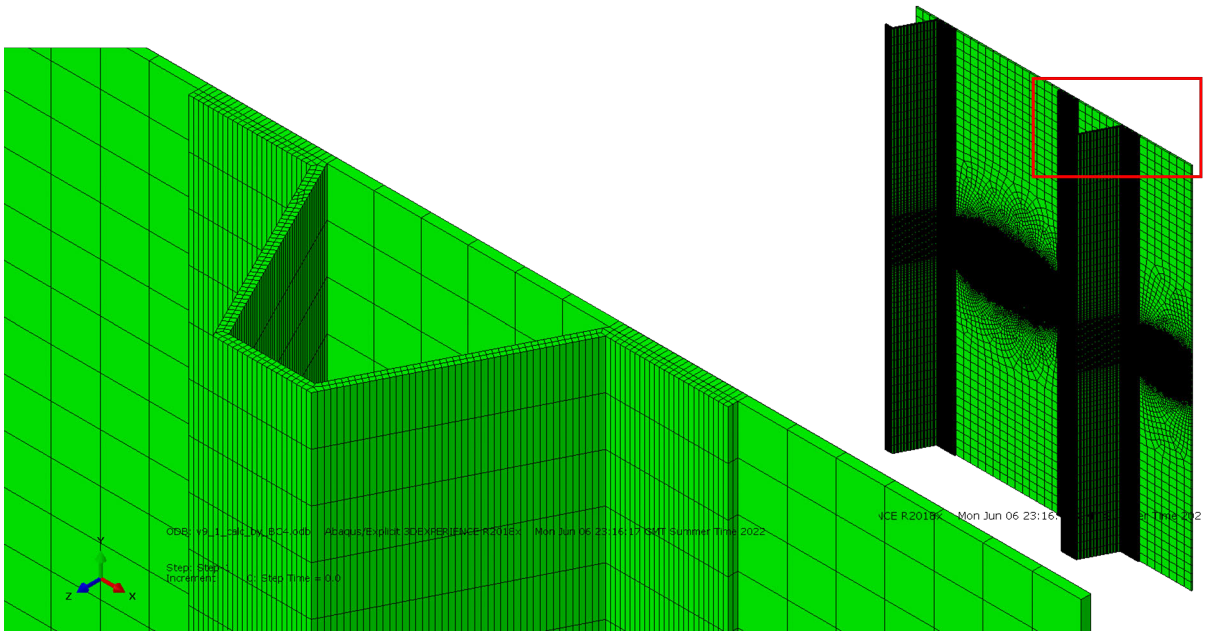

Figure 7.23: Overview of the mesh arrangements and a detailed view of the mesh around the skin-stringer interface.

For the large stiffened panel, metal fixtures were installed front and back on the specimen to act as shear transfer devices. The metal fixtures were bolted onto the specimen via 23 bolts on each end of the specimen. It has been shown in the previous section that the simplification of applying load to all nodes through the thickness at a certain height is representative of the test configuration, therefore the same assumption will be applied to the large stiffened panel. But as opposed to glass fibre end-tabs where the compliance is not negligible, it could be argued the metal fixture used has significantly higher stiffness and can be omitted. Therefore satisfactory results can be obtained by applying load to all nodes through the thickness at the ends of the metal fixtures, as shown in figure 7.22. The boundary conditions applied to the top and bottom plane of nodes are as follows -

Table 7.1: Boundary conditions applied to the top and bottom loading nodes.

Top	U2 = 4 mm
Bottom	U2 = 0

where U denotes displacement and the direction 1, 2, and 3 denotes x, y and z as per figure 7.23.

Similar to the previous models, the large stiffened panel model employs nodal energy VCCT as the failure criterion for crack propagation and uses cohesive elements to facilitate the potential delamination/debonding between stringer foot and skin. The nodal energy VCCT criterion was applied in the same manner as in the small stiffened coupon model in the previous section, where all nodes through the thickness at a given crack increment are assigned a critical strain energy

release rate G_C value for the whole of the ligament. The same R-curve, derived from the compact tension and ESET NCF specimen tests in chapter 4, was applied to both the small stiffened coupon models in the previous section and the current large stiffened panel model. Figure 7.24 shows the nodal energy VCCT criterion with respect to the large stiffened panel and figure 7.25 shows the R-curve overlayed on top of the large stiffened panel. The model was setup in explicit mode, the run time on a 28 CPUs computing node was approximately 17 hours.

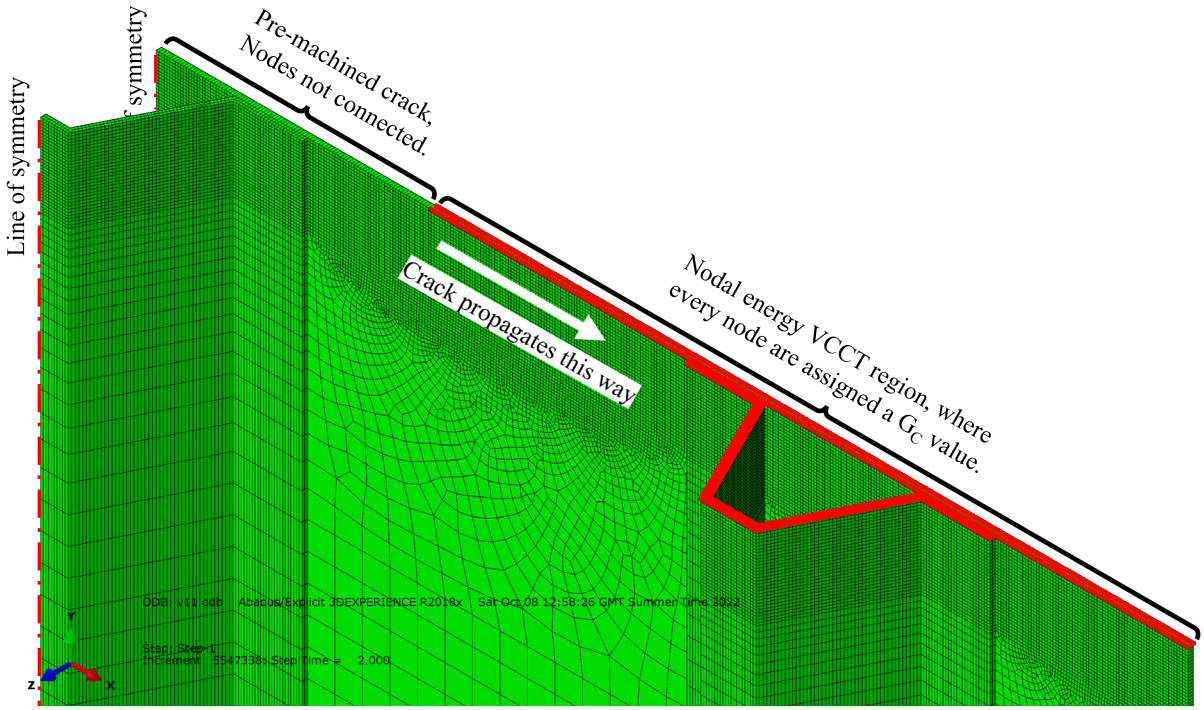

Figure 7.24: Illustration of nodal energy VCCT criterion with respect to the large stiffened panel.

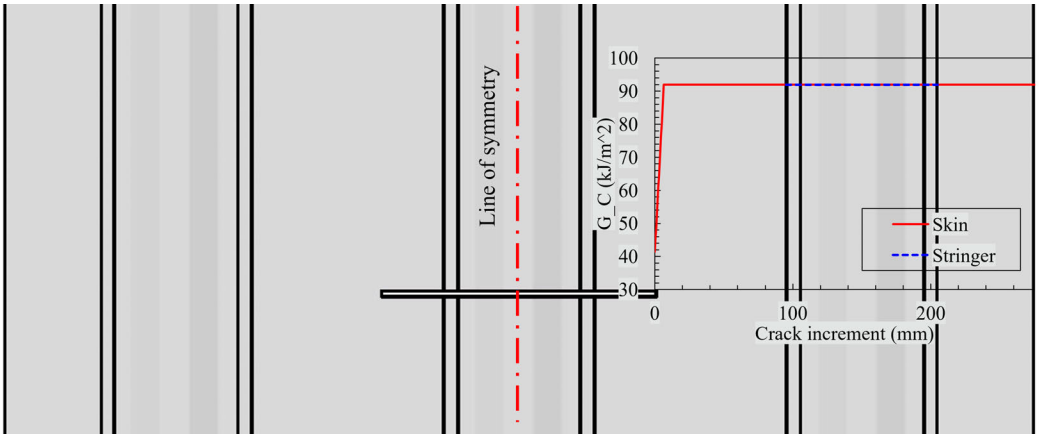

Figure 7.25: R-curve applied overlayed on top of the large stiffened panel.

7.3.2 Large stiffened panel simulation results

With the large stiffened panel model set-up established in the previous section, the model was sent for simulation. Figure 7.26 shows the load-displacement curve produced by the model. Simulation results suggest there are in total three distinct load-drops taking place for the large stiffened panel, with the second load-drop being the drop from the peak load. From the start, a linear load-displacement relationship is found, where the load increased linearly to approximately 220 kN followed by a small/first load-drop. The first load-drop was of a magnitude of approximately 20 kN. Following the first load-drop, the load kept on increasing to the peak load - reaching 260 kN at 2.3 mm displacement, followed by the second load-drop. Having had a second load drop, the load yet again kept on increasing, but by about 15 kN this time and the third load took place. The third load drop was by far the largest in magnitude - where the load dropped by close to 100 kN from 230 kN to 130 kN. After the third load drop, the load kept on increasing until 4 mm displacement where the model was terminated at the 4 mm displacement mark .

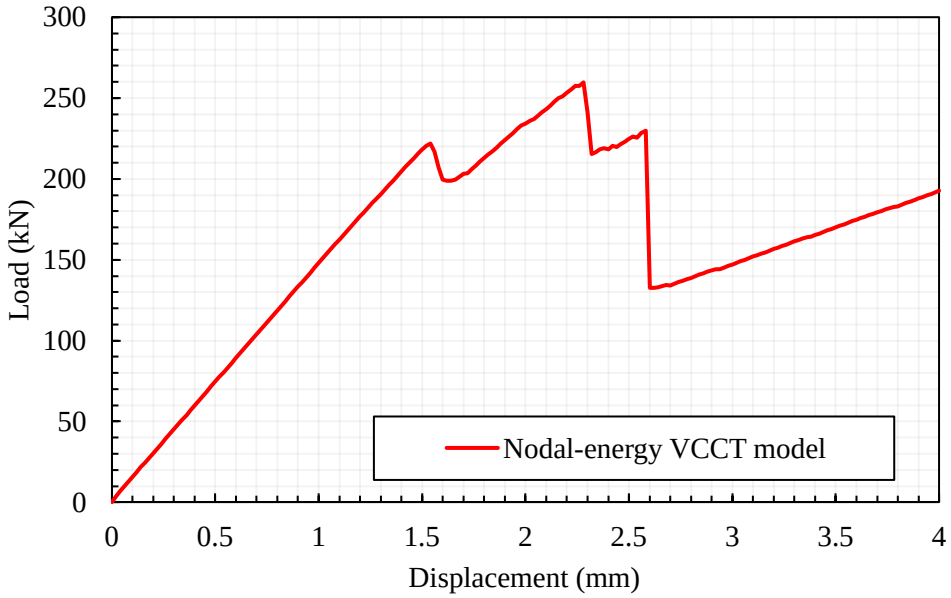

Figure 7.26: Load-displacement curve produced by the large stiffened panel nodal-energy VCCT model.

7.3.3 Analysis

To better understand the damage mechanism and to assess the validity of the nodal energy model, this section will analyse the sequence of events that took place during the test and the results revealed by the model. The comparison between the test and the model provides an indication of the validity of the model and determines whether it satisfies the original requirements - a cost-effective modelling method for predicting fracture in large notched stiffened composite panels.

Figure 7.27 shows a comparison of the load-displacement curves obtained from the test and the model. Overall there is a very good agreement between the two, especially where the two load drops in the test load-displacement curves were very well captured by the model. The test data load-displacement curve showed a linear increasing trend right till the peak load at 282 kN, 2.4 mm displacement. The first load drop in the test took the load from its peak value of 282 kN to 220 kN, a 62 kN load drop. Following the peak load drop the load kept on increasing, similar to the model, for about 20 kN and a major load drop of magnitude 117 kN took place which saw the load dropping to 114 kN - 40% of the peak value. After the major load drop, the load kept on increasing till 4 mm displacement.

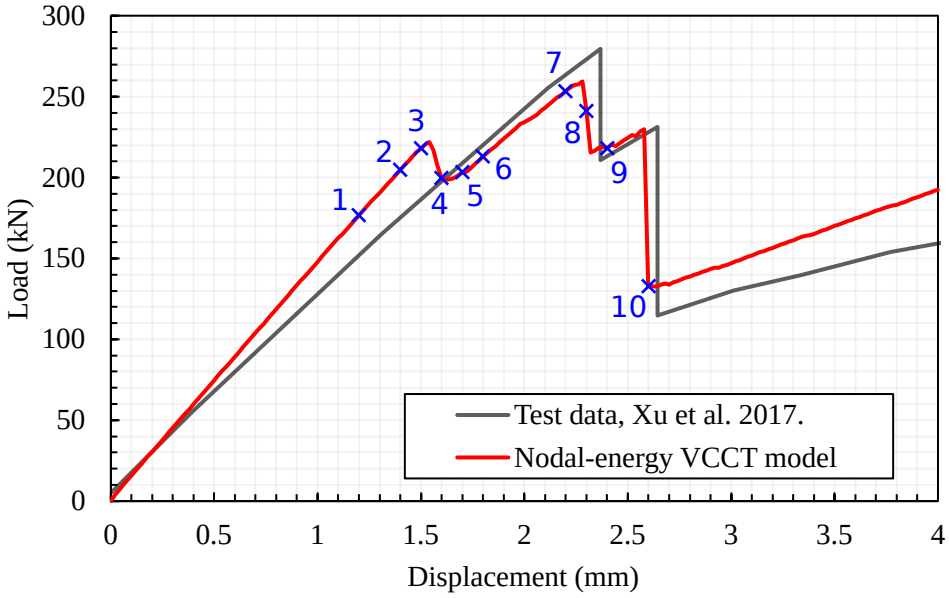

Figure 7.27: A comparison of load-displacement curves obtained from test and the nodal-energy VCCT model. The blue markings with numbering are key events marked on the modelling load-displacement curve.

To better capture the failure events sequence, the test specimen had a number of strain gauges installed on the stringer side of the specimen, as indicated in figure 7.21 and 7.22 where the white cables were each connected to a surface-mounted strain gauge. The purpose of the strain gauges was to measure the strain at different locations of the specimen and to assess the crack propagation status. Figure 7.28 shows the locations and numbering of the strain gauges.

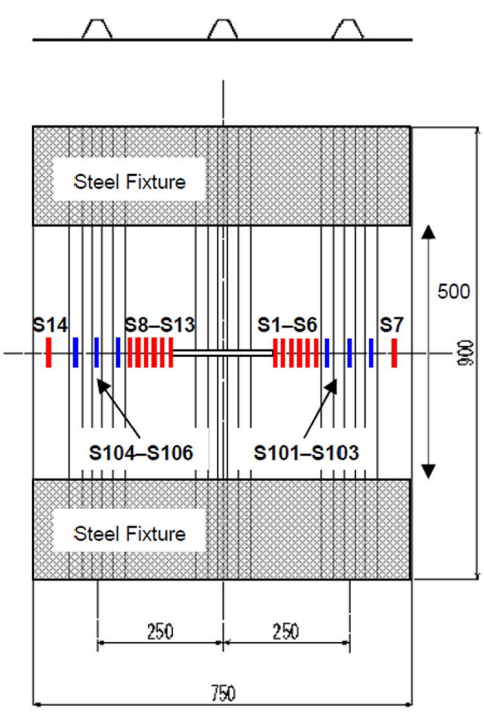

Gage No.	Location
S1(S8)	1.5 mm from notch tip
S2(S9)	5 mm from notch tip
S3(S10)	10 mm from notch tip
S4(S11)	20 mm from notch tip
S5(S12)	50 mm from notch tip
S6(S13)	80 mm from notch tip
S7(S14)	35mm from skin edge
S101 (S104)	On foot near to notch
S102(S105)	On top of stringer
S103(S106)	On foot far to notch

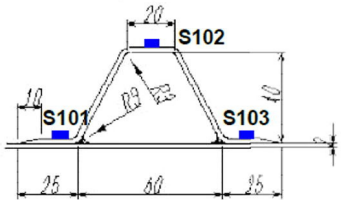

Figure 7.28: Locations and numbering of the strain gauges installed on the large stiffened test panel, [11].

With the help of these strain gauges, the crack propagation sequence could be captured. In summary, the key events during the test were -

- Strain gauges 1 and 8, located 1.5 mm from either side of the machined notched, failed at 182 kN and 197 kN respectively. However, it was reported that the average fracture process zone of this material is approximately 3.1 mm [11], therefore strain gauges 1 and 8 would fail during the development of the fracture process zone as they are both 1.5 mm away from the notch tip.

- Strain gauge 9 located 5 mm from the machined notch-tip, failed at 235 kN. This indicates crack initiation (with a fully developed fracture process zone) took place at 235 kN.

- The peak load drop at 282 kN saw the breakage of multiple strain gauges (S3 to S6), indicating the occurrence of a substantial crack propagation from 10 mm crack increment to 80 mm crack increment. At this point, the crack reaches and propagates past the inner stringer foot (each hat-shaped stringer were connected to the skin via two stringer feet - inner and outer). The inner stringer foot cracked with the skin at this point, the outer stringer foot was still intact.

- The second load drop which took place at 231 kN 2.6 mm displacement saw the breakage of the outer stringer foot and the crack propagating through the remaining ligament till

the edge of the specimen. Strain gauge number 7 fails, which is located on the skin on the outer side of the stringer near to the edge of the specimen. At this point, the right side of the panel, skin and stringer, has failed completely, all load are taken by the left side of the specimen where the skin was still intact.

Turning to the modelling load-displacement curve. To simplify the analysis process, the modelling load-displacement curve in figure 7.27 has ten blue markings to indicate the locations of the key events. The key events being -

- At key event location 1, crack initiation took place at 1.2 mm displacement with a load of 176 kN. The crack initiation point corresponds to the first point on the input R-curve which is 41 kJ/m^2.
- At key event location 2, the crack propagated slightly to 4 mm crack increment. Load and displacement at location 2 were 204 kN and 1.4 mm respectively.
- At key event location 3, the crack propagated further to approximately 7 mm crack increment. At this point the input R-curve has already reached its plateau value of 91 kJ/m^2. From here on the input critical strain energy release rate stays constant at the plateau value. For location 3, the load and displacement are 218 kN and 1.5 mm respectively.
- A substantial crack propagation took place at 1.6 mm displacement, hence the load drop seen between key event locations 3 and 4. After the load drop at location 4, the crack has propagated a long way reaching about 20 mm away from the inner stringer foot.
- Crack propagated even further between key event locations 4 and 5. At location 5 the crack stopped 2mm before the inner stringer feet.
- At location 6 the crack reaches the inner stringer foot, debonding area is about 4 mm in width in the cracking direction. Due to the crack-arresting effect of the stringers, the load keeps on increasing after location 6.
- At key event location 7, crack in the skin propagated 40% underneath the inner stringer foot width, the delamination area under the inner stringer foot is approx. 60% in the width direction. At location 7, the load and displacement are 253 kN and 2.2 mm respectively.
- At key event location 8, the crack in the skin has propagated past the inner stringer foot completely. The inner stringer foot has debonded from the skin. The crack in the skin stopped at 15mm in front of the outer stringer foot. At location 8, the load and displacement are 240 kN and 2.3 mm respectively.
- At key event location 9, the crack propagated underneath the outer stringer foot for 7 mm. The load drop seen between locations 8 and 9 is due to the crack propagating underneath the

outer stringer foot. Delamination area underneath the outer stringer foot is substantial but the outer stringer foot is still holding on and the crack has not penetrated the outer stringer foot yet. At location 9, the load and displacement are 240 kN and 2.3 mm respectively.

- At key event location 10, the crack propagated all the way underneath the outer stringer foot and the remaining skin ligament. Hence the huge load drop. At this point the stringer was still intact hence the load did not drop to zero.

Figure 7.29 shows the crack length as a function of displacement for the test data and FEA results. The crack length values obtained are similar between the test data and the FEA results, however there is a difference in the displacement. Such disagreement in displacement is understandable as the specimen itself is physically very large (approximately 1 m by 1 m) and any slight inaccuracies when measuring the displacement would cause the 1 mm difference seen. In addition, the specimen was loaded by multiple bolts which has a finite contact area to distribute the load, but the model takes a simplified version of loading on a plane of nodes. The simplification in loading conditions could have caused the difference in stiffness hence the displacement difference seen.

In short, the modelling results contain four key stages - crack initiation at 176kN; a substantial crack propagation in the skin and the subsequent crack arrest by the inner stringer foot between key event locations 3 to 6; crack propagating past the inner stringer foot during the load drop at 2.3 mm displacement, and crack propagating the outer stringer foot and the remainder ligament at 2.6 mm displacement. Figure 7.30 shows the delamination status at key event location 7 where the crack was arrested by the inner stringer foot and the boundary of delamination is approximately 8 mm in front of the crack front. The clear evidence of crack arresting effect shown here indicates the peak load achieved by the large panel is attributable to the stringers as opposed to the R-curve effect.

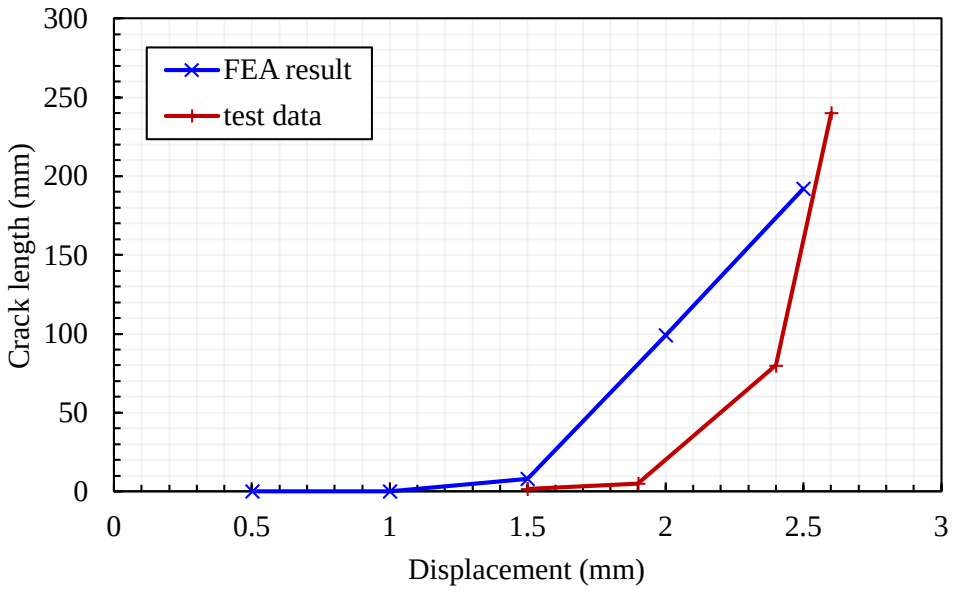

Figure 7.29: Crack length as a function of displacement for FEA and test results.

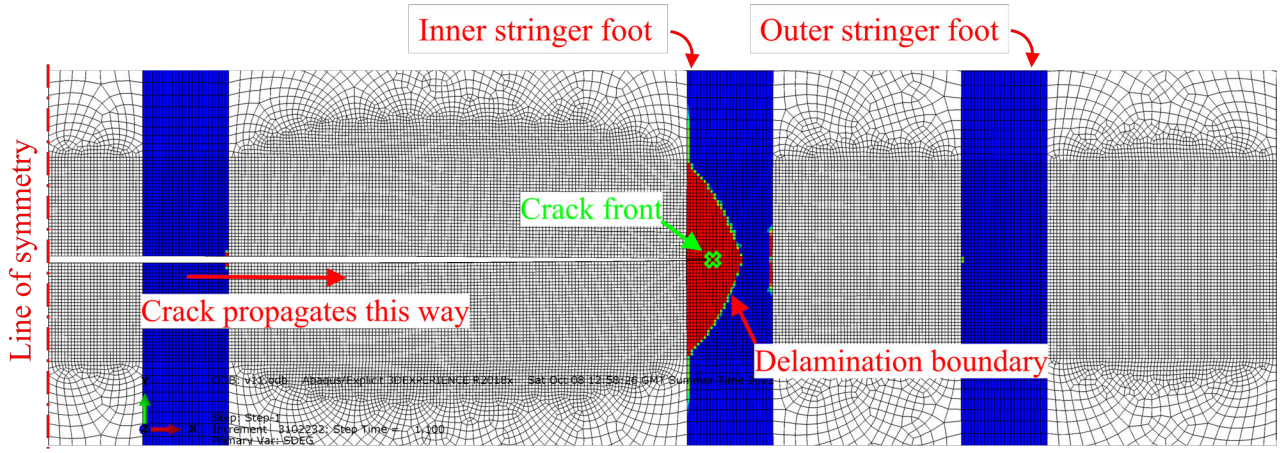

Figure 7.30: Delamination status at key event location 7 from the large stiffened panel simulation showing delamination boundary at 8 mm in front of the crack front. Red elements indicate delaminated cohesive elements and blue indicates pristine. At this point in time the crack was in the skin only, no evidence of the crack in the stringer foot.

7.4 Discussion

Overall a good correlation can be found between the large stiffened panel test data and nodal-energy VCCT modelling result. Both sources show a similar crack initiation load in the region of 180 kN. The nodal-energy VCCT model does not distinguish between fracture process zone development and crack propagation, therefore the crack initiation in the model was determined by the movement of the stress concentration created by the crack front. To compare like for like,

strain gauges 1 and 8 in the test panel which are 1.5 mm away front either side of the notch tip both failed in the region of 180 to 190 kN, which is in very good agreement with the model. Furthermore, the peak load drop in the test was induced by the crack propagating substantially in the skin reaching and surpassing the inner stringer foot. This damage sequence was reflected in the model by means of two load drops located between key events 3 to 4 and key events 7 to 8, where the crack propagated substantially in the skin between locations 3 to 4 and surpassed the inner stringer foot between 7 to 8. In addition, the large load drop seen at 2.6 mm displacement in both sources corresponds to the crack propagating past the outer stringer foot through the remaining ligament with almost identical load values - 230 kN.

The obvious disagreement between the test data and modelling results is that the modelling load-displacement curve shows one extra load drop at 1.6 mm displacement, whereas the test data does not. It should be noted that despite the test data not displaying a load drop, the underlying crack propagation (i.e. substantial crack propagation in the skin where the crack reaches the inner stringer foot) still took place. Based on the available strain gauge data, it could be concluded that the crack has reached and surpassed the inner stringer foot after the peak load drop at 2.4 mm displacement. However, it is unclear whether this crack propagation took place instantly at the moment of the load drop or prior. In addition, as with any experimental test, imperfections in the test specimen and outside factors cause uncertainties in the results. In the case of the large stiffened panel, the crack propagated asymmetrically between the two sides of the specimen where on the left side the crack propagated above the crack plane, as shown in figure 7.31. Such asymmetrical crack propagation causes the crack path to be not directly underneath the surface bonded strain gauges, rendering their results less accurate. Furthermore, the test data also displayed a gradual change in the initial stiffness which was likely to have been caused by the testing jig compliance and the local deformation at the loading holes. Hence despite the additional load drop in the modelling data, it could still be considered to be a good correlation as the model is capable to capture all the main damage events at approximately the correct locations.

Figure 7.31: Picture of the failed large-panel showing asymmetric crack propagation between two sides.

A previous study by Xu et al. [11] related the initial fracture propagation of full-scale stiffened composite panels to that of small stiffened coupons and scaled-down Over-height Compact Tension (OCT) specimens, where it was demonstrated that translaminar fracture energy is the key link to bridging the dimension gap between large and small specimens. This chapter has taken this further and demonstrated the capability of predicting the behaviour of large stiffened panels using the R-curve obtained from significantly smaller coupons.

7.5 Conclusion

To conclude, this chapter demonstrated the setup process and the results of the nodal-energy VCCT model for two small stiffened coupons and a large stiffened panel. The models employ a simple nodal-energy VCCT failure criterion to simulate the crack initiation/propagation and use cohesive elements inserted between the stringers and skin to address delamination. Two centre-notch small stiffened coupons were modelled and the results were compared with existing test data. Both the long and short-notch specimen models showed a promising correlation with test data, where the unstable crack propagation in the short-notch specimen and the stable crack propagation in the long-notch specimen were well captured by the model. The crack initiation

load and displacement values were almost identical between the test and the simulation.

For the large stiffened panel with hat-shaped stringers, a nodal-energy VCCT model was constructed and results show a high resemblance to test data. The crack initiation value, peak load, and crack arresting effect of the stringers were all well captured by the model. Despite the accuracy of the model, the run time could be kept relatively low at 16 hours on a 28-core CPU computing cluster. It has been demonstrated that the novel approach of employing VCCT in conjunction with cohesive elements is capable of producing accurate results at a relatively low cost. The results produced by the nodal energy VCCT model proves to be satisfactory while being slightly conservative. The characteristics of being conservative and low cost are two vital requirements for industrial use.

CHAPTER 8

CONCLUSIONS

8.1 Thesis conclusions

The aim of this PhD was to construct a cost-effective modelling method to predict the fracture of large notched stiffened composite panels. To achieve this an extensive literature review was carried out which looked into and analysed the recent experimental and numerical research in the field of composite fracture, followed by six distinct yet intertwined pieces of research each reported in a self-contained chapter. The conclusions of these chapters are as follows -

In chapter 3, two sets of stiffened Over-height Compact Tension (OCT) specimens were manufactured and tested to characterise the fracture process in notched stiffened composite coupons. The two sets of stiffened OCT specimens had different stringer thickness - one set had 2 mm stringers while the other set had 0.5 mm thick stringers. The stiffened OCT specimens were manufactured from Hexcel IM7/8552 prep-reg with a quasi-isotropic layup, 32 plies with a nominal skin thickness of 4 mm. A comprehensive set of results were collected with these two sets of stiffened OCT specimens with varying stringer thicknesses. Results show that both sets of specimens, thin and thick stringers, exhibited delamination to some extent, while only the 0.5 mm stringer specimens experienced stringer breakage. The extent of delamination was greater on the 2 mm stringer specimens compared to the 0.5 mm stringer specimens. When a crack in the skin encounters a stringer, one of two things happens - either delamination propagation only or delamination/debonding along with stringer breakage. Exactly which happens is dependent on the relative strength of the stringer and the interface. The load-carrying capability of the skin decreases as fracture propagates through it, therefore an increasing amount of load is transferred to the stringers. When the stringer is relatively strong or of sufficient thickness, it can withstand more of the load that is transferred, in a way facilitating crack propagation in the skin. On the

other hand, when the stringer is not of sufficient strength or thickness, it fails in tension as the load gets transferred to it, reducing the overall load-carrying capability of the specimen. Such tensile failure is what was observed in the failed 0.5 mm stringer specimens.

In chapter 4, two sets of experimental tests were carried out using a Non-Crimp Fabric (NCF) material provided by the Japan Aerospace Exploration Agency (JAXA). One set consists of testing a number of compact tension specimens, while the other set consists of two eccentrically loaded single-edge-notch tension (ESET) specimens with in-situ CT scan. From the compact tension specimen set, one uninterrupted test and four interrupted tests were carried out. The interrupted test specimens were prepared and subsequently CT scanned. Test results and CT scan images suggest a positive correlation between crack length and displacement but the rate of increase of crack length slows down as displacement increases. No obvious delamination was found in the CT scan images of the interrupted compact tension specimens. R-curves for the compact tension specimens were calculated using the ASTM E399 data reduction method. Only the first two points on the R-curve were in the valid range, reaching 91 kJ/m^2. For the ESET specimens, two tests were carried out with in-situ CT scan. In-situ CT scanning a R-curve to be produced from each specimen on its own, hence two R-curves were produced for the ESET specimens. Data shows an increase in the R-curve of the ESET specimens with no evidence of a plateau yet. The maximum valid value of fracture energy was 48.5 kJ/m^2. While these two sets of tests provided an insight to the damage morphology and the corresponding R-curves, the R-curves obtained here were still not long enough - there was still no evidence of the location of the plateau. Therefore another set of tests was conducted to try to see the R-curve plateau.

In chapter 5, a set of large compact tension specimens manufactured from thin-ply materials were tested with the aim of obtaining a longer R-curve. Five of the thin-ply compact tension specimens were tested, all of which showed a very straight and neat crack surface with no signs of delamination and splitting. CT scans were carried out to verify the hypothesis that the surface crack increment is the same as the effective crack increment for this thin-ply specimen, and results suggest the hypothesis is true. The effect of notch tip radius was assessed by testing a specimen with the notch tip sharpened by tapping a razor blade, whereas for other specimens the notch tip had a radius of 0.5 mm. The specimen with the sharp notch yielded a lower peak load and a smaller magnitude for the initial load drop, with the rest of the load-displacement curve being very similar to specimens with machined notch tips. The thin-ply compact tension specimen showed an increasing R-curve to approximately 55 mm crack increment with no sign of a plateau. Towards the end of the chapter, a comparison was made between the different R-curves obtained from this chapter and the previous chapter, with all specimens' R-curves showing an increasing trend within the valid range. For the JAXA NCF material - which is the material of concern for this PhD thesis, a linearly increasing R-curve was assumed before crack increment 8.1 mm, after which the R-curve stays constant at the plateau value.

In chapter 6, the development of the VCCT model was covered in detail, from a basic VCCT

model with very basic geometries and a single critical strain energy release rate value to a nodal energy VCCT model that can predict translaminar fracture in stiffened OCT specimens using R-curves. Two sets of specimens were simulated using the nodal-energy VCCT model - stiffened OCT specimens with 0.5 mm and 2 mm stringers. For both sets of specimens, a strong correlation was discovered between the numerical forecasts and test findings. The newly developed nodal energy VCCT model produced results that were marginally conservative compared to tests, but at the same time were very computationally efficient - two characteristics that would make it extremely appealing for industrial applications. It was concluded that with an accurate R-curve, a model that utilises the nodal energy VCCT failure criterion and the cohesive zone elements would be capable of producing accurate predictions. With the nodal energy VCCT model established for the stiffened OCT specimen, the next step would be to apply this technique to the large stiffened panel, achieving the initial ultimate goal of this PhD project.

In the final chapter, the knowledge and data obtained from the previous chapters were put to use in achieving the ultimate goal of the PhD thesis - constructing a cost-effective modelling method for predicting fracture in large notched stiffened composite panels. To achieve this goal, two small stiffened coupons of the same material as the large panel was firstly modelled using the nodal-energy VCCT method developed in the previous chapter. The two small stiffened coupons were centre notched with two stringer feet co-cured to one side of the specimen, they differ in the centre notch length with one having a long notch of 70 mm and the other one with a short notch of 17.5 mm. The models for the long and short notch specimens both displayed a positive correlation with test results, with the models successfully simulating both the unstable crack propagation in the short notch specimen and the stable fracture propagation in the long notch specimen. Between the test and the simulation, the fracture initiation load and displacement values were remarkably similar. Having the behaviour of the small coupons of the same material accurately predicted, a nodal-energy VCCT model was built for the large stiffened panel with hat-shaped stringers, and the load-displacement curve predicted by the model closely match test data. The model accurately predicted the crack initiation value, peak load, and crack arresting effect of the stringers. Despite the model's precision, a 28-core CPU processing cluster allowed for a run duration that was only 16 hours, a significant reduction compared to some high fidelity models [14]. It has been demonstrated that the R-curve obtained from the small coupon tests is sufficient for accurate large panel predictions.

Overall it could be argued that this PhD project has been a great success in that much valuable test data have been collected and the initial goal has been well achieved. The three batches of experimental tests carried out (stiffened OCT, NCF compact tension and ESET specimens, and thin-ply compact tension) each provided some very interesting findings in their unique way. It was concluded that the stringers fail in tension as opposed to fracture. The newly developed nodal energy VCCT model demonstrates its outstanding capability to predict the fracture process of a large stiffened composite panel while being extremely computationally efficient, bridging the gap

between small test coupons to large panels.

8.2 Potential future work

This thesis has investigated a range of different topics and achieved the initial goal, leaving certain works for the future due to time constraints. These are summarised below:

- Full R-curve. Despite extensive tests carried out during this project, the full R-curve still has not been determined, and the location of the R-curve plateau needs further confirmation. This would require some more tests to be carried out to have a definitive answer - namely a larger compact tension specimen with non thin-pliy materials.

- The relationship between ply thickness, fracture toughness and the R-curve. The initial aim of testing the thin-ply compact tension specimens was to induce a longer R-curve such that the location of the plateau would be revealed. However, the thin-ply results did not reveal the locations of the plateau. This suggests that not only does the ply thickness have an effect on the initial fracture toughness, but influences the whole R-curve . This ply thickness effect on the R-curve needs to be investigated in the future.

- The effect of the stringer attachment method on the skin-crack/stringer interaction. All the tests carried out in this thesis have stringers co-cured to the skin, meaning that the stringers and the skin were cured simultaneously. It is suspected that the interaction between the skin-crack and the stringer would differ significantly if the stringers were attached to the skin via other methods such as secondary bonding. This is an important area as stringers are often not co-cured to the skin in engineering structures.

- The environmental effects on translaminar toughness. All tests carried out in this thesis have been at room temperature. The effect of hot and wet conditions on translaminar fracture would be very interesting area of research as engineering structures are often found operating at non-ideal conditions.

- Developing a FEA model capable of predicting the fracture behaviour of large stiffened panels under compression would be another critical area for future research. This would require a large amount of research since compression is fundamentally different from tension, but equally critical to engineering applications.

BIBLIOGRAPHY

[1] C. Kassapoglou, *Modeling the effect of damage in composite structures: simplified approaches*.
John Wiley & Sons, 2015.

[2] M. De Moura and A. De Morais, "Equivalent crack based analyses of enf and els tests," *Engineering Fracture Mechanics*, vol. 75, no. 9, pp. 2584–2596, 2008.

[3] J. Li, E. W. Lee, T. K. OBrien, and S. M. Lee, "Evaluation of the edge crack torsion (ect) test for mode 3 interlaminar fracture toughness of laminated composites," in *ASTM Symposium on Composite Materials: Testing and Design*, no. NASA-TM-110264, 1996.

[4] W. F. Gale and T. C. Totemeier, *Smithells metals reference book*.
Elsevier, 2003.

[5] A. Ismail, A. Ariffin, S. Abdullah, and M. Ghazali, "Stress intensity factors for surface cracks in round bar under single and combined loadings," *Meccanica*, vol. 47, no. 5, pp. 1141–1156, 2012.

[6] T. J. Rawlings, K. T. Carpenter, and J. P. Parmigiani, "Experimental specimen for classification of matrix compression damage in carbon fiber reinforced polymers," in *ASME 2018 International Mechanical Engineering Congress and Exposition*, pp. V001T03A026–V001T03A026, American Society of Mechanical Engineers, 2018.

[7] R. Krueger, "Virtual crack closure technique: History, approach, and applications," *Appl. Mech. Rev.*, vol. 57, no. 2, pp. 109–143, 2004.

[8] X. Xu, M. R. Wisnom, Y. Mahadik, and S. R. Hallett, "Scaling of fracture response in overheight compact tension tests," *Composites Part A: Applied Science and Manufacturing*, vol. 69, pp. 40–48, 2015.

[9] X. Xu, S.-i. Takeda, and M. R. Wisnom, "Investigation of fracture process zone development in quasi-isotropic carbon/epoxy laminates using in situ and ex situ x-ray computed tomography," *Composites Part A: Applied Science and Manufacturing*, vol. 166, p. 107395, 2023.

[10] X. Sun, S.-i. Takeda, M. R. Wisnom, and X. Xu, "In situ characterization of trans-laminar fracture toughness using x-ray computed tomography," *Composites Communications*, vol. 21, p. 100408, 2020.

[11] X. Xu, S.-i. Takeda, Y. Aoki, S. R. Hallett, and M. R. Wisnom, "Predicting notched tensile strength of full-scale composite structures from small coupons using fracture mechanics," *Composite Structures*, vol. 180, pp. 386–394, 2017.

[12] "Test method for linear-elastic plane-strain fracture toughness KIc of metallic materials."

[13] X. Xu, X. Sun, and M. R. Wisnom, "Initial r-curves for trans-laminar fracture of quasi-isotropic carbon/epoxy laminates from specimens with increasing size," *Composites Science and Technology*, p. 109077, 2021.

[14] X. Xu, M. R. Wisnom, and S. R. Hallett, "Deducing the r-curve for trans-laminar fracture from a virtual over-height compact tension (oct) test," *Composites Part A: Applied Science and Manufacturing*, vol. 118, pp. 162–170, 2019.

[15] S. Pinho, L. Iannucci, and P. Robinson, "Formulation and implementation of decohesion elements in an explicit finite element code," *Composites Part A: Applied science and manufacturing*, vol. 37, no. 5, pp. 778–789, 2006.

[16] S. Pinho, L. Iannucci, and P. Robinson, "Physically based failure models and criteria for laminated fibre-reinforced composites with emphasis on fibre kinking. part ii: Fe implementation," *Composites Part A: Applied Science and Manufacturing*, vol. 37, no. 5, pp. 766–777, 2006.

[17] N. Moës and T. Belytschko, "Extended finite element method for cohesive crack growth," *Engineering fracture mechanics*, vol. 69, no. 7, pp. 813–833, 2002.

[18] T. K. O'Brien, "Interlaminar fracture toughness: the long and winding road to standardization," *Composites Part B: Engineering*, vol. 29, no. 1, pp. 57–62, 1998.

[19] N. Sela and O. Ishai, "Interlaminar fracture toughness and toughening of laminated composite materials: a review," *Composites*, vol. 20, no. 5, pp. 423–435, 1989.

[20] A. De Morais, C. Rebelo, P. De Castro, A. Marques, and P. Davies, "Interlaminar fracture studies in portugal: past, present and future," *Fatigue & Fracture of Engineering Materials & Structures*, vol. 27, no. 9, pp. 767–773, 2004.

[21] A. Szekrényes, "Overview on the experimental investigations of the fracture toughness in composite materials," 2002.

[22] A. Internat., *Standard test method for mode I interlaminar fracture toughness of unidirectional fiber-reinforced polymer matrix composites*.
ASTM Internat., 2007.

[23] A. Internat., "Standard test method for mixed mode i-mode ii interlaminar fracture toughness of unidirectional fiber reinforced polymer matrix composites," 2022.

[24] A. J. Vinciquerra, B. D. Davidson, J. R. Schaff, and S. L. Smith, "Determination of the mode ii fatigue delamination toughness of laminated composites," *Journal of Reinforced plastics and composites*, vol. 21, no. 7, pp. 663–677, 2002.

[25] P. Davies, "Introduction to delamination fracture of continuous fibre composites," 2001.

[26] E. E. Gdoutos, *Fracture mechanics: an introduction*, vol. 263.
Springer Nature, 2020.

[27] D. Broek, *Elementary engineering fracture mechanics*.
Springer Science & Business Media, 1982.

[28] M. Wisnom, "The role of delamination in failure of fibre-reinforced composites," *Philosophical Transactions of the Royal Society A: Mathematical, Physical and Engineering Sciences*, vol. 370, no. 1965, pp. 1850–1870, 2012.

[29] T. Gordon, X. Xu, L. Kawashita, M. R. Wisnom, S. R. Hallett, and B. C. Kim, "Delamination suppression in tapered unidirectional laminates with multiple ply drops using a tape scarfing technique," *Composites Part A: Applied Science and Manufacturing*, vol. 150, p. 106627, 2021.

[30] P. Davies, B. Blackman, and A. Brunner, "Mode ii delamination," in *European Structural Integrity Society*, vol. 28, pp. 307–333, Elsevier, 2001.

[31] A. Brunner, B. Blackman, and P. Davies, "Mode i delamination," in *European Structural Integrity Society*, vol. 28, pp. 277–305, Elsevier, 2001.

[32] H. F. Bueckner, "The propagation of cracks and the energy of elastic deformation," *Transactions of the American Society of Mechanical Engineers*, vol. 80, no. 6, pp. 1225–1229, 1958.

[33] A. AC09036782, *Standard test method for mode I interlaminar fracture toughness of unidirectional fiber-reinforced polymer matrix composites*.
ASTM Internat., 2007.

[34] C. A. Wood and W. L. Bradley, "Determination of the effect of seawater on the interfacial strength of an interlayer e-glass/graphite/epoxy composite by in situ observation of

transverse cracking in an environmental sem," *Composites science and Technology*, vol. 57, no. 8, pp. 1033–1043, 1997.

[35] R. Talreja, "Damage and failure of composite materials," in *Advanced Theories for Deformation, Damage and Failure in Materials*, pp. 235–280, Springer, 2023.

[36] R. Gutkin, M. Laffan, S. Pinho, P. Robinson, and P. Curtis, "Modelling the r-curve effect and its specimen-dependence," *International Journal of Solids and Structures*, vol. 48, no. 11-12, pp. 1767–1777, 2011.

[37] S. Pinho, P. Robinson, and L. Iannucci, "Developing a four point bend specimen to measure the mode i intralaminar fracture toughness of unidirectional laminated composites," *Composites Science and Technology*, vol. 69, no. 7-8, pp. 1303–1309, 2009.

[38] D. Hull and Y. B. Shi, "Damage mechanism characterization in composite damage tolerance investigations," *Composite Structures*, vol. 23, no. 2, pp. 99–120, 1993.

[39] R. Krueger, M. K. Cvitkovich, T. K. O'Brien, and P. J. Minguet, "Testing and analysis of composite skin/stringer debonding under multi-axial loading," *Journal of composite Materials*, vol. 34, no. 15, pp. 1263–1300, 2000.

[40] S. R. Hallett, B. G. Green, W.-G. Jiang, K. H. Cheung, and M. R. Wisnom, "The open hole tensile test: a challenge for virtual testing of composites," *International Journal of Fracture*, vol. 158, no. 2, pp. 169–181, 2009.

[41] M. W. Czabaj and J. G. Ratcliffe, "Comparison of intralaminar and interlaminar mode i fracture toughnesses of a unidirectional im7/8552 carbon/epoxy composite," *Composites Science and Technology*, vol. 89, pp. 15–23, 2013.

[42] J. Laffan, S. Pinho, P. Robinson, and A. McMillan, "Translaminar fracture toughness testing of composites: A review," *Polymer Testing*, vol. 31, no. 3, pp. 481–489, 2012.

[43] A. C. Garg, "Intralaminar and interlaminar fracture in graphite/epoxy laminates," *Engineering fracture mechanics*, vol. 23, no. 4, pp. 719–733, 1986.

[44] S. M. Lee, "A comparison of fracture toughness of matrix controlled failure modes: delamination and transverse cracking," *Journal of composite materials*, vol. 20, no. 2, pp. 185–196, 1986.

[45] M. Iwamoto, Q.-Q. Ni, T. Fujiwara, and K. Kurashiki, "Intralaminar fracture mechanism in unidirectional cfrp composites: Part i: Intralaminar toughness and ae characteristics," *Engineering Fracture Mechanics*, vol. 64, no. 6, pp. 721–745, 1999.

[46] R. Truss, P. Hine, and R. Duckett, "Interlaminar and intralaminar fracture toughness of uniaxial continuous and discontinuous carbon fibre/epoxy composites," *Composites Part A: Applied Science and Manufacturing*, vol. 28, no. 7, pp. 627–636, 1997.

[47] K. D. Cowley and P. W. Beaumont, "The interlaminar and intralaminar fracture toughness of carbon-fibre/polymer composites: The effect of temperature," *Composites science and technology*, vol. 57, no. 11, pp. 1433–1444, 1997.

[48] B. F. Sørensen and T. K. Jacobsen, "Large-scale bridging in composites: R-curves and bridging laws," *Composites Part A: Applied Science and Manufacturing*, vol. 29, no. 11, pp. 1443–1451, 1998.

[49] S. Jose, R. R. Kumar, M. Jana, and G. V. Rao, "Intralaminar fracture toughness of a cross-ply laminate and its constituent sub-laminates," *Composites Science and Technology*, vol. 61, no. 8, pp. 1115–1122, 2001.

[50] M. De Moura, R. D. Campilho, A. Amaro, and P. Reis, "Interlaminar and intralaminar fracture characterization of composites under mode i loading," *Composite Structures*, vol. 92, no. 1, pp. 144–149, 2010.

[51] F. Macedo, A. Pereira, and A. de Morais, "Mixed bending-tension (mbt) test for mode i interlaminar and intralaminar fracture," *Composites science and technology*, vol. 72, no. 9, pp. 1049–1055, 2012.

[52] S. Parhizgar, L. W. Zachary, and C. Sun, "Application of the principles of linear fracture mechanics to the composite materials," *International Journal of Fracture*, vol. 20, no. 1, pp. 3–15, 1982.

[53] D. Leach and D. Moore, "Toughness of aromatic polymer composites reinforced with carbon fibres," *Composites Science and Technology*, vol. 23, no. 2, pp. 131–161, 1985.

[54] P. Hine, B. Brew, R. Duckett, and I. Ward, "Failure mechanisms in continuous carbon-fibre reinforced peek composites," *Composites Science and technology*, vol. 35, no. 1, pp. 31–51, 1989.

[55] M. Iwamoto, S. Araki, K. Kurashiki, and K. Saito, "Comparison between mode i interlamina and intralamina fracture toughness of thin unidirectional graphite (as 4)/epoxy (1908) laminates," *ICCM/9. Composites Behaviour.*, vol. 5, pp. 795–802, 1993.

[56] P. Hine, B. Brew, R. Duckett, and I. Ward, "The fracture behaviour of carbon fibre reinforced poly (ether etherketone)," *Composites Science and technology*, vol. 33, no. 1, pp. 35–71, 1988.

[57] A. Garg and O. Ishai, "Hygrothermal influence on delamination behavior of graphite/epoxy laminates," *Engineering fracture mechanics*, vol. 22, no. 3, pp. 413–427, 1985.

[58] M. R. Wisnom and D. Green, "Tensile failure due to interaction between fibre breaks," *Composites*, vol. 26, no. 7, pp. 499–508, 1995.

[59] N. Pagano, "On the micromechanical failure modes in a class of ideal brittle matrix composites. part 1. coated-fiber composites," *Composites Part B: Engineering*, vol. 29, no. 2, pp. 93–119, 1998.

[60] N. Pagano, "On the micromechanical failure modes in a class of ideal brittle matrix composites. part 2. uncoated-fiber composites," *Composites Part B: Engineering*, vol. 29, no. 2, pp. 121–130, 1998.

[61] J.-K. Kim and Y.-W. Mai, "High strength, high fracture toughness fibre composites with interface control—a review," *Composites Science and Technology*, vol. 41, no. 4, pp. 333–378, 1991.

[62] A. A. Griffith, "Vi. the phenomena of rupture and flow in solids," *Philosophical transactions of the royal society of london. Series A, containing papers of a mathematical or physical character*, vol. 221, no. 582-593, pp. 163–198, 1921.

[63] A. Griffith, "The theory of rupture," in *First Int. Cong. Appl. Mech*, pp. 55–63, 1924.

[64] G. R. Irwin, "Analysis of stresses and strains near the end of a crack traversing a plate," 1957.

[65] J. F. Knott, *Fundamentals of fracture mechanics*.
Gruppo Italiano Frattura, 1973.

[66] A. McEvily and T. Johnston, "The role of cross-slip in brittle fracture and fatigue," *International Journal of Fracture Mechanics*, vol. 3, no. 1, pp. 45–74, 1967.

[67] C. E. Inglis, "Stresses in a plate due to the presence of cracks and sharp corners," *Trans Inst Naval Archit*, vol. 55, pp. 219–241, 1913.

[68] S. K. Maiti, *Fracture mechanics: Fundamentals and applications*.
Cambridge University Press, 2015.

[69] K. Honjo, "Fracture toughness of pan-based carbon fibers estimated from strength–mirror size relation," *Carbon*, vol. 41, no. 5, pp. 979–984, 2003.

[70] B. W. Rosen, "Mechanics of composite strengthening.," 1965.

[71] T. L. Anderson, *Fracture mechanics: fundamentals and applications*.
CRC press, 2017.

[72] C. Soutis, N. Fleck, and P. Smith, "Failure prediction technique for compression loaded carbon fibre-epoxy laminate with open holes," *Journal of Composite Materials*, vol. 25, no. 11, pp. 1476–1498, 1991.

[73] E. G. Guynn, W. L. Bradley, and W. Elber, "Micromechanics of compression failures in open hole composite laminates," *ASTM STP*, vol. 1012, pp. 118–136, 1989.

[74] T. Vogler and S. Kyriakides, "Initiation and axial propagation of kink bands in fiber composites," *Acta Materialia*, vol. 45, no. 6, pp. 2443–2454, 1997.

[75] T. Nizolek, M. Begley, R. McCabe, J. Avallone, N. Mara, I. Beyerlein, and T. Pollock, "Strain fields induced by kink band propagation in cu-nb nanolaminate composites," *Acta Materialia*, vol. 133, pp. 303–315, 2017.

[76] G. Catalanotti, P. Camanho, J. Xavier, C. Dávila, and A. Marques, "Measurement of resistance curves in the longitudinal failure of composites using digital image correlation," *Composites Science and Technology*, vol. 70, p. 1986, Sept. 2010.

[77] A. Ortega, P. Maimí, E. González, and D. Trias, "Characterization of the translaminar fracture cohesive law," *Composites Part A: Applied Science and Manufacturing*, vol. 91, pp. 501–509, 2016.

[78] A. Ortega, P. Maimí, E. González, J. S. de Aja, F. M. de la Escalera, and P. Cruz, "Translaminar fracture toughness of interply hybrid laminates under tensile and compressive loads," *Composites Science and Technology*, vol. 143, pp. 1–12, 2017.

[79] M. Laffan, S. Pinho, P. Robinson, and L. Iannucci, "Measurement of the in situ ply fracture toughness associated with mode i fibre tensile failure in frp. part ii: Size and lay-up effects," *Composites Science and Technology*, vol. 70, no. 4, pp. 614–621, 2010.

[80] P. Maimí, A. Wagih, A. Ortega, J. Xavier, N. Blanco, and P. Ponces Camanho, "Oon the experimental determination of the j -curve of quasi-brittle composite materials," *International Journal of Fracture*, vol. 224, no. 2, pp. 199–215, 2020.

[81] P. Maimí, A. Ortega, E. González, and J. Costa, "Should the translaminar fracture toughness of laminated composites be represented by the r or the j curve? a comparison of their consistency and predictive capability," *Composites Part A: Applied Science and Manufacturing*, vol. 156, p. 106867, 2022.

[82] M. Laffan, S. Pinho, P. Robinson, and A. McMillan, "Translaminar fracture toughness: The critical notch tip radius of 0 plies in cfrp," *Composites Science and Technology*, vol. 72, no. 1, pp. 97–102, 2011.

[83] R. Teixeira, S. Pinho, and P. Robinson, "Translaminar fracture toughness of cfrp: From the toughness of individual plies to the toughness of the laminates," in *15th European Conference on Composite Materials (ECCM15)*, 2015.

[84] L. Gigliotti and S. Pinho, "Translaminar fracture toughness of ncf composites with multi-axial blankets," *Materials & Design*, vol. 94, pp. 410–416, 2016.

[85] R. Teixeira, S. Pinho, and P. Robinson, "Thickness-dependence of the translaminar fracture toughness: experimental study using thin-ply composites," *Composites Part A: Applied Science and Manufacturing*, vol. 90, pp. 33–44, 2016.

[86] R. R. Souza, S. L. Nascimento Junior, N. N. Silveira, M. A. Arbelo, and M. V. Donadon, "Translaminar fracture toughness and fatigue crack growth characterization of carbon-epoxy plain weave laminates," *Polymer Composites*, 2019.

[87] G. Bullegas, S. T. Pinho, and S. Pimenta, "Engineering the translaminar fracture behaviour of thin-ply composites," *Composites Science and Technology*, vol. 131, pp. 110–122, 2016.

[88] M. Laffan, S. Pinho, and P. Robinson, "Mixed-mode translaminar fracture of cfrp: Failure analysis and fractography," *Composite Structures*, vol. 95, pp. 135–141, 2013.

[89] S. Syed Abdullah, L. Iannucci, and E. Greenhalgh, "On the translaminar fracture toughness of vectran/epoxy composite material,"

[90] M. S. Aly-Hassan, H. Hatta, and S. Wakayama, "Effect of zigzag damage extension mechanism on fracture toughness of cross-ply laminated carbon/carbon composites," *Advanced Composite Materials*, vol. 12, no. 2-3, pp. 223–236, 2003.

[91] K. G. Dassios, V. Kostopoulos, and M. Steen, "Intrinsic parameters in the fracture of carbon/carbon composites," *Composites Science and Technology*, vol. 65, no. 6, pp. 883–897, 2005.

[92] R. Reber, J. De Haan, J. Mayer, M. Petitmermet, and E. Wintermatnel, "Intralaminar fracture of weft-knitted carbon fiber reinforced peek," in *European Structural Integrity Society*, vol. 27, pp. 123–133, Elsevier, 2000.

[93] K. M. Prewo, "The effect of ply lay-up sequence on the fracture toughness of boron aluminum," *Journal of Composite Materials*, vol. 12, no. 1, pp. 40–52, 1978.

[94] C. Sun and K. Prewo, "The fracture toughness of boron aluminum composites," *Journal of Composite Materials*, vol. 11, no. 2, pp. 164–175, 1977.

[95] J. Underwood and M. Kortschot, "Notch-tip damage and translaminar fracture toughness measurements from carbon/epoxy laminates," tech. rep., ARMY ARMAMENT

RESEARCH DEVELOPMENT AND ENGINEERING CENTER WATERVLIET NY ..., 1994.

[96] J. E. Masters, "Translaminar fracture toughness of a composite wing skin made of stitched warp-knit fabric," 1997.

[97] R. R. Kumar and S. Jose, "Evaluation of intralaminar fracture toughness of angle ply laminate," 2002.

[98] S. T. Pinho, P. Robinson, and L. Iannucci, "Fracture toughness of the tensile and compressive fibre failure modes in laminated composites," *Composites science and technology*, vol. 66, no. 13, pp. 2069–2079, 2006.

[99] H. Tada, P. C. Paris, and G. R. Irwin, "The stress analysis of cracks," *Handbook, Del Research Corporation*, vol. 34, p. 635, 1973.

[100] J. M. Slepetz and L. Carlson, "Fracture of composite compact tension specimens," in *Fracture Mechanics of Composites*, vol. 593, pp. 143–162, ASTM International, 1975.

[101] H. Tada, P. C. Paris, and G. R. Irwin, *The stress analysis of cracks handbook*. American Society of Mechanical Engineers, 2000.

[102] J. R. Rice, "A path independent integral and the approximate analysis of strain concentration by notches and cracks," 1968.

[103] J. H. Underwood, M. T. Kortschot, W. R. Lloyd, H. L. Eidinoff, D. A. Wilson, and N. Ashbaugh, "Translaminar fracture toughness test methods and results from interlaboratory tests of carbon/epoxy laminates," *ASTM special technical publication*, vol. 1256, pp. 486–508, 1995.

[104] I. Kongshavn and A. Poursartip, "Experimental investigation of a strain-softening approach to predicting failure in notched fibre-reinforced composite laminates," *Composites Science and Technology*, vol. 59, no. 1, pp. 29–40, 1999.

[105] "Standard test method for translaminar fracture toughness of laminated and pultruded polymer matrix composite materials."

[106] C. E. Harris and D. Morris, "Fracture behavior of thick, laminated graphite/epoxy composites.," tech. rep., VIRGINIA POLYTECHNIC INST AND STATE UNIV BLACKSBURG DEPT OF ENGINEERING ..., 1984.

[107] J. Underwood, I. Burch, and S. Bandyopadhyay, "Effects of notch geometry and moisture on fracture strength of carbon/epoxy and carbon/bismaleimide laminates," in *Composite Materials: Fatigue and Fracture (Third Volume)*, ASTM International, 1991.

[108] D. Morris and H. Hahn, "Fracture resistance characterization of graphite/epoxy composites," in *Composite Materials: Testing and Design (Fourth Conference)*, ASTM International, 1977.

[109] Y. Yeow, D. Morris, and H. Brinson, "A correlative study between analysis and experiment on the fracture behavior of graphite/epoxy composites," *Journal of testing and evaluation*, vol. 7, no. 2, pp. 117–125, 1979.

[110] R. S. Vaidya and C. Sun, "Fracture criterion for notched thin composite laminates," *AIAA journal*, vol. 35, no. 2, pp. 311–316, 1997.

[111] X. Li, S. R. Hallett, M. R. Wisnom, N. Zobeiry, R. Vaziri, and A. Poursartip, "Experimental study of damage propagation in over-height compact tension tests," *Composites Part A: Applied Science and Manufacturing*, vol. 40, no. 12, pp. 1891–1899, 2009.

[112] X. Xu, A. Paul, and M. R. Wisnom, "Thickness effect on mode i trans-laminar fracture toughness of quasi-isotropic carbon/epoxy laminates," *Composite Structures*, vol. 210, pp. 145–151, 2019.

[113] A. Torabi and E. Pirhadi, "Notch failure in laminated composites under opening mode: The virtual isotropic material concept," *Composites Part B: Engineering*, vol. 172, pp. 61–75, 2019.

[114] P. Kuhn, G. Catalanotti, J. Xavier, P. Camanho, and H. Koerber, "Fracture toughness and crack resistance curves for fiber compressive failure mode in polymer composites under high rate loading," *Composite Structures*, vol. 182, pp. 164–175, 2017.

[115] A. Bergan, C. Dávila, F. Leone, J. Awerbuch, and T.-M. Tan, "A mode i cohesive law characterization procedure for through-the-thickness crack propagation in composite laminates," *Composites Part B: Engineering*, vol. 94, pp. 338–349, 2016.

[116] X. Xu, M. R. Wisnom, X. Li, and S. R. Hallett, "A numerical investigation into size effects in centre-notched quasi-isotropic carbon/epoxy laminates," *Composites Science and Technology*, vol. 111, pp. 32–39, 2015.

[117] K. V. Williams, R. Vaziri, and A. Poursartip, "A physically based continuum damage mechanics model for thin laminated composite structures," *International Journal of Solids and Structures*, vol. 40, no. 9, pp. 2267–2300, 2003.

[118] J. Maire and J. Chaboche, "A new formulation of continuum damage mechanics (cdm) for composite materials," *Aerospace Science and Technology*, vol. 1, no. 4, pp. 247–257, 1997.

[119] S. Murakami, *Continuum damage mechanics: a continuum mechanics approach to the analysis of damage and fracture*, vol. 185.
Springer Science & Business Media, 2012.

[120] M. Elices, G. Guinea, J. Gomez, and J. Planas, "The cohesive zone model: advantages, limitations and challenges," *Engineering fracture mechanics*, vol. 69, no. 2, pp. 137–163, 2002.

[121] A. Hillerborg, M. Modéer, and P.-E. Petersson, "Analysis of crack formation and crack growth in concrete by means of fracture mechanics and finite elements," *Cement and concrete research*, vol. 6, no. 6, pp. 773–781, 1976.

[122] M. Tijssens, E. Van der Giessen, and L. Sluys, "Modeling of crazing using a cohesive surface methodology," *Mechanics of Materials*, vol. 32, no. 1, pp. 19–35, 2000.

[123] G. Lin, X.-G. Meng, A. Cornec, and K.-H. Schwalbe, "The effect of strength mis-match on mechanical performance of weld joints," *International journal of fracture*, vol. 96, no. 1, pp. 37–54, 1999.

[124] S. Li, M. Thouless, A. Waas, J. Schroeder, and P. Zavattieri, "Use of a cohesive-zone model to analyze the fracture of a fiber-reinforced polymer–matrix composite," *Composites Science and Technology*, vol. 65, no. 3-4, pp. 537–549, 2005.

[125] I. S. Raju, "Calculation of strain-energy release rates with higher order and singular finite elements," *Engineering Fracture Mechanics*, vol. 28, no. 3, pp. 251–274, 1987.

[126] Z. Xiong, Y. Meng, C. Zhao, and Y. Liu, "Translaminar mode-i fracture toughness experiment of pultruded gfrp laminates using extended compact tension specimen," *Journal of Composite Materials*, vol. 56, no. 17, pp. 2713–2725, 2022.

[127] M. Heidari-Rarani and M. Sayedain, "Finite element modeling strategies for 2d and 3d delamination propagation in composite dcb specimens using vcct, czm and xfem approaches," *Theoretical and Applied Fracture Mechanics*, vol. 103, p. 102246, 2019.

[128] A. C. Orifici, R. S. Thomson, R. Degenhardt, C. Bisagni, and J. Bayandor, "Development of a finite-element analysis methodology for the propagation of delaminations in composite structures," *Mechanics of Composite Materials*, vol. 43, pp. 9–28, 2007.

[129] R. Vitali, R. T. Haftka, and B. V. Sankar, "Multi-fidelity design of stiffened composite panel with a crack," *Structural and Multidisciplinary Optimization*, vol. 23, no. 5, pp. 347–356, 2002.

[130] G. Catalanotti, P. Camanho, J. Xavier, C. Dávila, and A. Marques, "Measurement of resistance curves in the longitudinal failure of composites using digital image correlation," *Composites Science and Technology*, vol. 70, no. 13, pp. 1986–1993, 2010.

[131] P. Camanho and G. Catalanotti, "On the relation between the mode i fracture toughness of a composite laminate and that of a 0 ply: Analytical model and experimental validation," *Engineering Fracture Mechanics*, vol. 78, no. 13, pp. 2535–2546, 2011.

[132] A. S. for Testing and Materials, "Standard test methods for plane-strain fracture toughness and strain energy release rate of plastic materials," *American Society for Testing and Materials*.

[133] C. Furtado, A. Arteiro, P. Linde, B. Wardle, and P. Camanho, "Is there a ply thickness effect on the mode i intralaminar fracture toughness of composite laminates?," *Theoretical and Applied Fracture Mechanics*, vol. 107, p. 102473, 2020.

[134] X. Wu, J. Fuller, M. Fotouhi, and M. Wisnom, "Bearing failure of pseudo-ductile thin ply angle-ply laminates," 2018.

[135] I. Kongshavn and A. Poursartip, "Experimental investigation of a strain-softening approach to predicting failure in notched fibre-reinforced composite laminates," *Composites Science and Technology*, vol. 59, no. 1, pp. 29–40, 1999.